

Airborne radar-sounding investigations of the firn layer and subglacial environment of Devon
Ice Cap, Nunavut, Canada

by
Anja Rutishauser

A thesis submitted in partial fulfillment of the requirements for the degree of
Doctor of Philosophy

Department of Earth and Atmospheric Sciences
University of Alberta

© Anja Rutishauser, 2019

Abstract

Airborne radio-echo sounding (RES) is a powerful tool to derive properties of glaciers and ice caps over spatially extensive areas, and has fundamentally improved our understanding of the distribution and structure of near-surface snow and firn, the ice thickness distribution and englacial structure of ice masses, and the topography and thermal/hydrological properties of glacier beds. Although several airborne RES surveys have been conducted over Devon Ice Cap (DIC) in the Canadian Arctic prior to this work, the data had not been utilized to investigate either the properties of the near-surface firn or the subglacial hydrological conditions. The Devon Ice Cap is one of the largest ice masses in the Canadian Arctic, and is thought to have a cold-based interior where ice is frozen to the underlying bedrock. Under recent warming conditions leading to intensified summer melt, the firn of DIC has been affected by significant melting and refreezing processes that can complicate the measurement of the ice cap's surface mass balance. Here, we use airborne RES measurements over DIC to (i) investigate whether the nature of the glacier surface reflection can be used to characterize the spatial heterogeneity of the near-surface firn, and (ii) investigate the hydrological conditions beneath the ice cap.

A comparison of airborne- and ground-based RES, along with analysis of shallow firn cores, led to the development of a novel technique where the spatial heterogeneity of firn is characterized via the scattering component of surface returns from airborne RES data. This method allows for the characterization of firn over spatially extensive areas and can help to identify regions where the structure and stratigraphy of the firn layer are affected significantly by melting and refreezing processes. Investigations of the RES reflection from the base of the ice column led to the identification and detailed characterization of a hypersaline subglacial lake and provide evidence for an extensive brine-network beneath DIC. Since basal ice temperatures are well below the pressure-melting point, this water system is considered to be brine-rich, to the point that the salinity significantly depresses its freezing point. Geological

evidence suggests that a salt-bearing evaporite unit outcrops beneath DIC, and is presumed to be the solute source for the brine.

The hypersaline subglacial lake beneath DIC and its surrounding hydrological and geological conditions are globally unique. The subglacial lake beneath DIC is not only the first to be discovered in the Canadian Arctic, but also the only spatially isolated hypersaline subglacial lake so far identified on Earth. This subglacial lake and the surrounding brine-network may host viable microbial habitats and could thus be world-class analogs for potential microbial habitats on other icy planetary bodies, such as Europa and Mars, where it has been suggested that sub-ice brine bodies may also exist. Thus, the unique subglacial water system beneath DIC, and the hypersaline subglacial lake in particular, are compelling targets for future in-situ sampling and biogeochemical investigations. The results from this study provide crucial information for the planning of future research over the subglacial lake and surrounding brine-network, including in-situ access and sampling of the water to explore its habitability for microbial life.

Acknowledgments

First of all, I would like to thank my advisors Dr. Martin Sharp and Dr. Donald D. Blankenship for their advice and guidance during my PhD, and for giving me the freedom to pursue research topics that reflect my interests. I am also very grateful for the numerous opportunities to participate in fieldwork, attend classes, both overseas and in Alaska, and to present my research at multiple conferences.

Many thanks to all members of the Arctic and Alpine Research Group at the University of Alberta and the Polar and Planetary Research Group at the University of Texas Institute for Geophysics for your support during my thesis. Thank you Colleen Mortimer, Ashley Dubnick, Luisa Fernandes, Alison Criscitiello, Duncan Young, Natalie Wolfenbarger, Jamin Greenbaum, Lucas Beem, Cyril Grima and Dustin Schroeder for the great discussions and brainstorming sessions that helped shaped this thesis. Thank you Scott Kempf and Gregory Ng for patiently answering my many questions and helping me to produce the data products I needed for this thesis.

I would also like to thank all my friends in Edmonton, and all over the world, for your support during my PhD, and especially for the lovely potluck and game nights. Many thanks to my family who always encouraged and supported me. And to Kirk, thank you for your endless love and support, for brainstorming ideas with me and for our nerdy radar discussions.

Finally, I would like to thank The W. Garfield Weston Foundation for championing northern research and providing funding for the research in this thesis. I would also like to thank the Department of Earth and Atmospheric Sciences at the University of Alberta, UAlberta North, the Institute for Geophysical Research at the University of Alberta, and the Canadian Geophysical Union for scholarships and grants throughout my degree. Lastly, I thank the people from Polar Continental Shell Program and Kenn Borek Air Ltd. and Tom Richter for their logistical support during fieldwork, and NRI and the peoples of Grise Fjord and Resolute Bay for permission to conduct airborne surveys over Devon Ice Cap.

Table of Contents

Chapter 1 Introduction	1
1.1 Background and motivation	1
1.2 Thesis objectives and structure	3
1.3 References	5
Chapter 2 Characterizing near-surface firn using the scattered signal component of the glacier surface return from airborne radio-echo sounding	11
2.1 Abstract	11
2.2 Introduction	11
2.3 Data and Methods	12
2.3.1 Radio-Echo Sounding Data	12
2.3.2 Determination of the Scattered Signal Component	13
2.3.3 Surface Roughness and Theoretical Scattering Component	14
2.4 Results	15
2.4.1 Firn Facies from Ground-Based RES	15
2.4.2 Scattering Distribution and Correlation to Firn Facies Zones	17
2.4.3 Effects of Surface Roughness	17
2.5 Conclusions	19
2.6 Acknowledgments and Data	20
2.7 References	23
Chapter 3 Discovery of a hypersaline subglacial lake complex beneath Devon Ice Cap, Canadian Arctic	27
3.1 Abstract	27
3.2 Introduction	27
3.3 Results	28
3.3.1 Radar evidence for two subglacial lakes	28
3.3.2 Subglacial hydraulic head over the lake area	29
3.3.3 Modeled basal ice temperatures indicating hypersaline water	29
3.3.4 Underlying geology and source of salinity	30
3.4 Discussion	31
3.5 Materials and Methods	32
3.5.1 Radar data and interpretation	32
3.5.2 Bed DEM	32
3.5.3 Hydraulic head	33
3.5.4 Ice temperature modeling	33

3.5.5	Geological model	33
3.5.6	Depth to magnetic basement	33
3.6	Acknowledgments and Data	34
3.7	References	38
Chapter 4 Evidence for an extensive subglacial brine network under the Devon Ice Cap, Canadian Arctic		
		43
4.1	Abstract	43
4.2	Introduction	43
4.3	Data and Methods	45
4.3.1	Radar sounding data	45
4.3.2	Basal reflectivity	46
4.3.3	Derivation of radar attenuation rates	49
4.3.4	Arrhenius modeled attenuation rates	50
4.3.5	Radar-inferred attenuation rates	52
4.3.6	Subglacial hydraulic head and water flow paths	53
4.3.7	Basal roughness	55
4.4	Results	57
4.4.1	Bed morphology	57
4.4.2	Basal reflectivity	58
4.4.3	Hydraulic head and subglacial water routes	59
4.5	Definition of new shorelines for subglacial lake in T2	61
4.6	Discussion	63
4.6.1	Likelihood of the existence of the hypothesized subglacial lakes	63
4.6.2	Basal hydrological conditions outside the subglacial lake	65
4.7	Conclusions	66
4.8	Acknowledgments	67
4.9	References	81
Chapter 5 Conclusions		
		89
Bibliography		
		92

List of Tables

Table 2-1: Description of the defined firn facies zones and results from statistical analysis of the scattering coefficient showing the mean and standard deviation of P_n . Additionally, the mean laser-derived RMS height σ_h and modeled scattering coefficient within the three firn zones are listed.	20
Table 4-1: Parameters and dielectric properties used in the conductivity model to estimate attenuation rates across DIC.....	68
Table 4-2: Median (mdn) basal reflectivity along with their standard deviation (std)and hydraulic heads from data within the original shorelines outlined by Rutishauser et al., (2018), and the newly defined shorelines for T2A-C from this study. ΔR is the median reflectivity anomaly over the subglacial lakes relative to the median of data.	69

List of Figures

Figure 2-1: a) Map of the airborne (black) and ground-based RES profiles (blue) over Devon Ice Cap, along with the location of the shallow firn cores (green). Black dashed lines indicate the firn facies zone boundaries. b)-d) Ground-based RES profiles revealing the firn stratigraphy. Dashed lines mark the location where the three profiles cross (~1880 m elevation), and the black markers indicate the locations of the picked firn zone boundaries. The scattered component of the airborne RES surface echo (P_n) is plotted in color code above each profile.

..... 21

Figure 2-2: a) Airborne RES flight tracks over Devon Ice Cap, color coded with the RSR-derived scattered signal component P_n . b) Laser altimetry transects color coded with the modeled P_n values, indicating the theoretical scattered signal component for the laser-derived surface roughness. To better illustrate large-scale variations, both the RSR-derived and modeled P_n values are smoothed by a moving average filter (2 km along-track window length). The color coded squares indicate small-scale surface roughness values. Black dashed lines indicate the firn facies zone boundaries..... 22

Figure 2-3: Normalized density plot of RSR-derived scattering components (P_n) against laser RMS surface roughness (σ_h) within the three firn zones. The black dotted lines represent the modeled theoretical scattering component for the given σ_h and permittivity values of 2.3 and 3.0. If the surface roughness was the major source of signal scattering, P_n values would lie along/between these lines..... 23

Figure 3-1: Radar evidence for a subglacial lake complex on Devon Ice Cap. (A) Landsat image overlain with the location of the subglacial lakes (blue) and ice divides (black). (B) Bedrock topography of the DIC summit area overlain with selected radar profiles. The subglacial lakes are located within the bedrock troughs T1 and T2. (C) Relative reflectivity along the radar transects atop of bedrock contours. (D) Radar transects A-F. The top panel shows the radargrams, the middle panel shows the ice surface and bedrock elevation (black) and the hydraulic head (blue). The bottom panel shows the relative basal reflectivity along the transect (black) and the recorded specular content along cross-profile F (blue). The estimated lake extents are highlighted by blue shading. 35

Figure 3-2: Basal temperature, hydraulic head and projected salt-bearing outcrops beneath Devon Ice Cap. (A) Bedrock elevation overlain with the hydraulic head (blue) and ice divides (black). The blue star indicates the location of the hydraulic head minimum in T2, whereas the arrow indicates the direction of water potentially outflowing T1. (B) Bedrock elevation

contours overlain with modeled basal temperatures. The black triangle is the location of the ice temperature profile where a basal temperature of $-18.5\text{ }^{\circ}\text{C}$ was measured [Paterson and Clarke, 1978]. (C) The area where the Bay Fiord Formation containing the bedded salt sequence is projected to outcrop beneath the ice is marked in yellow. Radar profiles are marked in blue/red. D) Cross-section along radar transect CC' revealing the projected geology consisting of the Bay Fiord Formation (yellow) and underlying sedimentary rocks (brown)..... 36

Figure 4-1: Location of Devon Ice Cap in the Canadian Arctic and Landsat image of Devon Ice Cap overlain with the survey grid and the locations of of the previously identified subglacial lakes within the bedrock troughs T1 and T2. 70

Figure 4-2: Comparison of the 1D steady-state advection-diffusion modeled ice temperatures (red) to measured ice temperatures near the summit of DIC (black) [Paterson and Clarke, 1978]. The grey shaded area indicates the uncertainties by propagating the uncertainties of the model input parameters. 70

Figure 4-3: a) Map of modeled depth-averaged ice temperatures using a steady-state 1D advection-diffusion model across DIC along with the location of the previously hypothesized subglacial lakes. Black contour lines represent the ice surface elevation (200 m interval) and the ice divides. b) Adjusted depth-averaged Arrhenius modeled attenuation rates which are used for the attenuation correction in this study. 71

Figure 4-4: Radar inferred (linear fit between ice thickness and bed power) and Arrhenius modeled attenuation rates. The uncertainty in the Arrhenius modeled attenuation rates is computed using the average ice temperature uncertainty of $3.14\text{ }^{\circ}\text{C}$, which also represents the temperature error bars in the radar-inferred attenuation rates. Radar-inferred attenuation rate uncertainties are derived as N_h . The dotted black line represents the Arrhenius modeled attenuation rates with a multiplier of 1.4, which is used in this study. 72

Figure 4-5: a) Bedrock topography (contour lines every 25 m) overlain with the location of the outlines of the hypothesized subglacial lakes from Rutishauser et al., (2018) in blue. Red lines depict the 20 m/yr ice flow contour line derived from Van Wychen et al., (2014). b) Ice thickness along survey lines, overlain with the bedrock contours (every 50 m). 72

Figure 4-6: a) Basal roughness on a radar footprint scale ($\Delta x=300\text{m}$) over DIC, and b) basal roughness on the wavelength scale ($\Delta x=5\text{m}$) in the region of the subglacial lakes. c) Hurst exponent over DIC and d) Hurst exponent over the area of the subglacial lakes. Previously hypothesized (black) [Rutishauser et al., 2018] and newly defined (blue shaded) subglacial lake

boundaries are outlined. Bed contours are marked with thin black lines with a 50 m interval, whereas thick black lines indicate the location of the ice divides..... 73

Figure 4-7: Basal Reflectivity map along with the median reflectivity anomaly for the individual catchment areas (numbers). Brown lines indicate the bottom (thick lines) and top (thin lines) of the projected salt-bearing rock outcrops underneath the ice [Rutishauser et al., 2018]. Thin black lines are the bed topography contour lines (every 50 m), and thick black lines represent the locations of the ice divides. 73

Figure 4-8: a) Map indicating low roughness areas (yellow) and high reflectivity anomalies (blue), along with locations where they overlap (green). b) Correlation between basal reflectivity (R) and RMSD. c) Distribution of all RMSD values along with the distribution of RMSD over high reflectivity areas, which has a mean of 0.51 m (used as threshold to define ‘low roughness’ areas). d) Distribution of all basal reflectivities along with the reflectivities over low roughness areas, which has a mean of 4 dB..... 74

Figure 4-9 a) Bed DEM overlain with hydraulically flat areas (blue) and reflectivity anomalies $R \geq 12$ dB (red). b) Hydraulic head over the area of the hypothesized subglacial lakes overlain with hydraulically flat areas, reflectivity anomalies and potential water routes..... 74

Figure 4-10: a) Bedrock contour lines (25 m interval) overlain with basal reflectivity values over hydraulically flat areas. The newly defined shorelines of the subglacial water bodies in T2 are outlined in blue. b) and c) distribution of all (gray) hydraulic heads and slopes observed over DIC, along with the hydraulic heads and slopes that occur in areas where $R \geq 12$ dB (red). 75

Figure 4-11: Background map (grayscale) shows the water flow paths resulting from a perturbation model with 100 model runs, and is overlain with the basal reflectivities. Black solid and dotted lines mark the newly defined shorelines for the subglacial water bodies in T2 and the previously outlined subglacial lake in T1, respectively..... 76

Figure 4-12: Basal reflectivities along the radar profiles and newly defined outlines of the subglacial water bodies occupying the bedrock trough T2. The squares represent grid cells of the hydraulic head mesh and are color coded with their median reflectivity value. Large squares indicate grid cells that are hydraulically flat, whereas the blue and black contours indicate whether the median grid cell reflectivity is above or below one standard deviation of all measured reflectivities (σ), respectively. Small squares represent grid cells without a flat hydraulic head but for which the median reflectivity $\geq 1\sigma$. Thin black lines represent the

bedrock topography (25 m interval) whereas thick black lines mark the location of the ice divides. 76

Figure 4-13: a) Bedrock topography overlain with selected radar profiles across trough T2. b-f) Selected radar sections (top panel) along with the bed and surface elevations (black) the hydraulic head Θ (blue, middle panel) and the basal reflectivity (bottom panel). Areas of the subglacial water bodies outlined from this study are shaded in blue. 77

Figure 4-14: a) Bedrock topography overlain with selected profiles across the canyon extending from T2. b) Bedrock elevations along radar profiles across the canyon, revealing the trough morphology. All profiles are oriented from south towards the north, where the dot in a) marks the start point. The blue shaded areas represent the water bodies defined in this study, and the black dotted line indicates the approximate trough center defined by the water flow routes. . 78

Figure 4-15: a) Bed reflectivity overlain with bed elevation contours (25 m interval) and outlines of the newly defined water bodies. Thin lines represent the MCoRDS data used for previous identification of the subglacial lake [CReSIS, 2016; Rutishauser et al., 2018]. Previously hypothesized lake outline is shown as dotted black line. b) Bed topography overlain with outlines of the newly defined water bodies and the water flow routes. Arrows follow the gradients of the hydraulic head and indicate potential water flow. 79

List of Supplementary Figures

- Figure S 3-1: Histogram of all recorded basal reflectivity values on DIC. Corrections for geometrical spreading losses and attenuation are applied. Dashed lines represent the values of one, two and three standard deviation σ . The observed reflectivity anomalies over T1 and T2 (10-15 dB) are 1.6-2.4 standard deviations above the mean of all bed reflectivities measured on DIC. 37
- Figure S 3-2 Interpolated ice thickness near the DIC summit area. The ice thickness is overlain on bedrock elevation contours [m asl.]. Fine black lines indicate the location of the radar transects, whereas the thick black lines represent the ice divides. The locations of the subglacial lakes are indicated with dotted lines. 37
- Figure S 3-3: 3D geology model. Three-dimensional reconstruction of the bedrock topography (greyscale) and ice surface (blue) of DIC and the geological formations as interpolated from the published geology [Harrison et al., 2016] into our geology model. Outcrops of the Bay Fiord Formation (red) and Cambrian-Ordovician sediments (green) are observed to the west of DIC, underlain by the Archean Shield. Interpolation of these outcrops reveals that the geological formations are dipping upwards and towards DIC, with the Bay Fiord Formation intersecting the bedrock in the vicinity of T1 and T2. The location of the transect used to derive the magnetic depth to basement (DMB) is shown in black. 38
- Figure S 3-4: Comparison of modeled geology and depth to magnetic basement solutions (DMB). The top of the Archean shield (basement, brown solid line) is compared to the depth to magnetic basement (DMB) solutions (black crosses) derived from airborne magnetic data recorded along a transect east of the subglacial lakes (Figure S 3-3). The black lines represent the ice surface and bedrock topography. The error bars of the DMB solutions represent a 20 % uncertainty of the distance between the source and sensor. 38
- Figure S 4-1: Comparison of hydraulically flat areas computed for densities of subglacial brine (blue) and fresh water (green) over bedrock trough T2. Red dots mark areas where the basal reflectivity $R \geq 12$ dB. The hydraulic head for freshwater is flat over the southern valley slope of the subglacial bedrock trough T2, where basal reflectivities are not indicative for subglacial water. The hydraulic head for brine is also flat towards the top of the ridge south of T2. This is likely driven by the reversed bedrock and surface slopes, and not from subglacial water being in hydrostatic equilibrium. 80

Figure S 4-2: Flow accumulation model run 100 times with randomly perturbed hydraulic heads using 1x (a, d), 2x (b, e), and 3x (c, f) its uncertainty. Blue lines represent the water flow routes without perturbation. d-f show the flow routes within the region marked in a), along with the outlies of the subglacial water bodies defined from this study. 80

Chapter 1

Introduction

1.1 Background and motivation

Glaciers and ice caps in the Canadian Arctic Archipelago (CAA) contain the largest mass of ice outside Greenland and Antarctica [Radić and Hock, 2011], and are projected to be significant contributors to sea level rise over the next century [Radić and Hock, 2011; Radić et al., 2013; Vaughan et al., 2013; Harig and Simons, 2016]. Devon Ice Cap (DIC) is one of the largest ice caps in the CAA, covering an area of about 14,400 km² [Burgess and Sharp, 2004]. While the interior region of DIC is characterized by slow ice flow (< 20 m/a) and is considered to be cold based with ice frozen to the underlying bedrock [Paterson and Clarke, 1978; Burgess et al., 2005; Van Wychen et al., 2017], the ice cap is drained by a number of marine-terminating outlet glaciers, most of which are grounded below sea-level in their lower reaches [Van Wychen et al., 2017]. Although the mass balance of DIC is dominated by surface melt, dynamic mass loss through iceberg calving is significant, and is the second largest contributor to dynamic mass loss of all CAA ice masses [Van Wychen et al., 2014, 2015; Millan et al., 2017].

Under recent warming conditions, summer surface melt has intensified and extended into higher elevation regions of CAA ice caps than was historically the case [Fisher et al., 2011; Bezeau et al., 2013; Gascon et al., 2013]. In the accumulation area, meltwater percolates into the firn and, where firn temperatures are below freezing, refreezes to form ice layers. This process can lead to a significant increase in rates of firn densification, which can lead to lowering of the glacier's surface elevation even in the absence of mass loss [e.g. Braithwaite et al., 1994]. Furthermore, strong density contrasts associated with ice layers in the firn can generate ambiguous reflections in airborne or satellite radar altimetry measurements, leading to a difference between the measured elevation and that of the actual glacier surface [Gray et al., 2015]. Melting and refreezing processes in the firn can therefore lead to incorrect inferences about mass balance trends if these are derived from repeat surface elevation measurements by altimetry [Parry et al., 2007]. Over the past 10-15 years, such melting-and refreezing processes have been documented over DIC from repeat firn cores, borehole temperature profiles, and ground-based radar surveys [Bezeau et al., 2013; Gascon et al., 2013; Fernandes et al., 2018], but spatially extensive measurements are sparse.

Radio-echo sounding (RES), also known as ice-penetrating radar or radar sounding, is a powerful technique that has been applied to numerous glaciological problems since the 1960s

[e.g. *Gudmandsen, 1969; Robin et al., 1977; Plewes and Hubbard, 2001; Dowdeswell and Evans, 2004; Bingham and Siegert, 2007*]. RES is based on the transmission, propagation and reflection of electromagnetic waves in a subsurface medium, where reflections can occur at any contrast in the subsurface dielectric properties. When deployed from airborne platforms, RES provides an efficient method to study spatially extensive areas of glaciers and ice sheets, and has fundamentally improved our understanding of the properties and distribution of near-surface snow and firn, and of englacial and subglacial conditions. A particularly useful application of RES measurements is for the identification of subglacial water and the characterization of subglacial hydrological systems ([e.g. *Carter et al., 2009; Schroeder et al., 2013; Wolovick et al., 2013; Chu et al., 2018*]). The presence of water at a glacier bed can have significant effects on ice dynamics, where subglacial water reduces basal friction, which can facilitate faster ice flow and potentially lead to increased mass loss [e.g. *Zwally et al., 2002*]. RES surveys have also led to the identification of numerous subglacial lakes beneath the Antarctic and Greenland ice sheets [e.g. *Palmer et al., 2013; Wright and Siegert, 2013; Howat et al., 2015; Willis et al., 2015; Siegert et al., 2016*]. In-situ sampling of subglacial aquatic environments has shown that these systems provide viable microbial habitats, despite their extreme conditions and isolation from the atmosphere [e.g. *Karl et al., 1999; Skidmore et al., 2005; Mikucki and Priscu, 2007; Christner et al., 2014; Boetius et al., 2015*]. Thus, subglacial aquatic environments, and subglacial lakes in particular, have long been considered as possible terrestrial analogs for environments in which life might exist on other icy planetary bodies [e.g. *Cockell et al., 2013; Garcia-Lopez and Cid, 2017*].

The first RES measurements over DIC were conducted with a ground-based radar system in 1970, and were used to map the ice thickness and underlying bedrock topography [*Paterson and Koerner, 1974*]. A following survey over DIC in 1973 was one of the first RES surveys in which the shape of the returned waveform was recorded. This allowed a more quantitative analysis of the of basal reflections, including interpretations of the returned bed power, which led to the inference of a geological boundary between the central region of DIC and its western margin [*Oswald, 1975*]. Since then, several airborne RES campaigns have been conducted over DIC using more sophisticated radar systems [e.g. *Dowdeswell et al., 2004; CReSIS, 2016*]. However, while the resulting data have been used to derive the ice thickness, they have not yet been utilized to derive basal properties of DIC. Since these surveys also cover various snow/firn/ice facies zones on the glacier surface, each with distinctive properties, they also present the opportunity to investigate the characteristics of the near-surface firn over spatially extensive areas.

1.2 Thesis objectives and structure

As described above, several airborne RES surveys have been conducted over DIC but the data have not previously been utilized to investigate either the properties of the near-surface firn or the subglacial hydrological conditions. The majority of the datasets were collected at radar frequencies designed to derive the ice thickness or basal properties, but not to resolve the near-surface firn stratigraphy. Nevertheless, studies showed that firn properties can be extracted from low frequency measurements via statistical analyses of the surface return, although this approach had only been applied to areas without significant surface melt [*Grima et al.*, 2014b; *Schroeder et al.*, 2016b]. This thesis utilizes airborne RES measurements over DIC to address two research objectives: (i) to investigate whether the RES signal that is returned from the glacier surface can be used to characterize the spatial heterogeneity of the near-surface firn on DIC that is affected by melting and refreezing processes, and (ii) to investigate the subglacial hydrological conditions beneath this largely cold-based ice cap. Three studies addressing these objectives are presented.

Chapter 2 presents the development and application of a novel technique that uses the scattering signal component of airborne RES surface echoes to characterize near-surface firn that is affected by melting and refreezing processes. The scattering component of the surface reflection is derived from a statistical method (Radar Statistical Reconnaissance, RSR, [e.g. *Grima et al.*, 2012, 2014a, 2014b]), and results are compared to the firn stratigraphy observed from ground-based RES measurements and shallow firn cores. This comparison reveals three distinct firn facies across DIC, and shows that differences in the scattering component of the signal are mainly generated by differences in the near-surface firn stratigraphy. The results from this study suggest that this method has potential to characterize such firn stratigraphy, which can help to identify areas for which mass balance estimates based on surface elevation changes may have large uncertainties due to the occurrence of surface melting and refreezing processes in the firn (i.e. because melting would lower the surface while refreezing would trap the resulting water within the firn, and prevent it from leaving the ice cap as runoff). This study presents the first application of the RSR method to an ice cap where firn is affected by spatio-temporally complex patterns of melting and refreezing. The RSR technique has also been applied to planetary surfaces such as those of Mars [e.g. *Grima et al.*, 2012] and is proposed to be used by two forthcoming missions to the icy moons of Jupiter [*Grima et al.*, 2014a], for which this work will provide an improved understanding of the relationship between the RSR-derived signal components and near-surface properties. This chapter is co-authored and has been published in *Geophysical Research Letters*. I participated in the data collection, performed all data analysis

and wrote the manuscript. Co-authors provided roughness data that were collected prior to this study, assistance with airborne RES data processing, and edited the manuscript.

Citation: Rutishauser, A., C. Grima, M. Sharp, D. D. Blankenship, D. A. Young, F. Cawkwell, and J. A. Dowdeswell (2016), Characterizing near-surface firn using the scattered signal component of the glacier surface return from airborne radio-echo sounding, *Geophys. Res. Lett.*, 43(24), 12,502-12,510, doi:10.1002/2016GL071230.

An investigation of airborne RES-derived reflections from the ice-bed interface of DIC led to the somewhat unexpected identification of liquid subglacial water beneath the cold-based center of this ice cap. Chapter 3 presents geophysical and geological evidence for the existence of two hypersaline subglacial lakes beneath DIC. These lakes are located in areas where basal ice temperatures are estimated to be well below the freezing point of fresh water. An investigation of the regional geology suggests that a salt-bearing evaporite unit likely outcrops beneath the ice, potentially providing the solute source for the hypersaline water. This study presents evidence for not only the first subglacial lakes to be discovered in the Canadian Arctic, but also for the first spatially isolated hypersaline subglacial lakes to be identified to date. It is possible that these subglacial lakes may support microbial life and harbor unique ecosystems. Due to their cold, hypersaline conditions, these lakes represent unique analogs for brine systems that may exist on Europa [Schmidt *et al.*, 2011] and Mars [Orosei *et al.*, 2018], and are therefore particularly compelling targets for future in situ exploration, including microbiological and biogeochemical investigations. This chapter is co-authored and has been published in *Science Advances*. I participated in the collection of some of the data, performed the data analysis and wrote the manuscript. Co-authors provided assistance with data analysis and edited the manuscript.

Citation: Rutishauser, A., D. D. Blankenship, M. Sharp, M. L. Skidmore, J. S. Greenbaum, C. Grima, D. M. Schroeder, J. A. Dowdeswell, and D. A. Young (2018), Discovery of a hypersaline subglacial lake complex beneath Devon Ice Cap, Canadian Arctic, *Sci. Adv.*, 4(4), eaar4353, doi:10.1126/sciadv.aar4353.

Due to the limited coverage of the radar data used to identify the subglacial lakes beneath DIC, their full extent and surrounding hydrological conditions remained unknown. To increase the radar data coverage and overcome the limitations of the previous survey, a new targeted airborne geophysical survey was conducted over DIC in spring 2018. Chapter 4 uses this dataset to revisit the initial hypothesis for the existence of the subglacial lakes, to derive their full extents, and to investigate the characteristics of the surrounding subglacial environment.

Results strongly support the existence of one of the subglacial lakes, but indicate that it is larger than previously thought. In addition, the new dataset reveals evidence for an extensive brine-network in which water may be concentrated in small ponds, thin films, or in the pore volume of subglacial sediments. It is likely that the characteristics of this brine-network are related to the bedrock lithology and topography. Results from this study will help inform the planning of future research over the Devon subglacial lakes, and provide context necessary for the design of a future program for in-situ access and sampling of the lake water and brine network, any accreted ice formed above the lake, or sediment on the lake floor or directly beneath the ice to explore the suitability of these habitats for supporting life. This study is a collaborative work with the University of Texas Institute for Geophysics (UTIG), and will be prepared for publication in early 2019. I was involved in the planning and execution of the data collection, performed all data analyses and wrote the manuscript. Collaborators from UTIG assisted with data processing and, together with M. Sharp, edited the manuscript.

1.3 References

- Bezeau, P., M. Sharp, D. Burgess, and G. Gascon (2013), Firm profile changes in response to extreme 21st-century melting at Devon Ice Cap, Nunavut, Canada, *J. Glaciol.*, *59*(217), 981–991, doi:10.3189/2013JoG12J208.
- Bingham, R. G., and M. J. Siegert (2007), Radar-derived bed roughness characterization of Institute and Møller ice streams, West Antarctica, and comparison with Siple Coast ice streams, *Geophys. Res. Lett.*, *34*(21), 1–5, doi:10.1029/2007GL031483.
- Boetius, A., A. M. Anesio, J. W. Deming, J. A. Mikucki, and J. Z. Rapp (2015), Microbial ecology of the cryosphere: sea ice and glacial habitats, *Nat. Rev. Microbiol.*, *13*(11), 677–690, doi:10.1038/nrmicro3522.
- Braithwaite, R. J., M. Laternser, and W. T. Pfeffer (1994), Variations of near-surface firm density in the lower accumulation area of the Greenland ice sheet, Pakitsoq, West Greenland, *J. Glaciol.*, *40*(136), 477–485, doi:10.1088/0022-3727/48/32/325305.
- Burgess, D., and M. J. Sharp (2004), Recent Changes in Areal Extent of the Devon Ice Cap, Nunavut, Canada, *Arctic, Antarct. Alp. Res.*, *36*(2), 261–271, doi:10.1657/1523-0430(07-069).
- Burgess, D. O., M. J. Sharp, D. W. F. Mair, J. a. Dowdeswell, and T. J. Benham (2005), Flow dynamics and iceberg calving rates of Devon Ice Cap, Nunavut, Canada, *J. Glaciol.*, *51*(173), 219–230, doi:10.3189/172756505781829430.

- Carter, S. P., D. D. Blankenship, D. a. Young, and J. W. Holt (2009), Using radar-sounding data to identify the distribution and sources of subglacial water: Application to Dome C, East Antarctica, *J. Glaciol.*, 55(194), 1025–1040, doi:10.3189/002214309790794931.
- Christner, B. C. et al. (2014), A microbial ecosystem beneath the West Antarctic ice sheet, *Nature*, 512(7514), 310–313, doi:10.1038/nature13667.
- Chu, W., D. M. Schroeder, H. Seroussi, T. T. Creyts, and R. E. Bell (2018), Complex Basal Thermal Transition Near the Onset of Petermann Glacier, Greenland, *J. Geophys. Res. Earth Surf.*, 123(5)May, 985–995, doi:10.1029/2017JF004561.
- Cockell, C. S. et al. (2013), Subglacial Environments and the Search for Life Beyond the Earth, in *Antarctic Subglacial Aquatic Environments*, pp. 129–148, American Geophysical Union.
- CReSIS (2016), CReSIS, *Radar Depth Sounder Data*, Lawrence, Kansas, USA, Digital Media. <http://data.cresis.ku.edu/>
- Dowdeswell, J. A., and S. Evans (2004), Investigations of the form and flow of ice sheets and glaciers using radio-echo sounding, *Reports Prog. Phys.*, 67(10), 1821–1861, doi:10.1088/0034-4885/67/10/R03.
- Dowdeswell, J. A., T. J. Benham, M. R. Gorman, D. Burgess, and M. J. Sharp (2004), Form and flow of the Devon Island Ice Cap, Canadian Arctic, *J. Geophys. Res. Surf.*, 109(F2), doi:10.1029/2003JF000095.
- Fernandes, L., A. Schmitt, A. Wendleder, M. Sharp, and A. Roth (2018), Detecting Supraglacial Meltwater Drainage on the Devon Ice Cap using Kennaugh Decomposition of TerraSAR-X imagery, in *EUSAR 2018; 12th European Conference on Synthetic Aperture Radar*, pp. 1–6.
- Fisher, D., J. Zheng, D. Burgess, C. Zdanowicz, C. Kinnard, M. Sharp, and J. Bourgeois (2011), Recent melt rates of Canadian arctic ice caps are the highest in four millennia, *Glob. Planet. Change*, 84–85, 3–7, doi:10.1016/j.gloplacha.2011.06.005.
- Garcia-Lopez, E., and C. Cid (2017), Glaciers and ice sheets as analog environments of potentially habitable icy worlds, *Front. Microbiol.*, 8(JUL), 1407, doi:10.3389/fmicb.2017.01407.
- Gascon, G., M. Sharp, D. Burgess, P. Bezeau, and A. B. G. Bush (2013), Changes in

- accumulation-area firn stratigraphy and meltwater flow during a period of climate warming: Devon Ice Cap, Nunavut, Canada, *J. Geophys. Res. Earth Surf.*, *118*(4), 2380–2391, doi:10.1002/2013JF002838.
- Gray, L., D. Burgess, L. Copland, M. N. Demuth, T. Dunse, K. Langley, and T. V. Schuler (2015), CryoSat-2 delivers monthly and inter-annual surface elevation change for Arctic ice caps, *Cryosphere*, *9*(5), 1895–1913, doi:10.5194/tc-9-1895-2015.
- Grima, C., W. Kofman, A. Herique, R. Orosei, and R. Seu (2012), Quantitative analysis of Mars surface radar reflectivity at 20MHz, *Icarus*, *220*(1), 84–99, doi:10.1016/j.icarus.2012.04.017.
- Grima, C., D. M. Schroeder, D. D. Blankenship, and D. A. Young (2014a), Planetary landing-zone reconnaissance using ice-penetrating radar data: Concept validation in Antarctica, *Planet. Space Sci.*, *103*, doi:10.1016/j.pss.2014.07.018.
- Grima, C., D. D. Blankenship, D. A. Young, and D. M. Schroeder (2014b), Surface slope control on firn density at Thwaites Glacier, West Antarctica: Results from airborne radar sounding, *Geophys. Res. Lett.*, *41*(19), 6787–6794, doi:10.1002/2014GL061635.
- Gudmandsen, P. (1969), Airborne Radio Echo Sounding of the Greenland Ice Sheet, *Geogr. J.*, *135*(4), 548–551, doi:10.2307/1795099.
- Harig, C., and F. J. Simons (2016), Ice mass loss in Greenland, the Gulf of Alaska, and the Canadian Archipelago: Seasonal cycles and decadal trends, *Geophys. Res. Lett.*, *43*(7), 3150–3159, doi:10.1002/2016GL067759.
- Howat, I. M., C. Porter, M. J. Noh, B. E. Smith, and S. Jeong (2015), Brief communication: Sudden drainage of a subglacial lake beneath the Greenland Ice Sheet, *Cryosphere*, *9*(1), 103–108, doi:10.5194/tc-9-103-2015.
- Karl, D. M., D. F. Bird, K. Björkman, T. Houlihan, R. Shackelford, and L. Tupas (1999), Microorganisms in the accreted ice of Lake Vostok, Antarctica., *Science*, *286*(5447), 2144–2147, doi:10.1126/science.286.5447.2144.
- Mikucki, J. A., and J. C. Priscu (2007), Bacterial diversity associated with Blood Falls, a subglacial outflow from the Taylor Glacier, Antarctica, *Appl. Environ. Microbiol.*, *73*(12), 4029–4039, doi:10.1128/AEM.01396-06.
- Millan, R., J. Mouginot, and E. Rignot (2017), Mass budget of the glaciers and ice caps of the

- Queen Elizabeth Islands, Canada, from 1991 to 2015, *Environ. Res. Lett.*, 12(2), 024016, doi:10.1088/1748-9326/aa5b04.
- Orosei, R. et al. (2018), Radar evidence of subglacial liquid water on Mars., *Science*, 361(6401), 490–493, doi:10.1126/science.aar7268.
- Oswald, G. K. A. (1975), Investigation of Sub-Ice Bedrock Characteristics by Radio-Echo Sounding, *J. Glaciol.*, 15(73), 75–87, doi:10.3189/S0022143000034286.
- Palmer, S. J., J. A. Dowdeswell, P. Christoffersen, D. A. Young, D. D. Blankenship, J. S. Greenbaum, T. Benham, J. Bamber, and M. J. Siegert (2013), Greenland subglacial lakes detected by radar, *Geophys. Res. Lett.*, 40(23), 6154–6159, doi:10.1002/2013GL058383.
- Parry, V., P. Nienow, D. Mair, J. Scott, B. Hubbard, K. Steffen, and D. Wingham (2007), Investigations of meltwater refreezing and density variations in the snowpack and firn within the percolation zone of the Greenland ice sheet, *Ann. Glaciol.*, 46(1), 61–68, doi:10.3189/172756407782871332.
- Paterson, W. S. B., and G. K. C. Clarke (1978), Comparison of theoretical and observed temperature profiles in Devon Island ice cap, Canada, *Geophys. J. Int.*, 55(3), 615–632, doi:10.1111/j.1365-246X.1978.tb05931.x.
- Paterson, W. S. B., and R. M. Koerner (1974), Radio Echo Sounding on Four Ice Caps in Arctic Canada, *Arctic*, 27(3), 1–9.
- Plewes, L. A., and B. Hubbard (2001), A review of the use of radio-echo sounding in glaciology, *Prog. Phys. Geogr.*, 25(2), 203–236.
- Radić, V., and R. Hock (2011), Regionally differentiated contribution of mountain glaciers and ice caps to future sea-level rise, *Nat. Geosci.*, 4(2), 91–94, doi:10.1038/ngeo1052.
- Radić, V., A. Bliss, a. C. Beedlow, R. Hock, E. Miles, and J. G. Cogley (2013), Regional and global projections of twenty-first century glacier mass changes in response to climate scenarios from global climate models, *Clim. Dyn.*, 42(5841), 37–58, doi:10.1007/s00382-013-1719-7.
- Robin, G. D. Q., D. J. Drewry, and D. T. Meldrum (1977), International Studies of Ice Sheet and Bedrock, *Philos. Trans. R. Soc. B Biol. Sci.*, 279(963), 185–196, doi:10.1098/rstb.1977.0081.
- Schmidt, B. E., D. D. Blankenship, G. W. Patterson, and P. M. Schenk (2011), Active formation

- of ‘chaos terrain’ over shallow subsurface water on Europa, *Nature*, 479(7374), 502–505, doi:10.1038/nature10608.
- Schroeder, D. M., D. D. Blankenship, and D. A. Young (2013), Evidence for a water system transition beneath Thwaites Glacier, West Antarctica, *Proc. Natl. Acad. Sci.*, 110(30), 12225–12228, doi:10.1073/pnas.1302828110.
- Schroeder, D. M., C. Grima, and D. D. Blankenship (2016), Evidence for variable grounding-zone and shear-margin basal conditions across Thwaites Glacier, West Antarctica, *GEOPHYSICS*, 81(1), WA35-WA43, doi:10.1190/geo2015-0122.1.
- Siegert, M. J., N. Ross, J. Li, D. M. Schroeder, D. Rippin, D. Ashmore, R. Bingham, and P. Gogineni (2016), Subglacial controls on the flow of Institute Ice Stream, West Antarctica, *Ann. Glaciol.*, 57(73), 19–24, doi:10.1017/aog.2016.17.
- Skidmore, M., S. P. Anderson, M. Sharp, J. Foght, and B. D. Lanoil (2005), Comparison of microbial community compositions of two subglacial environments reveals a possible role for microbes in chemical weathering processes., *Appl. Environ. Microbiol.*, 71(11), 6986–97, doi:10.1128/AEM.71.11.6986-6997.2005.
- Vaughan, D. G., J. C. Comiso, I. Allison, J. Carrasco, G. Kaser, R. Kwok, and T. Murray (2013), IPCC Observations: Cryosphere, in *Climate Change 2013: The Physical Science Basis. Contribution of Working Group I to the Fifth Assessment Report of the Intergovernmental Panel on Climate Change*, pp. 317–382, Cambridge University Press, Cambridge, United Kingdom and New York, USA.
- Willis, M. J., B. G. Herried, M. G. Bevis, and R. E. Bell (2015), Recharge of a subglacial lake by surface meltwater in northeast Greenland, *Nature*, 518(7538), 223–227, doi:10.1038/nature14116.
- Wolovick, M. J., R. E. Bell, T. T. Creyts, and N. Frearson (2013), Identification and control of subglacial water networks under Dome A, Antarctica, *J. Geophys. Res. Earth Surf.*, 118(1), 140–154, doi:10.1029/2012JF002555.
- Wright, A., and M. J. Siegert (2013), The Identification and Physiographical Setting of Antarctic Subglacial Lakes: An Update Based on Recent Discoveries, in *Antarctic Subglacial Aquatic Environments*, pp. 9–26.
- Van Wychen, W., D. O. Burgess, L. Gray, L. Copland, M. Sharp, J. A. Dowdeswell, and T. J. Benham (2014), Glacier velocities and dynamic ice discharge from the Queen Elizabeth

Islands, Nunavut, Canada, *Geophys. Res. Lett.*, 41(2), 484–490, doi:10.1002/2013GL058558.

Van Wychen, W., L. Copland, D. O. Burgess, L. Gray, and N. Schaffer (2015), Glacier velocities and dynamic discharge from the ice masses of Baffin Island and Bylot Island, Nunavut, Canada, edited by T. Fisher, *Can. J. Earth Sci.*, 52(11), 980–989, doi:10.1139/cjes-2015-0087.

Van Wychen, W., J. Davis, L. Copland, D. O. Burgess, L. Gray, M. Sharp, J. A. Dowdeswell, and T. J. Benham (2017), Variability in ice motion and dynamic discharge from Devon Ice Cap, Nunavut, Canada, *J. Glaciol.*, 63(239), 436–449, doi:10.1017/jog.2017.2.

Zwally, H. J., W. Abdalati, T. Herring, K. Larson, J. Saba, and K. Steffen (2002), Surface Melt-Induced Acceleration of Greenland Ice-Sheet Flow, *Science (80-.)*, 297(5579), 218–222, doi:10.1126/science.1072708.

Chapter 2

Characterizing near-surface firn using the scattered signal component of the glacier surface return from airborne radio-echo sounding

2.1 Abstract

We derive the scattered component (hereafter referred to as the incoherent component) of glacier surface echoes from airborne radio-echo sounding measurements over Devon Ice Cap, Arctic Canada, and compare the scattering distribution to firn stratigraphy observations from ground-based radar data. Low scattering correlates to laterally homogeneous firn above 1800 m elevation containing thin, flat and continuous ice layers, and below 1200 m elevation where firn predominantly consists of ice. Increased scattering between elevations of 1200-1800 m corresponds to firn with inhomogeneous, undulating ice layers. No correlation was found to surface roughness and its theoretical incoherent backscattering values. This indicates that the scattering component is mainly influenced by the near-surface firn stratigraphy, whereas surface roughness effects are minor. Our results suggest that analyzing the scattered signal component of glacier surface echoes is a promising approach to characterize the spatial heterogeneity of firn that is affected by melting and refreezing processes.

2.2 Introduction

Glaciers and ice caps in the Canadian Arctic Archipelago (CAA) contain the largest mass of ice outside Greenland and Antarctica [Radić and Hock, 2011], and are projected to be significant contributors to sea level rise over the next century [Radić and Hock, 2011; Radić et al., 2013; Vaughan et al., 2013; Harig and Simons, 2016]. With recent summer warming, surface melt on these ice masses has intensified and extended to higher elevations [Fisher et al., 2011; Sharp et al., 2011; Bezeau et al., 2013; Gascon et al., 2013; Mortimer et al., 2016]. In the accumulation area, where firn temperatures are below freezing, meltwater percolates into the firn and refreezes as ice layers. Repeat firn cores, borehole temperature profiles, and ground-penetrating radar surveys document major changes in the firn stratigraphy of CAA ice caps and glaciers over the past 10-15 years [Bezeau et al., 2013; Gascon et al., 2013], but spatially extensive measurements are sparse.

Knowledge of the near-surface firn stratigraphy is important for interpreting altimetrically derived measurements of glacier surface height in terms of changes in glacier mass balance [Parry et al., 2007]. The glacier surface height in the accumulation area is affected by changes in the near-surface firn density, even in the absence of mass changes [Braithwaite et al., 1994].

Ice layer formation by meltwater percolation/refreezing can significantly increase firn densification rates, causing a lowering of the glacier surface height. Strong density contrasts associated with ice layers in the firn can generate ambiguous reflections in satellite radar altimetry data, leading to a difference between the measured elevation and that of the actual glacier surface [Gray *et al.*, 2015].

Recent studies used properties of the glacier surface reflection from airborne radio-echo sounding (RES) measurements to determine the near-surface firn density and the surface roughness of Thwaites Glacier, West Antarctica [Grima *et al.*, 2014a, 2014b; Schroeder *et al.*, 2016b]. However, direct density estimates from the RES surface signal are only feasible if the firn density increases continuously with depth (i.e. steady state accumulation) [Grima *et al.*, 2014b], which is not the case for CAA ice caps where there are often ice layers in the firn. Here, we investigate the use of the scattering signal component of the RES glacier surface reflection to characterize near-surface firn stratigraphies affected by melting and refreezing processes. We apply the Radar Statistical Reconnaissance (RSR) method [Grima *et al.*, 2014a] to airborne RES measurements from Devon Ice Cap (DIC) to calculate the scattering signal component. We compare this component to the near-surface firn stratigraphy revealed by ground-based RES measurements, and to glacier surface roughness estimates and their theoretical backscattering values. We then discuss the relative influences of the near-surface firn stratigraphy and the surface roughness on the scattering component, and show that the firn stratigraphy is the predominant influence on signal scattering. This is the first application of the RSR method to an ice cap with a firn layer affected by spatio-temporally complex patterns of melting and refreezing. We argue that the RSR method and analysis of the scattered signal component have potential to characterize such firn stratigraphy.

2.3 Data and Methods

2.3.1 Radio-Echo Sounding Data

Airborne RES data were collected over DIC in spring 2014 (Figure 2-1a) using the University of Texas Institute for Geophysics' High-Capability Radar Sounder (HiCARS) [Peters *et al.*, 2005]. HiCARS transmits chirped pulses at 60 MHz center frequency (i.e., 5 m wavelength) over a 15 MHz bandwidth [Peters *et al.*, 2005]. HiCARS was mounted on board a Basler DC-3 aircraft operated by Kenn Borek Air, and positioning was obtained with a Global Positioning System (GPS) providing a 15 cm root mean square (RMS) vertical accuracy and smaller horizontal errors. The resulting radar dataset was sampled every ~1 m along the survey

transects. The pulse-limited footprint (area illuminated by the radar) at the surface has a diameter of ~ 235 m for typical aircraft heights above ice (~ 700 m).

Several of the airborne RES transects were surveyed with a ground-based RES system in spring 2015 (Figure 2-1a). A PulseEKKO Noggin radar (Sensors & Software Inc.) with antennae operating at 500 MHz center frequency (i.e., 0.6 m wavelength) was mounted on a plastic sled towed by snowmobile, generating a dataset sampled every ~ 0.4 m along-track. Positioning was obtained with a Leica Geosystems GPS system providing a 25 cm RMS accuracy. Processing steps for these RES data included dewow filtering, time-zero shift, background removal, Butterworth band pass filtering, and the application of a gain function [e.g. *Cassidy*, 2009]. The firn stratigraphy was further documented using six ~ 11 m long firn cores drilled along the survey transects (Figure 2-1a) in May 2015. The stratigraphic data were used to validate and interpret the ground-based RES measurements, and to determine bulk firn permittivities and the radar wave velocity in firn.

2.3.2 Determination of the Scattered Signal Component

In airborne RES measurements, a strong signal from the glacier surface (surface echo) is generated by the large contrast in dielectric properties between the atmosphere and snow, firn or ice. The surface echo is affected by the material properties of the near-surface (e.g. the vertical dielectric profile and homogeneity) with the probed depth being a function of the pulse width (uppermost 5-10 m for the HiCARS signal). The surface echo strength (P) can be expressed as a combination of reflected (specular, deterministic phase interference, P_c) and scattered (random phase interference, P_n) signal components, so that $P = P_c + P_n$ [e.g. *Ulaby et al.*, 1986]. P_c is mainly sensitive to the permittivity of the probed subsurface, whereas P_n is dominantly affected by the surface roughness and by inhomogeneous geometries in the subsurface [*Grima et al.*, 2014a]. We apply the RSR method to estimate P_c and P_n [*Grima et al.*, 2014a, 2014b]. To calculate P_c and P_n , the amplitudes of consecutive surface echoes from a defined along-track baseline (1 km, equivalent to ~ 1000 echoes, repeated every 50 m) are combined in a statistical distribution. The resulting echo amplitude distributions are then best fitted with an analytically derived stochastic envelope (homodyned K-distribution, HK) which is parameterized with the signal components P_c and P_n [*Destempes and Cloutier*, 2010]. The scattering model assumes statistical stationarity of roughness effects over the sampled space (1 km baseline), however, the HK distribution allows for reflector/scatterer clustering (i.e. non-stationarity) over the radar footprint. [*Destempes and Cloutier*, 2010; *Grima et al.*, 2014a].

Although scattering values are only analyzed qualitatively, P_c and P_n values are calibrated by a comparison between the calculated radar reflectance P_c (roughness corrected) and the theoretical radar reflectance generated by an air-glacier ice interface (-11.08 dB) at locations where nadir looking camera pictures taken during the airborne RES survey showed exposures of bare ice. P_n values from areas where the correlation coefficient of the fit is below 95 %, and where the airplane roll angle was above 2° were considered unreliable and discarded.

2.3.3 Surface Roughness and Theoretical Scattering Component

Analytical models that describe backscattering from rough surfaces [Elfouhaily and Guérin, 2004] show that the scattering component of the surface echo is a function of the surface roughness. To investigate roughness effects on the surface echoes, we calculated the RMS roughness from laser altimetry data collected simultaneously with the HiCARS measurements, and modeled the theoretical scattered signal component for the resulting roughness. The laser altimeter provides a 2 mm range resolution with a footprint of ~ 1 m [Young *et al.*, 2008], and measurements were made every ~ 24.5 m along-track. The RMS height σ_h is defined as:

$$\sigma_h = \sqrt{\frac{1}{M} \sum_{i=1}^M (z(x_i) - \bar{z})^2} \quad (1)$$

where M is the number of surface height measurements, $z(x_i)$ is the height at location x_i , and \bar{z} is the mean of the surface heights. σ_h was calculated over sliding windows with $M = 7$ (baseline of ~ 171.5 m along-track), and the resulting RMS heights are used to model the theoretical scattered signal component of the surface echo, following Grima *et al.* [2012]:

$$P_n = 4k^2 r^2 \sigma_h^2 \left(1 - e^{-\left(\frac{Dkl}{2h}\right)^2} \right) \quad (2)$$

where k is the wavenumber, $r = (1 - \sqrt{\epsilon}) / (1 + \sqrt{\epsilon})$ is the surface Fresnel coefficient with ϵ being the dielectric constant of the firm, D is the footprint diameter at the glacier surface, l is the roughness correlation length, and h is the aircraft range to the surface. As the roughness correlation length is unknown, we assume $l > 10$ m [Grima *et al.*, 2014a], for which the exponential of (2) becomes $\ll 1$ and P_n values take on their maximum value. This is supported by RSR-derived surface densities at Thwaites Glacier where the same large correlation length assumption was applied, and the results conform well with expected density values [Grima *et al.*, 2014b]. We note that the laser and radar baselines for σ_h used in Eq. (2) are not the same.

The laser baseline used to calculate σ_h is ~ 171.5 m, whereas the horizontal length over which the radar scattering signal is affected by a given surface roughness is not known precisely; however, it has been estimated to be a few wavelengths (5-50 m) [Grima *et al.*, 2012]. Grima *et al.* [2014a] showed that radar RMS heights derived from P_n are about 33 % smaller than the corresponding laser-derived RMS heights for that specific acquisition platform. Hence, using laser-derived σ_h and assuming $l > 10$ m in Eq. (2) likely results in an overestimation of the modeled P_n values. The corresponding equation for the coherent signal part P_c can be found in Grima *et al.* [2014a] (Eq. 6).

Although the theoretical scattering signal component is mainly sensitive to the surface roughness, P_n is also a function of the firn permittivity. We use the stratigraphy of six firn cores (Figure 2-1a) to estimate bulk permittivity values for the uppermost 10 m of firn. Sections of the firn cores showing ice layers are assigned a density of 875 kg/m^3 [Bezeau *et al.*, 2013], whereas sections showing firn are assigned the theoretical depth-dependent density value $\rho(z) = \rho_i - (\rho_i - \rho_s)\exp(-\frac{z}{z_\rho})$ [Cuffey and Paterson, 2010], where $\rho_i = 875 \text{ kg/m}^3$ and $\rho_s = 320 \text{ kg/m}^3$ are the densities of glacier ice and the spring snowpack, respectively [Bezeau *et al.*, 2013]. The resulting average densities (ρ) for each core are converted to bulk permittivity values following the empirical relationship $\epsilon = (1 + 845 \times 10^{-6}\rho [\text{kg m}^{-3}])^2$ [Kovacs *et al.*, 1995]. From this, average firn permittivity values of 2.3 and 2.7 were used to model P_n in firn Zones I and II, respectively (see section 2.4.1 for specifications of firn zones). P_n values in firn Zone III were modeled with $\epsilon = 3.0$ (mostly ice in firn).

In addition to the surface roughness derived from laser altimeter data, we analyzed ground-based roughness measurements from a field campaign on DIC in spring 2004. The surface roughness was measured at 13 locations along a 48 km long transect from near the summit of the ice cap towards the margin in a southerly direction (Figure 2-2b). At each site, the height of a fixed laser level above the surface was measured at 10 cm intervals along 10 m long profiles oriented parallel (North-South direction) and perpendicular (West-East direction) to the transect. σ_h was calculated using Eq. (1) for each profile, and the overall mean surface roughness was determined for each site.

2.4 Results

2.4.1 Firn Facies from Ground-Based RES

Three ground-based radar echograms (Figure 2-1 (b-d)) reveal the stratigraphy of the uppermost ~ 12 m of the firn. The profiles intersect near the ice cap's summit at ~ 1880 m elevation and run

towards the margins in various directions (Figure 2-1a). A common elevation-dependent trend is observed in the firn stratigraphy: at the highest elevations (>1750 m), near the center of the ice cap, a few relatively flat and continuous reflections are present within the uppermost ~2 m of firn. These reflections correlate to thin ice layers (<0.18 m thick) identified in firn cores, and are interpreted as ice layers formed by refreezing of percolated meltwater. As elevation decreases, the ice layers in the firn thicken and become undulatory. Below ~1200 m elevation the low subsurface radar reflectivity indicates firn consisting mainly of ice, whereas internal reflections within the massive ice layers likely result from interfaces with residual bodies of firn. The massive ice layers form by refreezing of meltwater. Such a stratigraphy where firn is buried beneath ice layers formed by refreezing, is a plausible outcome of equilibrium line migration to higher elevations [e.g. *Gascon et al.*, 2013]. *Gascon et al.* [2013] describe firn stratigraphies observed on DIC and assess their implications for melt water flow.

To relate the RSR-derived scattering values to firn characteristics (section 2.4.2), we identify three firn facies zones. These are based on variations in the apparent homogeneity of firn in the ground-based RES data. A laterally homogeneous firn layer extending over an RSR baseline (1 km) is expected to generate surface echoes with a weak scattering signal component. In contrast, firn containing internal inhomogeneities (i.e. undulating ice layers) is expected to cause a higher scattering signal component. On this basis, Zone I is defined as the area where firn contains thin, flat and mostly continuous ice layers. It is found at elevations above 1750 m surrounding the summit of the ice cap. Zone II is found between 1150-1895 m elevation, where the ice layers are undulating, and significantly thicker than in Zone I. In Zone III, the uppermost 6 m (the theoretical depth to which the surface echo is affected by a dielectric profile composed of ice) of firn consists predominantly of ice, and appears more homogeneous than firn in Zone II. To exclude possible influences from ice flow within outlet glaciers (e.g. crevassing), we constrain Zone III to areas where the glacier surface lies above 900 m elevation. The resulting Zone III spans an elevation range of 900-1435 m, and likely includes areas that lie within the ablation zone in some years [*Gascon et al.*, 2013].

The spatial extent of the firn facies zones is shown in Figure 2-1a. For airborne RES profiles for which no ground-based RES data were available, the zone boundaries were interpolated using data from neighboring ground-based RES profiles. Since changes in firn characteristics between zones are gradual, we estimate a 5 km along-track error in zone boundary picking.

2.4.2 Scattering Distribution and Correlation to Firn Facies Zones

The RSR-derived scattering component ranges from -40 to -5 dB across DIC (Figure 2-2a). Like the firn stratigraphy, P_n values display an elevation-dependent trend forming a circular distribution pattern around the ice cap's center: P_n values are low (<-24 dB) in the summit region, (>1800 m) and below ~1400 m. These two areas are separated by a band of higher P_n values (>-24 dB). Transitions between these high- and low scattering areas coincide with the defined firn zone transitions (Figure 2-1) to within 0.4-7 km. The majority lie within the estimated 5 km picking error.

To quantify variations in P_n within the different firn facies zones, we analyzed the P_n values statistically (Table 2-1). Firn Zones I, II and III yield mean P_n values of -26.9 dB, -23.2 dB, and -27 dB, respectively. A Kruskal-Wallis test (non-parametric ANOVA) indicates that P_n values from Zone II are significantly ($p < 0.001$) different from those in Zones I and III, with a 95 % confidence level. Thus, the scattering properties of the different firn stratigraphies are statistically significantly different with respect to lateral homogeneity. These results are consistent with the expected pattern of high scattering where near-surface firn is inhomogeneous and low scattering where it is more homogeneous. The high scattering values in firn Zone II could be explained by the presence of the inhomogeneous, undulating ice layers in the firn, whereas the flat and continuous ice layers in firn Zone I appear to reflect the radar signal coherently. Similarly, the firn stratigraphy in Zone III does not significantly scatter the surface echo, indicating that, despite the presence of some residual firn bodies, the probed subsurface appears homogeneous at the frequency and configurations of HiCARS. Higher P_n values near some outlet glacier termini likely result from scattering at crevasses and broken floating ice.

2.4.3 Effects of Surface Roughness

The good correlation between areas with distinct P_n values and the different firn facies zones suggests that changes in the scattering coefficient are caused by changes in the firn stratigraphy. However, because P_n is also a function of surface roughness, it is important to determine whether there is any relation between P_n and the observed surface roughness. If surface roughness was the major source of signal scattering, a positive correlation would be expected between P_n and roughness [Grima *et al.*, 2014a].

The laser-derived RMS surface roughness of DIC ranges between 0.008 and 5.9 m, with averages for Zones I, II and III of 0.05 m, 0.09 m and 0.12 m respectively (Table 2-1). The modeled scattered signal components for the observed roughnesses (Figure 2-2b) are generally

lower (-31.9 dB, -26.9 dB and -24.5 dB for firm Zones I, II, and III, respectively, Table 2-1) than the RSR-derived scattering values, and have a different spatial pattern. This suggests the surface roughness of DIC is not the major influence on the scattered signal component, and supports the argument that differences in P_n are due to differences in the near-surface firm stratigraphy. This is reinforced by Figure 2-3, which shows that the observed P_n values and the laser-derived surface roughnesses are not correlated.

However, given the relatively large point separation of the laser measurements (24.5 m), the laser-derived σ_h values might exclude small, wind-sculpted forms like sastrugi and capture only large-scale surface irregularities. Unfortunately, no smaller scale roughness measurements are available for the period when the data used in this study were collected. Nevertheless, we analyzed ground-based roughness measurements from spring 2004 to seek possible correlations between small-scale roughness features and P_n . The formation and orientation of sastrugi and the associated surface roughness are dependent on the prevailing wind pattern over the glacier surface [e.g. *Mather*, 1962]. Because similar patterns of katabatic winds and sastrugi formation have been observed over multiple years on DIC [*Koerner*, 1966; *Boon et al.*, 2010], we argue that despite the ten-year time span between data collection, a comparison with roughness data from 2004 is meaningful. The small-scale surface roughness (10 cm point separation, 10 m baseline) ranges between 0.04-0.13 m and displays a general trend of increasing roughness with decreasing elevation (Figure 2-2b). However, no significant changes occur at the elevations where considerable shifts in P_n are observed (~1400 m and ~1800 m). This suggests that patterns in P_n are also not correlated to small-scale surface roughness. Thus, changes in the scattering signal component at the HiCARS instrument frequency are mainly caused by changes in the near-surface firm stratigraphy, while surface roughness effects are probably minor.

We assume that the winter snow pack has minimal effect on P_n . *Koerner*, [1966] showed that the snow depth distribution over DIC does not vary systematically with elevation, so it is unlikely to co-vary with the observed distribution of P_n . Furthermore, the end-of-winter snow pack that existed during the measurement period was mostly homogeneous and dominated by a layered (deterministic) structure (a layer of wind-packed snow overlying depth hoar), which would contribute primarily to the reflectance component (P_c).

While theoretical backscattering models for a rough surface layer are well established [e.g. *Ulaby et al.*, 1986; *Grima et al.*, 2012], the formulation of models that capture effects of rough/undulating layers within the subsurface is more difficult [e.g. *Tabatabaeenejad and Moghaddam*, 2010; *Tabatabaeenejad et al.*, 2013; *Zamani et al.*, 2016]. Although a quantitative

understanding of the scattering contribution from undulating ice layers in the firm facies of Zone II might explain the high P_n values in this zone, modeling such an effect is beyond the scope of this paper.

2.5 Conclusions

We calculated the scattering signal component of airborne RES surface echoes from DIC using the RSR method, and compared the resulting pattern to the near-surface firm stratigraphy, which contains numerous ice layers formed by melting-and refreezing processes. Three distinct facies zones occupy different elevation ranges and the scattered signal component changes significantly between them. Low scattering correlates with laterally homogeneous firm above 1800 m that contains thin, flat and continuous ice layers, and below 1200 m where firm predominantly consists of ice. Between 1200 and 1800 m, increased scattering coincides with firm containing inhomogeneous, undulating ice layers. Although backscattering theory suggests a correlation between surface roughness and scattered signal components, no such correlation was found on DIC. Scattering values modeled for the observed surface roughness are significantly lower than the RSR-derived scattering values, and failed to reproduce their spatial distribution pattern. Therefore, we conclude that changes in the scattering signal component on DIC are mainly generated by changes in the near-surface firm stratigraphy, although some contribution from surface roughness effects cannot be ruled out. Knowledge of the firm stratigraphy, especially the spatial extent of percolation features is critical if repeat altimetry measurements of surface height derived from airborne or satellite sensors are used to estimate mass balance changes on Arctic ice caps. Our results suggest that the combined use of the RSR method and the scattering component from airborne-RES measurements has potential to characterize near-surface firm. This can help to identify areas where firm is affected significantly by melting and refreezing processes, areas for which mass balance estimates based on altimetrically-derived records of surface elevation change may have large uncertainties. This promising approach can easily be applied to other glaciers and ice caps which experience similar spatially and temporally inhomogeneous melting and refreezing processes. Finally, the RSR technique is being applied to planetary surfaces such as Mars [e.g. *Grima et al.*, 2012] or two forthcoming missions to the icy moons of Jupiter [*Grima et al.*, 2014a], however, near-surface scattering effects are usually not considered. Our study will benefit planetary exploration by providing an improved understanding of the RSR-derived signal components and its relationship to near-surface properties.

2.6 Acknowledgments and Data

This work was supported by grants from UK NERC (NE/K004999), NASA (13-ICEE13-00018), NSERC (Discovery Grant/Northern Research Supplement), Alberta Innovates Technology Futures, the CRYSYS Program (Environment Canada), and a University of Alberta Northern Research Award. We thank PCSP for logistical support, and NRI, NWB and the peoples of Grise Fjord and Resolute Bay for research permission on Devon Ice Cap. A. Criscitiello, F. Habbal, G. Ng, C. Mortimer, S. Palmer, T. Richter, and many others helped with data collection. We also thank the editor Julienne Stroeve and two anonymous reviewers for their helpful comments that improved the manuscript. This is UTIG contribution #3020. The data products derived for this study are available by contacting the corresponding author.

Tables

Table 2-1: Description of the defined firn facies zones and results from statistical analysis of the scattering coefficient showing the mean and standard deviation of P_n . Additionally, the mean laser-derived RMS height σ_h and modeled scattering coefficient within the three firn zones are listed.

Firn Facies Zones			Mean P_n [dB]	Std. P_n [dB]	Mean Laser σ_h [m]	Mean Modeled P_n [dB]
Zone I	Thin, continuous ice layers	>1750 m asl.	-26.9	2.5	0.05	-31.9
Zone II	Thickening, undulating ice layers	1150-1895 m asl.	-23.2	2.8	0.09	-26.9
Zone III	Mostly ice in uppermost 6 m	900-1435 m asl.	-27.0	3.4	0.12	-24.5

Figures

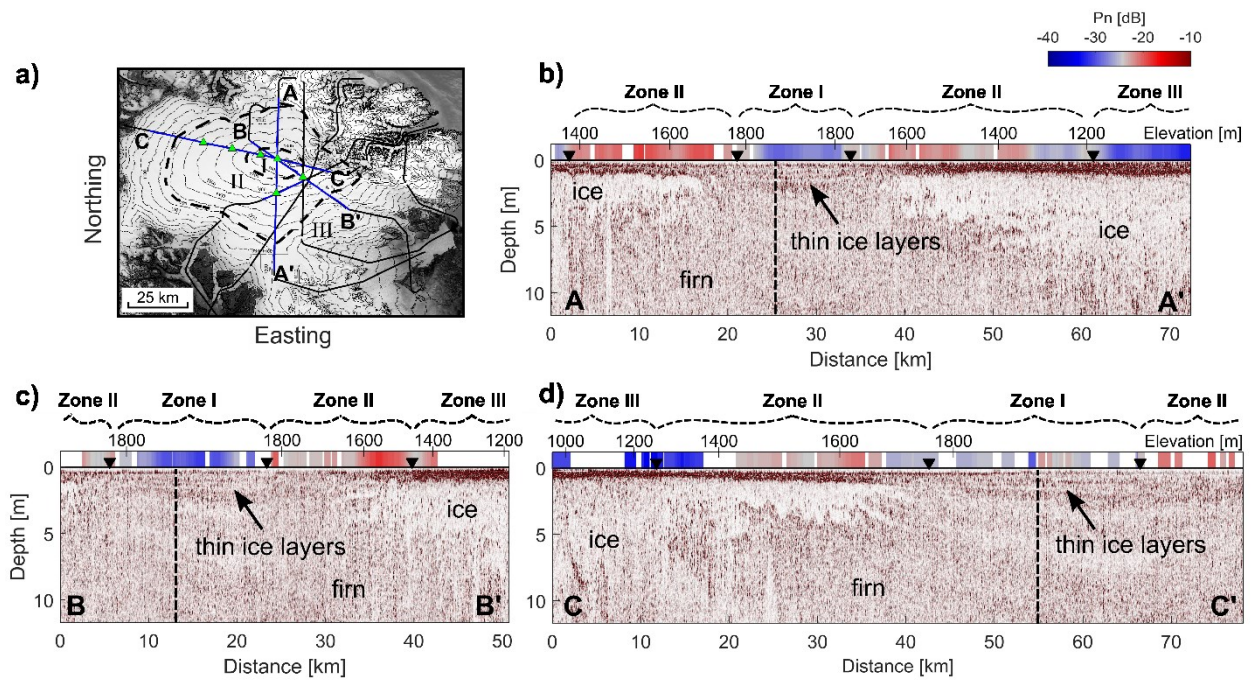


Figure 2-1: a) Map of the airborne (black) and ground-based RES profiles (blue) over Devon Ice Cap, along with the location of the shallow firn cores (green). Black dashed lines indicate the firn facies zone boundaries. b)-d) Ground-based RES profiles revealing the firn stratigraphy. Dashed lines mark the location where the three profiles cross (~1880 m elevation), and the black markers indicate the locations of the picked firn zone boundaries. The scattered component of the airborne RES surface echo (P_n) is plotted in color code above each profile.

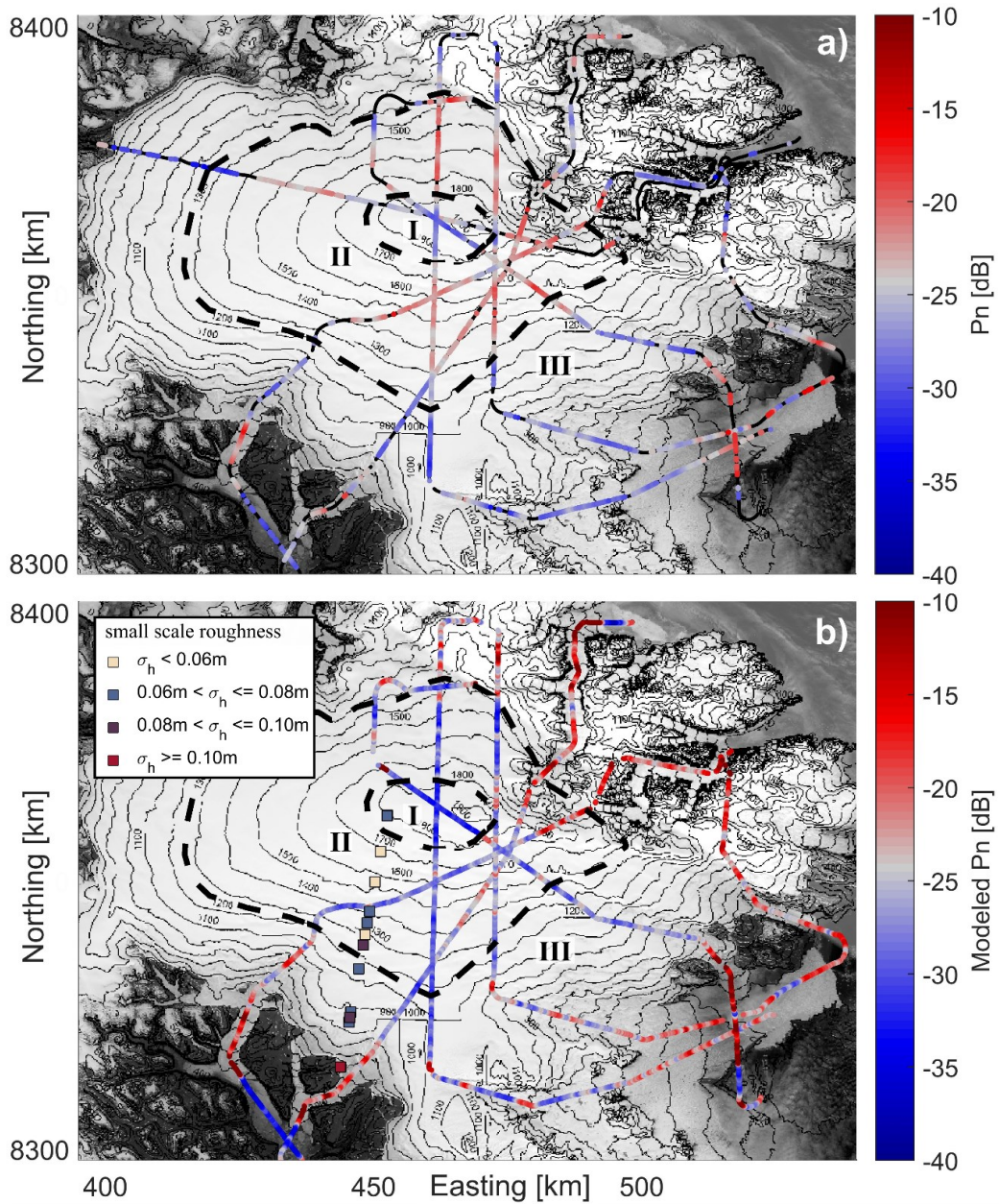


Figure 2-2: a) Airborne RES flight tracks over Devon Ice Cap, color coded with the RSR-derived scattered signal component P_n . b) Laser altimetry transects color coded with the modeled P_n values, indicating the theoretical scattered signal component for the laser-derived surface roughness. To better illustrate large-scale variations, both the RSR-derived and modeled P_n values are smoothed by a moving average filter (2 km along-track window length). The color coded squares indicate small-scale surface roughness values. Black dashed lines indicate the firn facies zone boundaries.

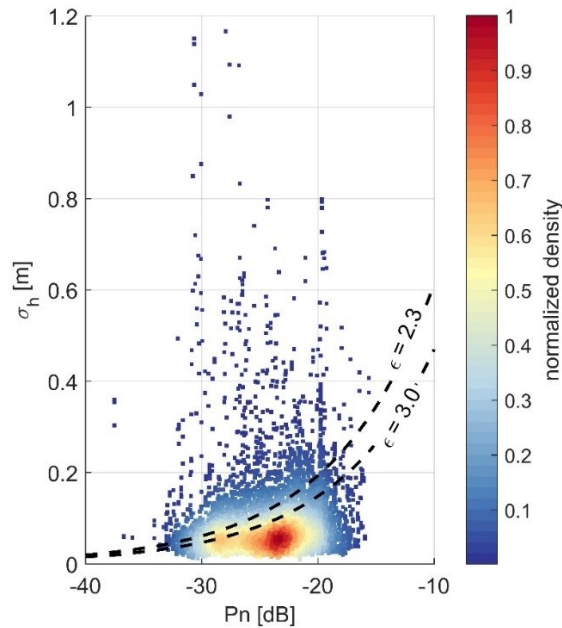


Figure 2-3: Normalized density plot of RSR-derived scattering components (P_n) against laser RMS surface roughness (σ_h) within the three firn zones. The black dotted lines represent the modeled theoretical scattering component for the given σ_h and permittivity values of 2.3 and 3.0. If the surface roughness was the major source of signal scattering, P_n values would lie along/between these lines.

2.7 References

- Bezeau, P., M. Sharp, D. Burgess, and G. Gascon (2013), Firm profile changes in response to extreme 21st-century melting at Devon Ice Cap, Nunavut, Canada, *J. Glaciol.*, 59(217), 981–991, doi:10.3189/2013JoG12J208.
- Boon, S., D. O. Burgess, R. M. Koerner, and M. J. Sharp (2010), Forty-seven Years of Research on the Devon Island Ice Cap, Arctic Canada., *Arctic*, 63(1), 13–29.
- Braithwaite, R. J., M. Laternser, and W. T. Pfeffer (1994), Variations of near-surface firm density in the lower accumulation area of the Greenland ice sheet, Pakitsoq, West Greenland, *J. Glaciol.*, 40(136), 477–485, doi:10.1088/0022-3727/48/32/325305.
- Cassidy, N. J. (2009), Ground Penetrating Radar Data Processing, Modelling and Analysis, in *Ground Penetrating Radar Theory and Applications*, edited by H. M. Jol, pp. 141–176, Elsevier, Amsterdam.
- Cuffey, K. M., and W. S. B. Paterson (2010), *The Physics of Glaciers*, Academic Press.
- Destrempe, F., and G. Cloutier (2010), A critical review and uniformized representation of statistical distributions modeling the ultrasound echo envelope, *Ultrasound Med. Biol.*, 36(7), 1037–1051, doi:10.1016/j.ultrasmedbio.2010.04.001.

- Elfouhaily, T. M., and C.-A. Guérin (2004), A critical survey of approximate scattering wave theories from random rough surfaces, *Waves in Random Media*, 14(4), R1–R40, doi:10.1088/0959-7174/14/4/R01.
- Fisher, D., J. Zheng, D. Burgess, C. Zdanowicz, C. Kinnard, M. Sharp, and J. Bourgeois (2011), Recent melt rates of Canadian arctic ice caps are the highest in four millennia, *Glob. Planet. Change*, 84–85, 3–7, doi:10.1016/j.gloplacha.2011.06.005.
- Gascon, G., M. Sharp, D. Burgess, P. Bezeau, and A. B. G. Bush (2013), Changes in accumulation-area firn stratigraphy and meltwater flow during a period of climate warming: Devon Ice Cap, Nunavut, Canada, *J. Geophys. Res. Earth Surf.*, 118(4), 2380–2391, doi:10.1002/2013JF002838.
- Gray, L., D. Burgess, L. Copland, M. N. Demuth, T. Dunse, K. Langley, and T. V. Schuler (2015), CryoSat-2 delivers monthly and inter-annual surface elevation change for Arctic ice caps, *Cryosphere*, 9(5), 1895–1913, doi:10.5194/tc-9-1895-2015.
- Grima, C., W. Kofman, A. Herique, R. Orosei, and R. Seu (2012), Quantitative analysis of Mars surface radar reflectivity at 20MHz, *Icarus*, 220(1), 84–99, doi:10.1016/j.icarus.2012.04.017.
- Grima, C., D. M. Schroeder, D. D. Blankenship, and D. A. Young (2014a), Planetary landing-zone reconnaissance using ice-penetrating radar data: Concept validation in Antarctica, *Planet. Space Sci.*, doi:10.1016/j.pss.2014.07.018.
- Grima, C., D. D. Blankenship, D. A. Young, and D. M. Schroeder (2014b), Surface slope control on firn density at Thwaites Glacier, West Antarctica: Results from airborne radar sounding, *Geophys. Res. Lett.*, 41(19), 6787–6794, doi:10.1002/2014GL061635.
- Harig, C., and F. J. Simons (2016), Ice mass loss in Greenland, the Gulf of Alaska, and the Canadian Archipelago: Seasonal cycles and decadal trends, *Geophys. Res. Lett.*, 43(7), 3150–3159, doi:10.1002/2016GL067759.
- Koerner, R. M. (1966), Accumulation on the Devon Island Ice Cap, Northwest Territories, Canada, *J. Glaciol.*, 6(45), 383–392.
- Kovacs, A., A. J. Gow, and R. M. Morey (1995), The in-situ dielectric constant of polar firn revisited, *Cold Reg. Sci. Technol.*, 23(3), 245–256, doi:10.1016/0165-232X(94)00016-Q.
- Mather, K. B. (1962), Further observations on sastrugi, snow dunes and the pattern of surface

- winds in Antarctica, *Polar Rec. (Gr. Brit.)*, 11(71), 158, doi:10.1017/S0032247400052888.
- Mortimer, C. A., M. Sharp, and B. Wouters (2016), Glacier surface temperatures in the Canadian High Arctic, 2000–15, *J. Glaciol.*, (July), 1–13, doi:10.1017/jog.2016.80.
- Parry, V., P. Nienow, D. Mair, J. Scott, B. Hubbard, K. Steffen, and D. Wingham (2007), Investigations of meltwater refreezing and density variations in the snowpack and firn within the percolation zone of the Greenland ice sheet, *Ann. Glaciol.*, 46(1), 61–68, doi:10.3189/172756407782871332.
- Peters, M. E., D. D. Blankenship, and D. L. Morse (2005), Analysis techniques for coherent airborne radar sounding: Application to West Antarctic ice streams, *J. Geophys. Res. Solid Earth*, 110(B6), doi:10.1029/2004JB003222.
- Radić, V., and R. Hock (2011), Regionally differentiated contribution of mountain glaciers and ice caps to future sea-level rise, *Nat. Geosci.*, 4(2), 91–94, doi:10.1038/ngeo1052.
- Radić, V., A. Bliss, a. C. Beedlow, R. Hock, E. Miles, and J. G. Cogley (2013), Regional and global projections of twenty-first century glacier mass changes in response to climate scenarios from global climate models, *Clim. Dyn.*, 42(5841), 37–58, doi:10.1007/s00382-013-1719-7.
- Schroeder, D. M., C. Grima, and D. D. Blankenship (2016), Evidence for variable grounding-zone and shear-margin basal conditions across Thwaites Glacier, West Antarctica, *Geophysics*, 81(1), WA35-WA43, doi:10.1190/geo2015-0122.1.
- Sharp, M., D. O. Burgess, J. G. Cogley, M. Ecclestone, C. Labine, and G. J. Wolken (2011), Extreme melt on Canada's Arctic ice caps in the 21st century, *Geophys. Res. Lett.*, 38(11), doi:10.1029/2011GL047381.
- Tabatabaeenejad, A., and M. Moghaddam (2010), Study of validity region of small perturbation method for two-layer rough surfaces, *IEEE Geosci. Remote Sens. Lett.*, 7(2), 319–323, doi:10.1109/LGRS.2009.2034543.
- Tabatabaeenejad, A., X. Duan, and M. Moghaddam (2013), Coherent scattering of electromagnetic waves from two-layer rough surfaces within the kirchhoff regime, *IEEE Trans. Geosci. Remote Sens.*, 51(7), 3943–3953, doi:10.1109/TGRS.2012.2229391.
- Ulaby, F. T., R. K. Moore, and A. K. Fung (1986), *Microwave remote sensing, active and*

passive; Volume III, From theory to applications Remote sensing, a series of advanced level textbooks and reference works, BOOK, Artech House : Dedham, MA, United States, Univ. Mich., Ann Arbor, MI, United States.

Vaughan, D. G., J. C. Comiso, I. Allison, J. Carrasco, G. Kaser, R. Kwok, and T. Murray (2013), IPCC Observations: Cryosphere, *Clim. Chang. 2013 Phys. Sci. Basis. Contrib. Work. Gr. I to Fifth Assess. Rep. Intergov. Panel Clim. Chang.*, doi:10.1017/CBO9781107415324.

Young, D. a., S. D. Kempf, D. D. Blankenship, J. W. Holt, and D. L. Morse (2008), New airborne laser altimetry over the Thwaites Glacier catchment, West Antarctica, *Geochemistry, Geophys. Geosystems*, 9(6), 1–11, doi:10.1029/2007GC001935.

Zamani, H., A. Tavakoli, and M. Dehmollaian (2016), Scattering from Layered Rough Surfaces: Analytical and Numerical Investigations, *IEEE Trans. Geosci. Remote Sens.*, 54(6), 3685–3692, doi:10.1109/TGRS.2016.2524639.

Chapter 3

Discovery of a hypersaline subglacial lake complex beneath Devon Ice Cap, Canadian Arctic

3.1 Abstract

Subglacial lakes are unique environments that, despite the extreme dark and cold conditions, have been shown to host microbial life. Many subglacial lakes have been discovered beneath the ice sheets of Antarctica and Greenland, but none have been reported to be hypersaline. Here, we use radio-echo sounding measurements to identify two subglacial lakes situated in bedrock troughs near the ice divide of Devon Ice Cap, Canadian Arctic. Modeled basal ice temperatures in the lake area are no higher than $-10.5\text{ }^{\circ}\text{C}$, indicating that these lakes consist of hypersaline water. This is in agreement with the surrounding geology suggesting that the subglacial lakes are situated within an evaporite-rich sediment unit containing a bedded salt sequence, which likely act as the solute-source for the brine. Our results reveal the first evidence for subglacial lakes in the Canadian Arctic, and the first hypersaline subglacial lakes reported to date. We conclude that these previously unknown hypersaline subglacial lakes may represent significant and largely isolated microbial habitats, and are compelling analogs for potential ice-covered brine lakes and lenses on planetary bodies across the Solar System.

3.2 Introduction

Subglacial lakes in Antarctica mainly exist where temperatures at the glacier bed are maintained at the pressure-melting point from a combination of geothermal or frictional heating and the thermal insulation provided by the thick ice cover [Carter *et al.*, 2007; Wright and Siegert, 2012; Young *et al.*, 2017]. In contrast, many of the Greenland subglacial lakes [Palmer *et al.*, 2013; Howat *et al.*, 2015; Willis *et al.*, 2015] receive surface meltwater input, providing heat that prevents the subglacial water bodies from freezing even at temperatures below the pressure-melting point [Howat *et al.*, 2015; Willis *et al.*, 2015]. Liquid subglacial water has also been found to exist at sub-freezing temperatures beneath Taylor Glacier in the McMurdo Dry Valleys, Antarctica, where the composition of the brine-rich water depresses its freezing point [Mikucki *et al.*, 2004; Badgeley *et al.*, 2017]. Research over the past two decades has revealed increasing evidence that subglacial aquatic environments can host microbial life [Karl *et al.*, 1999; Skidmore *et al.*, 2005; Mikucki and Priscu, 2007], and recent direct sampling of an Antarctic subglacial lake confirmed the presence of a viable microbial ecosystem in this dark and cold environment [Christner *et al.*, 2014]. Terrestrial subglacial water systems are therefore

considered as potential analogs for microbial habitats on other planetary bodies where the presence of liquid water beneath ice has been inferred [Clifford, 1987; Schmidt *et al.*, 2011; Cockell *et al.*, 2013].

Devon Ice Cap (DIC) is one of the largest ice caps in the Canadian Arctic (Figure 3-1A), and has been surveyed extensively by radio-echo sounding (RES), a well-established technique used to identify subglacial lakes from hydraulically flat, bright, and specular (mirror-like) reflections from the glacier bed [Carter *et al.*, 2007; Schroeder *et al.*, 2015]. The interior region of DIC consists of a rugged terrain with mountain ridges reaching 1700 m above sea level (asl.) and several 100-200 m deep bedrock troughs (Figure 3-1B). This region has previously been inferred to be cold based where the ice is frozen to the bed [Burgess *et al.*, 2005; Van Wychen *et al.*, 2017]. Here, we present a combined interpretation of RES and geological data, which reveals evidence for the existence of a previously unknown hypersaline subglacial lake complex near the ice divide of DIC.

3.3 Results

3.3.1 Radar evidence for two subglacial lakes

A total of eight radar transects show relative bed reflectivity that is 10-15 dB higher over two troughs, T1 and T2, than in the surrounding area (Figure 3-1). These reflectivity anomalies are 1.6-2.4 standard deviations above the mean of all bed reflectivities measured on DIC (Figure S 3-1). The larger dielectric contrast of an ice-water interface compared to an ice-dry rock interface results in significantly stronger bed echoes where the relative reflected power of freshwater and seawater with respect to unfrozen bedrock are expected to be ~10 dB and ~12 dB higher, respectively [Peters *et al.*, 2005]. We therefore interpret that the observed reflectivity anomalies over T1 and T2 result from the presence of subglacial water.

The character of the ice bottom interface is further evaluated by computing the radar specular content [Schroeder *et al.*, 2013, 2015; Young *et al.*, 2016] along profile F over T1 (Figure 3-1). The specular content is an expression of the relative proportions of specularly-reflected (mirror-like) and scattered radar energy and allows for the discrimination of smooth, flat ice-water interfaces (high specularity) and comparatively rough ice-rock interfaces (low specularity) [Schroeder *et al.*, 2015]. High specularity anomalies have typically been used to identify areas of subglacial water and lakes [Greenbaum *et al.*, 2015; Young *et al.*, 2016, 2017], and very high values have been used to infer areas of basal melting beneath an ice shelf [Greenbaum *et al.*, 2015]. We therefore propose that the observed specular anomaly over T1

indicates subglacial water. The exceptionally high specular content (> 0.75 , Figure 3-1D) in the center of T1 may result from basal melting, further smoothing the ice-water interface. Although no specular data are available over T2, the good agreement between the elevated specular content and reflectivity anomalies over T1 (Figure 3-1) supports the interpretation that the similar reflectivity anomalies over T2 result from the presence of subglacial water. Based on the extent of the radar signatures indicating subglacial water, and their confinement within two distinct topographic basins, we conclude that T1 and T2 each represent subglacial lakes. These subglacial lakes are located 2-5 km on either side of the west-east running ice divide, with mean ice thicknesses of 560 m over T1 and 740 m over T2 (Figure S 3-2). We estimate subglacial lake areas of about 5 km² and 8.3 km² for T1 and T2, respectively. These sizes are comparable to the majority of known [Carter *et al.*, 2007; Wright and Siegert, 2012] and predicted [Livingstone *et al.*, 2013] subglacial lakes in Antarctica and Greenland, however, the full extent of the water bodies beneath DIC may be underestimated due to limited radar coverage.

3.3.2 *Subglacial hydraulic head over the lake area*

Hydraulic heads calculated along the radar transects as well as from surface and bed DEMs are mostly flat across T2, with a local hydraulic minimum in the western part of the trough (Figure 3-1D and Figure 3-2A). A flat hydraulic head indicates hydrostatic equilibrium between the subglacial water and the overlying ice [Shreve, 1972], indicating that the ice is afloat above the basal water. The criteria of hydraulically flat reflections is commonly used to identify subglacial lakes [Carter *et al.*, 2007], further supporting the evidence for a subglacial lake in T2. Although the hydraulic head across T1 is relatively flat, no local hydraulic minimum is observed. Instead, the gradients of the hydraulic head suggest that water flows out of T1 in a north-west direction (Figure 3-2A). If water outflows T1, it is possible that the lake is replenished by active subglacial melting, which could explain the very high (> 0.75) specular content over T1. However, due to the relatively small horizontal lake extents and their confinement in bedrock troughs, bridging stresses in the overlying ice may prevent a fully developed hydraulic equilibrium. Other possible explanations for gradients in the hydraulic head include uncertainties due to undetected bedrock features where no RES data are available, or radar anomalies that arise from shallow water or water-saturated sediments.

3.3.3 *Modeled basal ice temperatures indicating hypersaline water*

Using a one-dimensional steady state advection-diffusion model [Cuffey and Paterson, 2010], we calculate basal temperatures of around -15.5 ± 3.5 °C in T1 and -14.3 ± 3.75 °C in T2 (Figure

3-2B). These modeled temperatures are in good agreement with a nearby measured ice temperature profile in which the basal temperature was $-18.5\text{ }^{\circ}\text{C}$ at 300 m depth [Paterson and Clarke, 1978], but are well below the pressure-melting point for fresh water derived from the overlying ice (about $-0.5\text{ }^{\circ}\text{C}$). Surficial water (and heat) input that would prevent the subglacial lakes from freezing is improbable since only limited surface meltwater is produced at elevations near the DIC summit [Wyatt and Sharp, 2015]. We therefore conclude that the subglacial lakes beneath DIC must consist of hypersaline water with a significantly depressed freezing-point temperature.

3.3.4 Underlying geology and source of salinity

Geological mapping shows outcrops of the Archean shield (igneous rocks) surrounding the eastern part of DIC, and Cambrian-Ordovician sediments, including an evaporite unit within the Bay Fiord formation, to the west of DIC [Harrison *et al.*, 2016] (Figure S 3-3). Drill cores from Bathurst Island, located west of Devon Island, show that the bottom of the Bay Fiord formation contains a bedded salt sequence with the salt consisting almost entirely of halite (98 %) [Mayr, 1980]. We use published outcrop data from Devon Island [Harrison *et al.*, 2016] to construct a three-dimensional geological model (Figure S 3-3) which allows us to constrain the bedrock geology beneath the ice. The modeled geology is consistent within the uncertainty for depth to magnetic basement solutions derived from airborne magnetics data (Figure S 3-4). Our geological model shows that the salt-bearing Bay Fiord formation outcrops near the DIC summit area, where it encloses the subglacial lake in T1, and outcrops about 100 m above the bottom of T2 (Figure 3-2). However, given the estimated uncertainty of 200 m in the projection of the geological model, it is possible that the subglacial lake in T2 is also situated within the Bay Fiord formation. The presence of the salt-bearing unit underlying the DIC summit area supports the existence of a substantial hypersaline subglacial lake complex, where the halite contained in the Bay Fiord formation likely provides the main source of salinity. The highest modeled ice temperatures within the uncertainty ranges for T1 and T2 are -12 and $-10.5\text{ }^{\circ}\text{C}$ respectively. Empirical studies show that in order to depress the freezing point of distilled water by $10.5\text{-}12\text{ }^{\circ}\text{C}$ with the addition of NaCl, a salinity of 140-160 practical salinity units (psu) (2.4-2.7 M NaCl) is required [Hall *et al.*, 1988]. These temperature and salinity values are similar to those of the brine-rich water body found beneath Taylor Glacier ($-7.8\text{ }^{\circ}\text{C}$, 125 psu) [Mikucki *et al.*, 2004] and the ice covered Lake Vida ($-13\text{ }^{\circ}\text{C}$, 200 psu) [Murray *et al.*, 2012], both located in the McMurdo Dry Valleys, Antarctica.

The observation of radar signatures indicative of subglacial water in an area where modeled basal ice temperatures are well below the pressure-melting point, and the likely outcrop of a bedded salt sequence beneath the ice in the same area provide compelling evidence for the existence of a hypersaline subglacial lake complex beneath DIC. These subglacial lakes are likely confined to bedrock troughs where the basal temperatures are higher due to a thicker, more insulating ice cover (Figure S 3-2). The geological model indicates that other troughs near the DIC summit are also underlain by the Bay Fiord formation (Figure 3-2C), however, more radar data are required to investigate their basal hydrological conditions. Additionally, outcrops of the Bay Fiord formation are common around Ellesmere Island [Harrison *et al.*, 2016] and may be found beneath other Canadian Arctic ice caps.

3.4 Discussion

Although numerous subglacial lakes have been discovered beneath the large ice sheets, the subglacial lake complex identified beneath DIC is unprecedented. These subglacial lakes, and their surrounding environments are very different from those reported in Antarctica and Greenland: The DIC lakes are situated within bedrock troughs in mountainous terrain, exist at temperatures well below the pressure-melting point, do not receive surface meltwater input, and likely consist of hypersaline water derived from dissolution of a surrounding salt-bearing geological formation. The origins of the hypersaline subglacial lakes, the processes by which they formed, and their potential interactions with shallow or deep groundwater flow remain unclear. However, possible mechanisms for the formation of the hypersaline subglacial water include melting of basal ice upon direct contact with the salt in the surrounding rocks, and modulated by double-diffusion processes within the waterbodies. The subglacial lakes might also be relict waterbodies that formed subaerially during an interglacial period, with the water becoming increasingly briny through interactions with underlying saline rocks, and as a result of cryo-concentration after they became permanently ice covered.

The only known subglacial fluid with temperature and salinity values comparable to this hypothesized hypersaline lake system beneath DIC, is the brine beneath Taylor Glacier, Antarctica [Mikucki *et al.*, 2004]. However, this brine body is not constrained as a spatially isolated subglacial lake, but is connected to a salt-rich ground-water system that is sourced by ancient marine water [Lyons *et al.*, 2005; Mikucki *et al.*, 2015; Badgeley *et al.*, 2017]. Brine outflows from Taylor Glacier have been shown to contain active microbial communities [Mikucki and Priscu, 2007], revealing that life is possible in such hypersaline, sub-ice aquatic environments. We therefore suggest that the DIC subglacial lakes may have the potential to

support microbial life and could harbor a unique ecosystem. If life exists in these lakes, it could have evolved in isolation since the area was last overridden by glacier ice, which was at least 120,000 years ago [Paterson *et al.*, 1977]. We conclude that the Devon Ice Cap's hypersaline subglacial lakes represent good analogs for the brine bodies inferred to exist beneath and potentially within Europa's ice shell [Schmidt *et al.*, 2011] or the Martian polar ice caps [Clifford, 1987], and are therefore compelling targets for future exploration.

3.5 Materials and Methods

3.5.1 Radar data and interpretation

Radio-echo sounding data were acquired with the University of Kansas Multichannel Coherent Radar Depth Sounder (MCoRDS) [CReSIS, 2016] during spring in the years 2011/12/14/15, and with the High Capability Airborne Radar Sounder (HiCARS) [Peters *et al.*, 2007] operated by the University of Texas Institute for Geophysics, during spring 2014. Ice thicknesses and basal reflectivity are extracted using a common semi-automatic method with rough localization from manual picking. Basal reflectivities were extracted from the HiCARS low gain data and from the MCoRDS CSARP_standard combined-gain data product. Basal reflectivity values were corrected for geometrical spreading losses, englacial attenuation and variations in radar systems [Schroeder *et al.*, 2016a]. Englacial attenuation rates were calculated and corrections applied along each individual radar profile via an adaptive fitting method [Schroeder *et al.*, 2016a]. We set the minimal requirement parameters to ensure a meaningful fitting to the same values as in [Schroeder *et al.*, 2016a]. If these requirements are not met along a profile, we apply the overall mean englacial attenuation rate derived from all radar data on DIC (26.8 dB/km, with a 7.3 dB/km standard deviation) to the profile. To correct for regional changes in attenuation rates and variations in radar system parameters, a long-wavelength signal (moving average with 30 km window length) from the bed echo along each radar profile was removed. The specular content from the HiCARS data was extracted by comparing the bed echo response from two different focusing aperture lengths [Schroeder *et al.*, 2015; Young *et al.*, 2016].

3.5.2 Bed DEM

An existing bedrock DEM [Dowdeswell *et al.*, 2004] was updated using the original bedrock depth dataset (derived from radar data collected over DIC in spring 2000 [Dowdeswell *et al.*, 2004]) in conjunction with bedrock depths from MCoRDS and HiCARS data collected between 2011-2015. The radar derived bedrock elevations were interpolated via a triangular linear

interpolation algorithm over a 1 km grid mesh. A crossover analysis yielded a mean error of ice thickness observation of 14 m (before interpolation).

3.5.3 Hydraulic head

Assuming the water pressure is equal to the ice overburden pressure, the basal hydraulic head (h) was calculated from the gridded bed elevations (B), and surface elevations (S) obtained from the ArcticDEM (Polar Geospatial Center from DigitalGlobe Inc. imagery), via

$$h = S \frac{\rho_i}{\rho_b} + B \left(1 - \frac{\rho_i}{\rho_b} \right),$$

where ρ_i is the ice density (917 kg/m³), and ρ_b is the brine density (1150 kg/m³, corresponding to 15 wt % NaCl) [Shreve, 1972].

3.5.4 Ice temperature modeling

To model basal ice temperatures, we use a one-dimensional steady state advection-diffusion model [Cuffey and Paterson, 2010] with the following parameters: A long-term accumulation rate of 0.19±0.05 m water equivalent per year [Paterson, 1976; Reeh and Paterson, 1988], an estimated geothermal heat flux of 65±5 mW/m² [Grasby et al., 2012] and an average annual surface temperature of -23±2°C at 1825 m elevation [Kinnard et al., 2006] with a 4.1°C/km lapse rate. The lapse rate is derived from surface air temperature records along a transect on DIC, sampling air temperatures at numerous elevations [Gardner et al., 2009].

3.5.5 Geological model

A geological map from the Canadian Arctic [Harrison et al., 2016] was combined with surface elevations derived from the ArcticDEM to generate a three-dimensional geological model (Figure S 3-3): First, surfaces through outcropping geological formation boundaries were interpolated, and formation thicknesses derived, assuming all geological units lie parallel to each other. Finally, the geological units were stacked atop of the interpolated formations that are most adjacent to DIC, using the derived formation thicknesses and the assumption that the units lie parallel to each other. Combining all formation thickness uncertainties, we estimate a total uncertainty of 200 m for the projected elevation of the Bay Fiord formation (salt-bearing unit) beneath DIC.

3.5.6 Depth to magnetic basement

We used depth to magnetic basement (DMB) solutions to infer the thickness of sediment beneath DIC. To do so, a 2D Werner deconvolution [Ku and Sharp, 1983] was applied to

available scalar airborne magnetics data with a single pass targeting shallow sources (0.5 to 5 km). Uncertainties in DMB estimates are commonly between 20 and 40% of the distance between the source and sensor [Ku and Sharp, 1983]. The results indicate sediment thicknesses consistent with our geological model within the range of uncertainties in the model and the DMB solutions (Figure S 3-4).

3.6 Acknowledgments and Data

General: We thank the NASA Operation IceBridge project team and the National Snow and Ice Data Center and acknowledge the use of MCoRDS airborne radar data from CReSIS generated with support from the University of Kansas, NSF grant ANT-0424589, and NASA Operation IceBridge grant NNX16AH54G. We thank the Polar Geospatial Center who provided the DEM under NSF OPP awards 1043681, 1559691 and 1542736. We thank F. Habbal, G. Ng, S. Palmer, and T. Richter for support during fieldwork, S. Grasby for providing us with an estimate for the geothermal heat flux, S. Kempf for assistance with radar data processing and T. Benham for providing bedrock elevations from the spring 2000 radar data set. We also thank N. Wolfenbarger, N. Ross, an anonymous reviewer and the editors M. Kelly and P. Bierman for providing feedback on the manuscript. This is UTIG contribution 3255.

Funding: This study was funded by grants from UK NERC (NE/K004999), NASA (13-ICEE13-00018), NSERC (Discovery Grant/Northern Research Supplement), Alberta Innovates Technology Futures, and the CRYSYS Program (Environment Canada). M.L.S. was partially supported by NSF 1543537 and NASA NNX16AJ64G, D.D.B and J.S.G. were partially supported by the G. Unger Vetlesen Foundation. D.D.B (assisted by A.R.) was supported as a Fulbright Scholar at the University of Gothenburg, Sweden.

Data and materials availability: MCoRDS radar data were accessed through the Center for Remote Sensing of Ice Sheets (CReSIS). UTIG radar data and the bedrock DEM will be made available upon request. ArcticDEM surface elevation data were accessed through the Polar Geospatial Center. All other data needed to evaluate the conclusions in the paper are present in the paper and/or the Supplementary Materials. Additional data related to this paper may be requested from the authors.

Figures

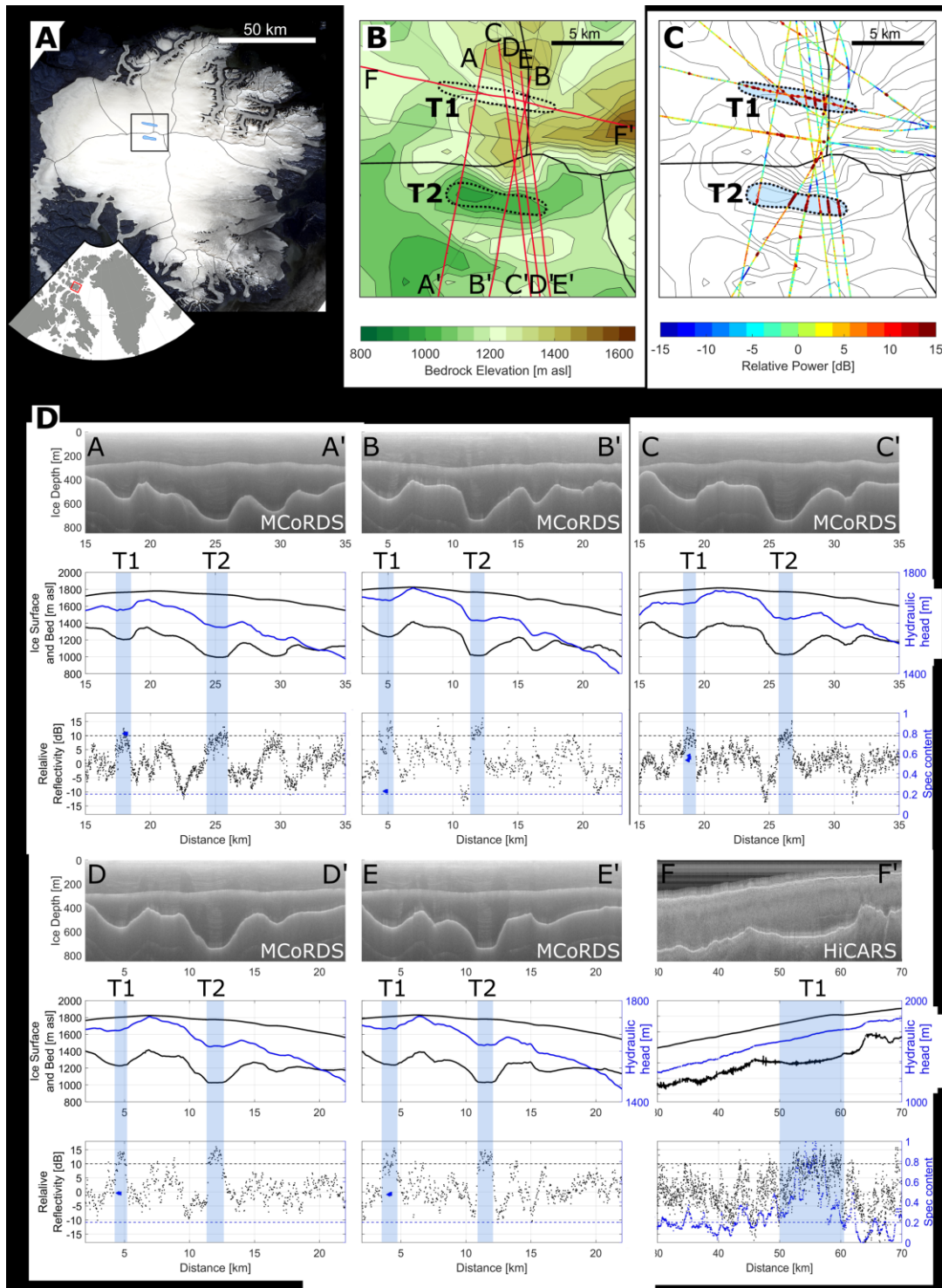


Figure 3-1: Radar evidence for a subglacial lake complex on Devon Ice Cap. (A) Landsat image overlain with the location of the subglacial lakes (blue) and ice divides (black). (B) Bedrock topography of the DIC summit area overlain with selected radar profiles. The subglacial lakes are located within the bedrock troughs T1 and T2. (C) Relative reflectivity along the radar transects atop of bedrock contours. (D) Radar transects A-F. The top panel shows the radargrams, the middle panel shows the ice surface and bedrock elevation (black) and the hydraulic head (blue). The bottom panel shows the relative basal reflectivity along the transect (black) and the recorded specularity content along cross-profile F (blue). The estimated lake extents are highlighted by blue shading.

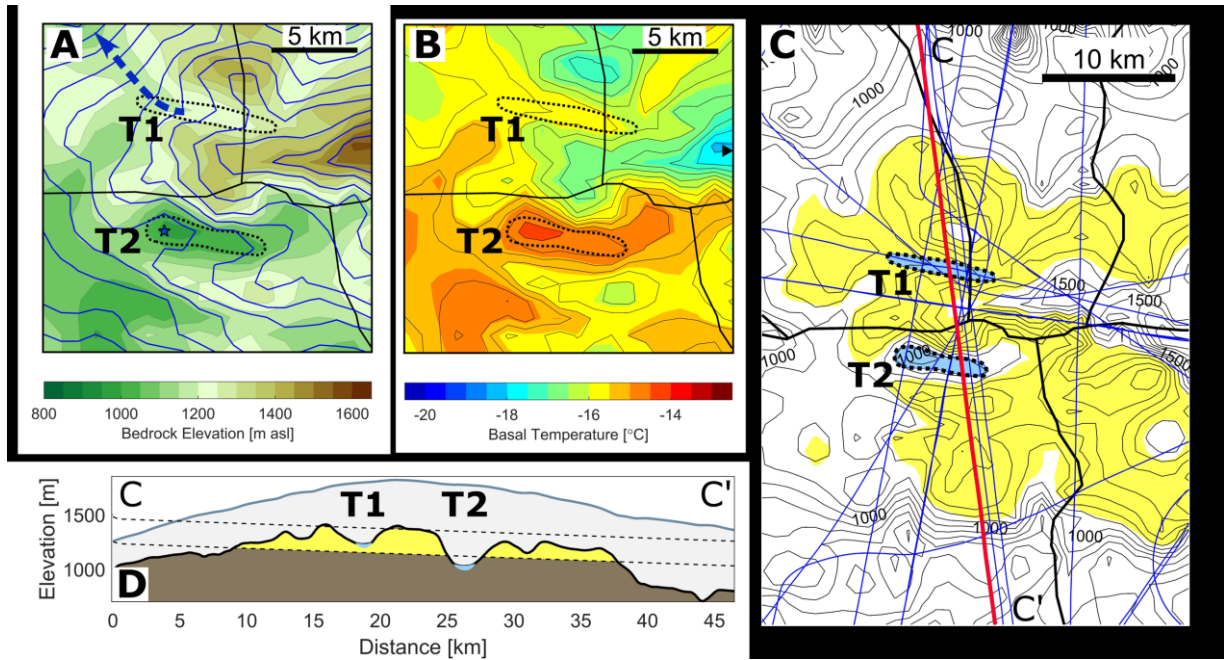


Figure 3-2: Basal temperature, hydraulic head and projected salt-bearing outcrops beneath Devon Ice Cap. (A) Bedrock elevation overlain with the hydraulic head (blue) and ice divides (black). The blue star indicates the location of the hydraulic head minimum in T2, whereas the arrow indicates the direction of water potentially outflowing T1. (B) Bedrock elevation contours overlain with modeled basal temperatures. The black triangle is the location of the ice temperature profile where a basal temperature of $-18.5\text{ }^{\circ}\text{C}$ was measured [Paterson and Clarke, 1978]. (C) The area where the Bay Fiord Formation containing the bedded salt sequence is projected to outcrop beneath the ice is marked in yellow. Radar profiles are marked in blue/red. (D) Cross-section along radar transect CC' revealing the projected geology consisting of the Bay Fiord Formation (yellow) and underlying sedimentary rocks (brown).

Supplementary Figures

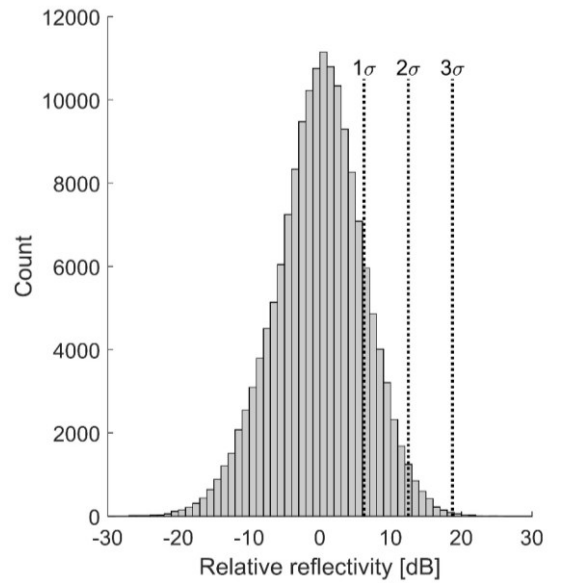


Figure S 3-1: Histogram of all recorded basal reflectivity values on DIC. Corrections for geometrical spreading losses and attenuation are applied. Dashed lines represent the values of one, two and three standard deviation σ . The observed reflectivity anomalies over T1 and T2 (10-15 dB) are 1.6-2.4 standard deviations above the mean of all bed reflectivities measured on DIC.

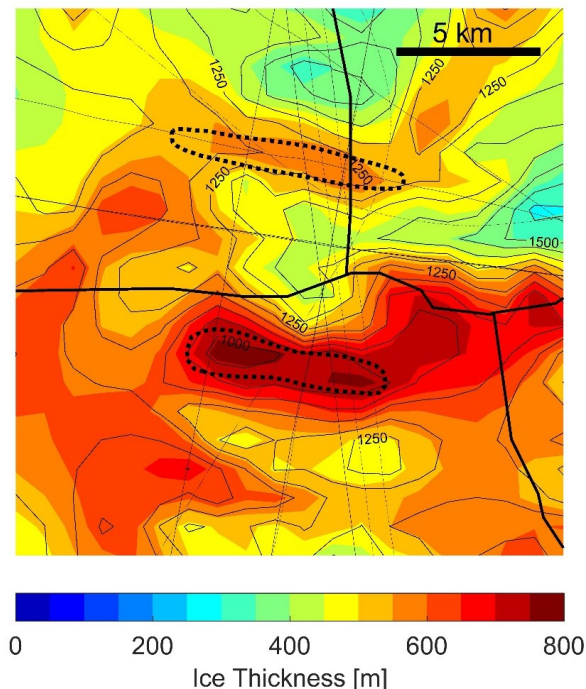


Figure S 3-2 Interpolated ice thickness near the DIC summit area. The ice thickness is overlain on bedrock elevation contours [m asl.]. Fine black lines indicate the location of the radar transects, whereas the thick black lines represent the ice divides. The locations of the subglacial lakes are indicated with dotted lines.

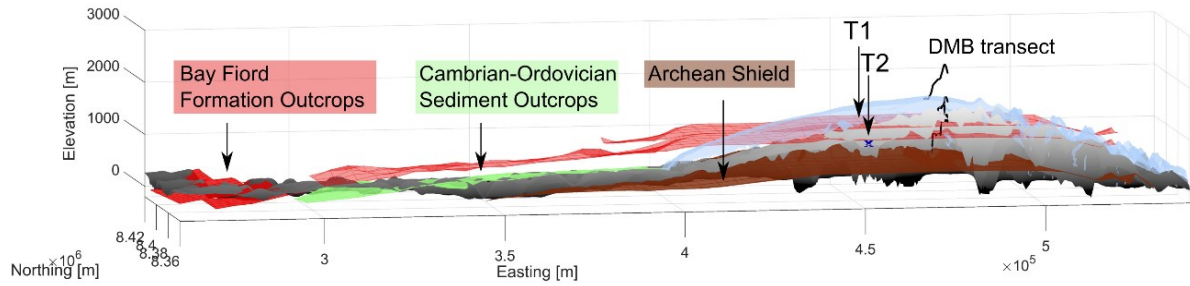


Figure S 3-3: 3D geology model. Three-dimensional reconstruction of the bedrock topography (greyscale) and ice surface (blue) of DIC and the geological formations as interpolated from the published geology [Harrison et al., 2016] into our geology model. Outcrops of the Bay Fiord Formation (red) and Cambrian-Ordovician sediments (green) are observed to the west of DIC, underlain by the Archean Shield. Interpolation of these outcrops reveals that the geological formations are dipping upwards and towards DIC, with the Bay Fiord Formation intersecting the bedrock in the vicinity of T1 and T2. The location of the transect used to derive the magnetics depth to basement (DMB) is shown in black.

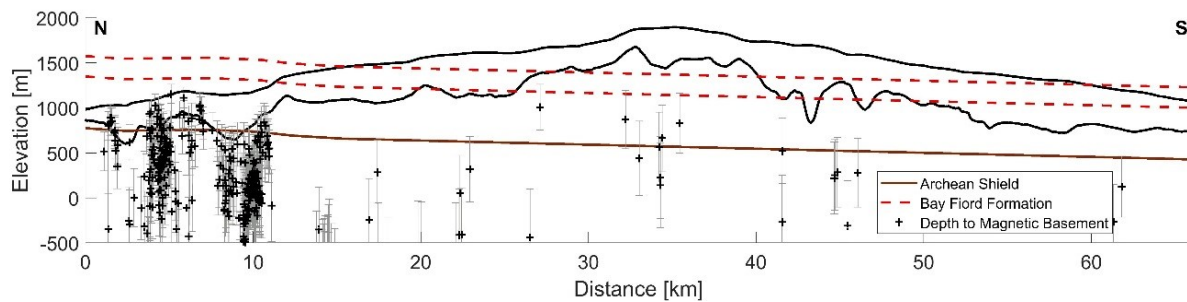


Figure S 3-4: Comparison of modeled geology and depth to magnetic basement solutions (DMB). The top of the Archean shield (basement, brown solid line) is compared to the depth to magnetic basement (DMB) solutions (black crosses) derived from airborne magnetics data recorded along a transect east of the subglacial lakes (Figure S 3-3). The black lines represent the ice surface and bedrock topography. The error bars of the DMB solutions represent a 20 % uncertainty of the distance between the source and sensor.

3.7 References

- Badgeley, J. A., E. C. Pettit, C. G. Carr, S. Tulaczyk, J. A. Mikucki, and W. B. Lyons (2017), An englacial hydrologic system of brine within a cold glacier: Blood Falls, McMurdo Dry Valleys, Antarctica, *J. Glaciol.*, 63, 1–14, doi:10.1017/jog.2017.16.
- Burgess, D. O., M. J. Sharp, D. W. F. Mair, J. a. Dowdeswell, and T. J. Benham (2005), Flow dynamics and iceberg calving rates of Devon Ice Cap, Nunavut, Canada, *J. Glaciol.*, 51(173), 219–230, doi:10.3189/172756505781829430.
- Carter, S. P., D. D. Blankenship, M. E. Peters, D. A. Young, J. W. Holt, and D. L. Morse (2007),

- Radar-based subglacial lake classification in Antarctica, *Geochemistry, Geophys. Geosystems*, 8(3), n/a-n/a, doi:10.1029/2006GC001408.
- Christner, B. C. et al. (2014), A microbial ecosystem beneath the West Antarctic ice sheet, *Nature*, 512(7514), 310–313, doi:10.1038/nature13667.
- Clifford, S. M. (1987), Polar basal melting on Mars, *J. Geophys. Res.*, 92(B9), 9135–9152, doi:10.1029/JB092iB09p09135.
- Cockell, C. S. et al. (2013), Subglacial Environments and the Search for Life Beyond the Earth, in *Antarctic Subglacial Aquatic Environments*, pp. 129–148, American Geophysical Union.
- CRISIS (2016), CRISIS, *Radar Depth Sounder Data*, Lawrence, Kansas, USA, Digital Media. <http://data.cresis.ku.edu/>
- Cuffey, K. M., and W. S. B. Paterson (2010), *The Physics of Glaciers*, Academic Press.
- Dowdeswell, J. A., T. J. Benham, M. R. Gorman, D. Burgess, and M. J. Sharp (2004), Form and flow of the Devon Island Ice Cap, Canadian Arctic, *J. Geophys. Res. Surf.*, 109(F2), doi:10.1029/2003JF000095.
- Gardner, A. S., M. J. Sharp, R. M. Koerner, C. Labine, S. Boon, S. J. Marshall, D. O. Burgess, and D. Lewis (2009), Near-surface temperature lapse rates over arctic glaciers and their implications for temperature downscaling, *J. Clim.*, 22(16), 4281–4298, doi:10.1175/2009JCLI2845.1.
- Grasby, S. E. et al. (2012), Geothermal energy resource potential of Canada, *Geol. Surv. Canada, Open File*, 6914, doi:10.4095/291488.
- Greenbaum, J. S. et al. (2015), Ocean access to a cavity beneath Totten Glacier in East Antarctica, *Nat. Geosci.*, 8(4), 294–298, doi:10.1038/ngeo2388.
- Hall, D. L., S. M. Sterner, and R. J. Bodnar (1988), Freezing point depression of NaCl-KCl-H₂O solutions, *Econ. Geol.*, 83, 197–202, doi:10.2113/gsecongeo.83.1.197.
- Harrison, J. C., T. Lynds, A. Ford, and R. H. Rainbird (2016), Geology, simplified tectonic assemblage map of the Canadian Arctic Islands, Northwest Territories - Nunavut, *Geol. Surv. Canada, Can. Geosci., Map 80*, doi:10.4095/297416.
- Howat, I. M., C. Porter, M. J. Noh, B. E. Smith, and S. Jeong (2015), Brief communication: Sudden drainage of a subglacial lake beneath the Greenland Ice Sheet, *Cryosphere*, 9(1),

103–108, doi:10.5194/tc-9-103-2015.

- Karl, D. M., D. F. Bird, K. Björkman, T. Houlihan, R. Shackelford, and L. Tupas (1999), Microorganisms in the accreted ice of Lake Vostok, Antarctica., *Science*, 286(5447), 2144–2147, doi:10.1126/science.286.5447.2144.
- Kinnard, C., C. M. Zdanowicz, D. a. Fisher, and C. P. Wake (2006), Calibration of an ice-core glaciochemical (sea-salt) record with sea-ice variability in the Canadian Arctic, *Ann. Glaciol.*, 44(May 1998), 383–390, doi:10.3189/172756406781811349.
- Ku, C. C., and J. A. Sharp (1983), Werner deconvolution for automated magnetic interpretation and its refinement using Marquardt's inverse modeling, *GEOPHYSICS*, 48(6), 754–774, doi:10.1190/1.1441505.
- Livingstone, S. J., C. D. Clark, J. Woodward, and J. Kingslake (2013), Potential subglacial lake locations and meltwater drainage pathways beneath the Antarctic and Greenland ice sheets, *Cryosphere*, 7(6), 1721–1740, doi:10.5194/tc-7-1721-2013.
- Lyons, W. B., K. A. Welch, G. Snyder, J. Olesik, E. Y. Graham, G. M. Marion, and R. J. Poreda (2005), Halogen geochemistry of the McMurdo dry valleys lakes, Antarctica: Clues to the origin of solutes and lake evolution, *Geochim. Cosmochim. Acta*, 69(2), 305–323, doi:10.1016/j.gca.2004.06.040.
- Mayr, U. (1980), Stratigraphy and correlation of lower Paleozoic formations, subsurface of Bathurst Island and adjacent smaller islands, Canadian Arctic Archipelago, *Geol. Surv. Canada, Bull.*, 306.
- Mikucki, J. A., and J. C. Priscu (2007), Bacterial diversity associated with Blood Falls, a subglacial outflow from the Taylor Glacier, Antarctica, *Appl. Environ. Microbiol.*, 73(12), 4029–4039, doi:10.1128/AEM.01396-06.
- Mikucki, J. A., C. M. Foreman, B. Sattler, W. Berry Lyons, and J. C. Priscu (2004), Geomicrobiology of blood falls: An iron-rich saline discharge at the terminus of the Taylor Glacier, Antarctica, *Aquat. Geochemistry*, 10(3–4), 199–220, doi:10.1007/s10498-004-2259-x.
- Mikucki, J. A., E. Auken, S. Tulaczyk, R. A. Virginia, C. Schamper, K. I. Sørensen, P. T. Doran, H. Dugan, and N. Foley (2015), Deep groundwater and potential subsurface habitats beneath an Antarctic dry valley, *Nat. Commun.*, 6(May 2014), 6831, doi:10.1038/ncomms7831.

- Murray, A. E. et al. (2012), Microbial life at -13°C in the brine of an ice-sealed Antarctic lake, *Proc. Natl. Acad. Sci.*, 109(50), 2–7, doi:10.1073/pnas.1208607109/-/DCSupplemental.www.pnas.org/cgi/doi/10.1073/pnas.1208607109.
- Palmer, S. J., J. A. Dowdeswell, P. Christoffersen, D. A. Young, D. D. Blankenship, J. S. Greenbaum, T. Benham, J. Bamber, and M. J. Siegert (2013), Greenland subglacial lakes detected by radar, *Geophys. Res. Lett.*, 40(23), 6154–6159, doi:10.1002/2013GL058383.
- Paterson, W. S. B. (1976), Vertical strain-rate measurements in an arctic ice cap and deductions from them, *J. Glaciol.*, 17(75), 3–12.
- Paterson, W. S. B., and G. K. C. Clarke (1978), Comparison of theoretical and observed temperature profiles in Devon Island ice cap, Canada, *Geophys. J. Int.*, 55(3), 615–632, doi:10.1111/j.1365-246X.1978.tb05931.x.
- Paterson, W. S. B., R. M. Koerner, D. Fisher, S. J. Johnsen, H. B. Clausen, W. Dansgaard, P. Bucher, and H. Oeschger (1977), An oxygen-isotope climatic record from the Devon Island ice cap, arctic Canada, *Nature*, 266(5602), 508–511, doi:10.1038/266508a0.
- Peters, M. E., D. D. Blankenship, and D. L. Morse (2005), Analysis techniques for coherent airborne radar sounding: Application to West Antarctic ice streams, *J. Geophys. Res. Solid Earth*, 110(B6), doi:10.1029/2004JB003222.
- Peters, M. E., D. D. Blankenship, S. P. Carter, S. D. Kempf, D. A. Young, and J. W. Holt (2007), Along-Track Focusing of Airborne Radar Sounding Data From West Antarctica for Improving Basal Reflection Analysis and Layer Detection., *IEEE Trans. Geosci. Remote Sens.*, 45(9), 2725–2736.
- Reeh, N., and W. S. B. Paterson (1988), Application of a flow model to the ice-divide region of Devon Island ice cap, Canada, *J. Glaciol.*, 34(116), 55–63.
- Schmidt, B. E., D. D. Blankenship, G. W. Patterson, and P. M. Schenk (2011), Active formation of ‘chaos terrain’ over shallow subsurface water on Europa, *Nature*, 479(7374), 502–505, doi:10.1038/nature10608.
- Schroeder, D. M., D. D. Blankenship, and D. A. Young (2013), Evidence for a water system transition beneath Thwaites Glacier, West Antarctica, *Proc. Natl. Acad. Sci.*, 110(30), 12225–12228, doi:10.1073/pnas.1302828110.
- Schroeder, D. M., D. D. Blankenship, R. K. Raney, and C. Grima (2015), Estimating subglacial

- water geometry using radar bed echo specularity: Application to Thwaites Glacier, West Antarctica, *IEEE Geosci. Remote Sens. Lett.*, *12*(3), 443–447, doi:10.1109/LGRS.2014.2337878.
- Schroeder, D. M., H. Seroussi, W. Chu, and D. A. Young (2016), Adaptively constraining radar attenuation and temperature across the Thwaites Glacier catchment using bed echoes, *J. Glaciol.*, *62*(236), 1075–1082, doi:10.1017/jog.2016.100.
- Shreve, R. L. (1972), Movement of Water in Glaciers, *J. Glaciol.*, *11*(62), 205–214.
- Skidmore, M., S. P. Anderson, M. Sharp, J. Foght, and B. D. Lanoil (2005), Comparison of microbial community compositions of two subglacial environments reveals a possible role for microbes in chemical weathering processes., *Appl. Environ. Microbiol.*, *71*(11), 6986–97, doi:10.1128/AEM.71.11.6986-6997.2005.
- Willis, M. J., B. G. Herried, M. G. Bevis, and R. E. Bell (2015), Recharge of a subglacial lake by surface meltwater in northeast Greenland, *Nature*, *518*(7538), 223–227, doi:10.1038/nature14116.
- Wright, A., and M. Siegert (2012), A fourth inventory of Antarctic subglacial lakes, *Antarct. Sci.*, *24*(06), 659–664, doi:10.1017/S095410201200048X.
- Wyatt, F. R., and M. J. Sharp (2015), Linking surface hydrology to flow regimes and patterns of velocity variability on Devon Ice Cap, Nunavut, *J. Glaciol.*, *61*(226), 387–399, doi:10.3189/2015JoG14J109.
- Van Wychen, W., J. Davis, L. Copland, D. O. Burgess, L. Gray, M. Sharp, J. A. Dowdeswell, and T. J. Benham (2017), Variability in ice motion and dynamic discharge from Devon Ice Cap, Nunavut, Canada, *J. Glaciol.*, *63*(239), 436–449, doi:10.1017/jog.2017.2.
- Young, D. A., D. M. Schroeder, D. D. Blankenship, S. D. Kempf, and E. Quartini (2016), The distribution of basal water between Antarctic subglacial lakes from radar sounding, *Philos. Trans. R. Soc. A Math. Phys. Eng. Sci.*, *374*(2059), 20140297, doi:10.1098/rsta.2014.0297.
- Young, D. A. et al. (2017), High resolution boundary conditions of an old ice target near Dome C, Antarctica, *Cryosph.*, (July), 1–16, doi:10.5194/tc-2016-169.

Chapter 4

Evidence for an extensive subglacial brine network under the Devon Ice Cap, Canadian Arctic

4.1 Abstract

A recent study presented the first evidence for the existence of two hypersaline subglacial lakes beneath a cold-based region of the Devon Ice Cap (DIC), Canadian Arctic. The lakes likely derive their salinity from dissolution of a salt-bearing evaporite unit that outcrops beneath the ice. Subglacial lakes have long been of interest with respect to the search for life on other icy planetary bodies. Due to their hypersaline and cold conditions, the subglacial lakes beneath DIC represent unique analogs for brines inferred to exist on Europa and Mars, and are therefore particularly compelling targets for in-situ investigations of their biology and biogeochemistry. However, due to the limited coverage of the geophysical data used to identify the lakes, the full extents of the lakes and the hydrological conditions in the area around them remain poorly constrained. Here, we present results from a targeted airborne geophysical survey (radar sounding and laser altimetry) to re-evaluate the evidence for the existence of these subglacial lakes, derive their full extents, and investigate their relationship to the surrounding subglacial environment. Our results strongly support the evidence for one of the subglacial lakes, for which we delineate new shorelines that define a lake with a total area of 23.2 km². Furthermore, we hypothesize that extensive areas of wet beds beneath the central and western sectors of DIC are part of a brine-network, where water is concentrated in small ponds, thin films, or saturated permeable sediments. The other subglacial lake previously hypothesized likely forms part of this brine-network, as we find evidence that suggests it is not a deep water body. We suggest that the characteristics of this brine-network are related to the bedrock lithology and topography.

4.2 Introduction

The ~14,400 km² Devon Ice Cap (DIC) [Burgess and Sharp, 2004] is one of the largest ice caps in the Canadian Arctic. DIC is underlain by rugged mountainous terrain that reaches above 1700 m above sea level (asl.) near its center and flattens towards its western margin [Dowdeswell *et al.*, 2004; Rutishauser *et al.*, 2018]. While a number of marine-terminating outlet glaciers drain towards the northern, southern and eastern margins of the ice cap, ice in the ice cap interior is slow-flowing, with velocities below 20 m/yr, and is considered to be cold-

based with ice frozen to the underlying bedrock [*Paterson and Clarke, 1978; Burgess et al., 2005; Van Wychen et al., 2017*].

Despite the cold-based interior, a recent study presented geophysical and geological evidence for the existence of two hypersaline subglacial lakes [*Rutishauser et al., 2018*] situated in bedrock troughs (referred to as T1 and T2) beneath 560-740 m of ice near the centre of DIC (Figure 4-1). These subglacial lakes were identified by radio-echo sounding (RES), a tool that has been widely used to identify subglacial water [e.g. *Carter et al., 2007, 2009; Palmer et al., 2013; Schroeder et al., 2015; Young et al., 2016; Chu et al., 2018*]. Modeled basal ice temperatures in the vicinity of T1 and T2 are well below the pressure melting point, suggesting that the lakes consist of hypersaline water, and that the salinity significantly depresses the freezing point of the subglacial water [*Rutishauser et al., 2018*]. *Rutishauser et al. (2018)* showed that an evaporite-rich sediment unit (Bay Fiord Formation) containing a bedded salt sequence [*Mayr, 1980*] likely outcrops beneath the ice near the subglacial lakes, and is therefore presumed to be the solute source for the brine.

Numerous subglacial lakes have been identified beneath the Antarctic [e.g. *Wright and Siegert, 2013; Siegert et al., 2016*] and Greenland ice sheets [*Palmer et al., 2013; Howat et al., 2015; Willis et al., 2015*], however, these lakes are considered to consist of fresh water. Thus, the hypersaline subglacial lakes beneath DIC are unprecedented and are considered to be the only spatially isolated brine-rich subglacial lakes so far identified on Earth [*Rutishauser et al., 2018*]. The only comparable subglacial fluid reported to date is the brine found beneath Taylor Glacier, Antarctica. However, this brine is associated with a salt-rich groundwater system rather than representing a spatially isolated subglacial lake [e.g. *Hubbard et al., 2004; Mikucki et al., 2004; Badgeley et al., 2017*].

In-situ sampling has shown that subglacial aquatic environments, both fresh and saline, are viable microbial habitats despite their extreme conditions and isolation from the atmosphere [*Karl et al., 1999; Skidmore et al., 2005; Mikucki and Priscu, 2007; Christner et al., 2014; Boetius et al., 2015*]. Terrestrial subglacial water systems and lakes are therefore considered to be potentially good analogs for icy habitats on other planetary bodies where liquid water may exist [e.g. *Cockell et al., 2013; Garcia-Lopez and Cid, 2017*]. The hypersaline nature of the subglacial lakes beneath DIC makes them particularly tantalizing analogs for brine bodies inferred to exist within Europa's ice shell [*Schmidt et al., 2011*] or beneath the Martian South Polar Layered Deposits [*Orosei et al., 2018*]. The subglacial lakes beneath DIC therefore represent compelling targets for further characterization and in-situ biogeochemical

investigations to explore the potential for, and limitations of, life in such extreme conditions. Exploration of these lakes can therefore help to assess the habitability of similar icy environments across the solar system.

Rutishauser et al. (2018) defined the shorelines of the subglacial lakes beneath DIC based on the occurrence of hydraulically flat, bright and specular (mirror-like) radar reflections at the glacier bed. These criteria have all been used previously to identify subglacial lakes [e.g. *Carter et al.*, 2007]. Nevertheless, although the radar reflections over T1 were highly specular, no hydraulic potential minimum was observed. This suggests that the T1 trough may contain either shallow water or water-saturated sediments, rather than a deep water body [*Rutishauser et al.*, 2018]. However, due to the relatively sparse coverage of the available radar data, questions remain regarding both the true nature and extent of the subglacial water bodies, and the hydrological conditions in the area around them.

Here, we use results from a new, targeted airborne geophysical survey over DIC to evaluate the previous hypothesis for the existence of two subglacial lakes [*Rutishauser et al.*, 2018], to identify the full extents of the lakes, and to characterize the subglacial environment that surrounds them. We utilize radar-derived basal reflectivity anomalies to identify areas of subglacial water, and the hydraulic flatness of these areas to evaluate the likelihood that they represent deep water bodies. Our results show that the lake in T2 is larger than previously reported [*Rutishauser et al.*, 2018], and suggest that an extensive brine-network covers large areas beneath DIC. Based on these results, the previously-proposed lake boundaries are refined, and the relationships between the characteristics of the brine-network, the geological context, ice cap bed morphology, and expected subglacial water flow pathways are discussed.

4.3 Data and Methods

Data used in this study were collected during an airborne geophysical survey over DIC in spring 2018, hereby referred to SRH1. The survey equipment consisted of an ice penetrating radar sounder, a laser altimeter, and a magnetometer installed on a Basler BT-67 (DC-3T) aircraft operated by Kenn Borek Air Ltd. A total of 4415 km of along-track data were acquired from a grid survey over the center of DIC. Line spacing ranged from 1.25 km to 5 km, with the densest grid centered over the area containing previously identified lakes (Figure 4-1).

4.3.1 Radar sounding data

Radar data were acquired with the High-Capability Radar Sounder (HiCARS), operated by the University of Texas Institute for Geophysics (UTIG). The radar is a coherent system with a 60

MHz center frequency (5 m wavelength in air) and a 15 MHz bandwidth. Detailed instrument characteristics and processing techniques are described in [Peters *et al.*, 2005]. Here, we use unfocused SAR processed data to derive basal reflectivities and subglacial bedrock topography. The bed return is identified using a semi-automated picking algorithm which locates the maximum bed reflection power within manually-defined depth boundaries. Travel times were converted to depths using a radar wave velocity in ice of 168.4 m/ μ s. Travel-time effects resulting from the existence of a less dense near-surface firn layer are neglected, but could potentially contribute between 2.3-4.5m for a 30 m thick firn layer with a density between 610-760 kg/m³ [Rutishauser *et al.*, 2016].

The vertical resolution of the radar data ($\delta v = c/(2B\sqrt{\epsilon})$) is a function of the bandwidth ($B = 15$ MHz), the speed of light (c) and the permittivity of ice ($\epsilon = 3.17$ [e.g. Evans, 1965]) and is about 5.6 m in ice for the HiCARS instrument. The nominal along-track trace spacing is a function of aircraft speed and trace stacking, and was calculated to be about 21.7 m. The full bed return at each trace is affected by basal properties within the pulse-limited footprint diameter $D_{pl} = 2\sqrt{c/B\left(h + \frac{d}{\sqrt{\epsilon}}\right)}$, where h is the aircraft clearance above the ice surface and d is the ice thickness. The average footprint diameter from this survey is 274 m. Small subglacial hydrological features such as channels or concentrated patches of water with dimensions below this footprint diameter may not be resolved. Bed elevations from this dataset result in a mean crossover error of 9 m. The bed elevation data were combined with data used to produce a previous digital elevation model (DEM) of the bed [Rutishauser *et al.*, 2018] to generate a new bed DEM over a 500 m grid mesh, computed via triangular linear interpolation of all bed elevations.

4.3.2 Basal reflectivity

Radar-derived measurements of basal reflectivity have been widely used to identify the presence of subglacial water [e.g. Peters *et al.*, 2005; Carter *et al.*, 2007; Jacobel *et al.*, 2009; Chu *et al.*, 2018]. The basis for such interpretations is that an ice-water interface will have a higher reflectivity than surrounding areas where ice is in direct contact with dry bedrock. The theoretical contrast in Fresnel reflectivity between wet and dry beds is estimated to be about 10-15 dB [Peters *et al.*, 2005], and is a function of the permittivity of the bed material. However, the thresholds that have been used in the literature to differentiate between subglacial water or wet beds and surrounding areas with dry bedrock are highly variable, ranging between 2 and

26 dB [Oswald and Gogineni, 2008; Carter et al., 2009; Jacobel et al., 2010; Wolovick et al., 2013; Chu et al., 2016].

Since bed reflectivity values derived from radar measurements are also affected by the characteristics of the radar system and englacial attenuation processes, a number of corrections are required before basal reflectivity values can be interpreted in terms of subglacial hydrological conditions [e.g. Matsuoka et al., 2010a, 2012; Wolovick et al., 2013; Chu et al., 2016; Schroeder et al., 2016a]. Here, we derive the relative basal reflectivity (R) following

$$[R]_{dB} = [P]_{dB} + [B]_{dB} + [G]_{dB} + [L]_{dB} - [S]_{dB}, \quad (1)$$

where P is the returned bed power, B are birefringence effects due to variations of the ice crystal fabric [e.g. Matsuoka et al., 2003], G is the power loss from geometric spreading of the radar beam, L is the loss from englacial attenuation, and S is the correction for power variations in the radar system, where the notation $[]_{dB}$ refers to the terms expressed in decibels ($[X]_{dB} = 10 \log_{10}(X)$) [e.g. Matsuoka et al., 2012]. Here, S is assumed to be constant as no changes were made to the radar instrument settings during the field campaign. Under the assumption of a relatively uniform pattern of crystal fabric orientation over the survey area, we assume that birefringence effects are relatively constant, and thus neglect both terms S and B when analyzing relative basal reflectivities. The power loss from geometric spreading is derived from

$$[G]_{dB} = 2[2(h + d/\sqrt{\epsilon})]_{dB}, \quad (2)$$

where λ is the radar wavelength in air, h is the aircraft range above the glacier surface, d is the ice thickness, and $\epsilon = 3.17$ [e.g. Evans, 1965] is the dielectric permittivity of ice [Schroeder et al., 2016a]. The englacial attenuation loss term L is related to the one-way depth-averaged attenuation rate N via

$$[L]_{dB} = 2Nh. \quad (3)$$

N is derived from a model exploring the Arrhenius relationship between ice temperature and ice impurity concentration as well as from a linear relationship between the ice thickness and the geometrically corrected bed power (see Section 4.3.3). Inserting equations (2) and (3) into equation (1) leads to relative basal reflectivity estimates:

$$[R]_{dB} = [P]_{dB} + 2[2(h + d/\sqrt{\epsilon_{ice}})]_{dB} + 2Nh, \quad (4)$$

where we express the resulting basal reflectivity relative to the median of all observed reflectivities from this dataset. The uncertainty of the measured bed reflectivities is estimated from the mean crossover error of the geometrically corrected bed power values along the survey profiles, leading to an uncertainty of 5.2 dB.

Although *Rutishauser et al.* (2016) showed that spatially variable radar scattering occurs from ice-layers within the near-surface firn over DIC, we ignore potential energy losses from scattering within the firn. When applied to Thwaites Glacier, Antarctica, a correction for scattering losses in the firn revealed that the firn losses were significantly less than the englacial losses [*Schroeder et al.*, 2016b]. We thus neglect potential firn losses, although we do analyze the pattern of basal reflectivities in relation to previous firn scattering observations [*Rutishauser et al.*, 2016], and acknowledge that the question of firn losses over DIC requires further investigation.

To distinguish radar signals indicative of wet beds, we use a 12 dB reflectivity threshold. This corresponds to the theoretical Fresnel reflectivity increase between a dry and wet bed for the dielectric permittivity of seawater [*Neal*, 1979; *Peters et al.*, 2005], and is 1.6 standard deviations from the median value of all measured bed reflectivities. Permittivity values of water are dependent on the water temperature and salinity, and on the frequency of the electromagnetic wave emitted by the radar instrument, and are typically estimated from laboratory experiments. Thus, the permittivity and reflection coefficient for seawater might not represent the true value for the dielectric properties of the brine hypothesized beneath DIC. However, it is likely a good approximation. Seawater permittivity was also used to approximate the dielectric properties of the brine beneath Taylor Glacier, Antarctica [*Badgeley et al.*, 2017], which may have properties similar to the brine hypothesized to exist beneath DIC [*Rutishauser et al.*, 2018].

For visualization purposes only, we include the radar data collected by NASA's Operation IceBridge that were previously used to identify the subglacial lakes [*CReSIS*, 2016; *Rutishauser et al.*, 2018]. In order to account for the differences in instrument parameters, we apply shifts of 48.6 dB and -37.7 dB respectively to the data collected with the University of Kansas Multichannel Coherent Radar Depth Sounder (MCoRDS) [*CReSIS*, 2016] in 2011 and 2012. This corresponds to the mean crossover differences in basal reflectivities compared to the SRH1 dataset.

4.3.3 Derivation of radar attenuation rates

Radar attenuation rates are a function of the electrical conductivity throughout the ice column, which is primarily controlled by ice temperature, and somewhat affected by ice chemistry for the frequency range of ice penetrating radar sounding measurements [e.g. *Corr et al.*, 1993; *Matsuoka et al.*, 2010a; *MacGregor et al.*, 2012, 2015]. Regional scale attenuation rates have been estimated from empirical relationships between the returned bed power and the thickness of the overlying ice column [e.g. *Gades et al.*, 2000; *Jacobel et al.*, 2009; *Wolovick et al.*, 2013]. Under the assumption of locally constant attenuation rates, this method allows a direct derivation of englacial attenuation from the radar measurements and does not require knowledge of ice temperature and chemistry. However, due to spatial variations in ice temperatures, and potentially also in impurity concentrations in the ice, attenuation rates are rarely uniform over large survey areas [e.g. *MacGregor et al.*, 2007, 2012, 2015; *Matsuoka*, 2011; *Schroeder et al.*, 2016a]. Most importantly, spatial variations in attenuation rates can exceed the theoretical reflectivity contrast between wet and dry beds [e.g. *Matsuoka*, 2011; *MacGregor et al.*, 2012], highlighting the importance of correcting for variable attenuation rates in order to derive meaningful reflectivity values for subglacial hydrological analyses. In order to retain spatial variations in ice properties that affect englacial attenuation, several studies have used modeling approaches in which conductivity is estimated as a function of spatially varying ice temperature and chemistry [e.g. *Corr et al.*, 1993; *MacGregor et al.*, 2007, 2012, *Matsuoka et al.*, 2010b, 2012; *Jordan et al.*, 2016]. These conductivity models explore the Arrhenius-form temperature dependencies of the ice conductivity, with the attenuation rates being an exponential function of the inverse of ice temperatures, and a linear function of impurity concentrations (see Eq. (6)). Other studies have used englacial layers and depth-dependent changes in their returned power to estimate spatially-varying attenuation rates [*Matsuoka et al.*, 2010a; *MacGregor et al.*, 2015]. This method requires the presence of bright and isolated internal layers in the radar data which are not observed in our dataset, and is therefore not applicable in this study.

Here, we model attenuation rates using an Arrhenius-type conductivity model that was introduced for the Greenland Ice Sheet by *MacGregor et al.*, (2015) (referred to as the M07 model), but with ice impurity concentrations adapted for DIC. For comparison, we also derive radar-inferred attenuation rates from localized linear fits between bed reflection power and ice thickness.

4.3.4 Arrhenius modeled attenuation rates

The radar attenuation rate N_a is proportionally related to the high-frequency limit of the electrical conductivity σ_∞ measured in μSm^{-1}

$$N_a = \frac{10 \log_{10} e}{1000 \epsilon_0 c \sqrt{\epsilon}} \sigma_\infty, \quad (5)$$

where ϵ_0 and c are the permittivity and the speed of light in vacuum, respectively [Winebrenner *et al.*, 2003; MacGregor *et al.*, 2012, 2015]. The electrical conductivity σ_∞ is related to ice temperature and impurity concentration via the Arrhenius-type conductivity model

$$\begin{aligned} \sigma_\infty = & \sigma_{pure} \exp \left[\frac{E_{pure}}{k} \left(\frac{1}{T_r} - \frac{1}{T} \right) \right] \\ & + \mu_{H^+} [H^+] \exp \left[\frac{E_{H^+}}{k} \left(\frac{1}{T_r} - \frac{1}{T} \right) \right] \\ & + \mu_{Cl^-} [Cl^-] \exp \left[\frac{E_{Cl^-}}{k} \left(\frac{1}{T_r} - \frac{1}{T} \right) \right] \\ & + \mu_{NH_4^+} [NH_4^+] \exp \left[\frac{E_{NH_4^+}}{k} \left(\frac{1}{T_r} - \frac{1}{T} \right) \right], \end{aligned} \quad (6)$$

where $k = 1.38 \times 10^{-23} \text{JK}^{-1}$ is the Boltzmann constant, T is the ice temperature, T_r is a reference temperature, and σ_{pure} and E_{pure} are the conductivity and activation energy for pure ice, respectively [MacGregor *et al.*, 2015]. μ_x is the molar conductivity, $[x]$ is the molarity and E_x is the activation energy for the respective impurities H^+ , Cl^- and NH_4^+ . Impurity concentrations were derived from average concentrations measured along a 20 m deep firn core that was retrieved from DIC in 2015 [Criscitiello *et al.*, in prep.]. All parameters and dielectric properties used in the model are given in Table 4-1.

Ice temperatures are estimated from a one-dimensional (1D) steady-state advection-diffusion model [Cuffey and Paterson, 2010] with similar input parameters as previously described in Rutishauser *et al.* (2018): An estimated geothermal heat flux of $65 \pm 5 \text{ mW m}^{-2}$ [Grasby *et al.*, 2012], a long-term accumulation rate of $0.19 \pm 0.05 \text{ m water equivalent per year}$ [Paterson, 1976; Reeh and Paterson, 1988], and a mean annual air temperature of $-23 \pm 1^\circ\text{C}$ at a reference elevation of 1825 m asl. [Kinnard *et al.*, 2006] and interpolated to all elevations using a 4.1°C/km lapse rate [Gardner *et al.*, 2009; Rutishauser *et al.*, 2018]. This temperature model assumes no horizontal temperature exchanges and no heat generation other than the geothermal heat flux, thus ignoring basal frictional heating, strain heating from ice deformation and

potential release of latent heat from freezing of percolated meltwater in the firn. However, following previous flow regime classifications [Burgess *et al.*, 2005; Van Wychen *et al.*, 2017], we find that 95.7% of our data lies within flow regime 1 (FR1, $\frac{v}{d} \leq 0.05 \text{ yr}^{-1}$, where v is the ice surface velocity) for which ice is expected to be frozen to the glacier bed and ice flow is solely driven by internal deformation (likely concentrated near the bed). Furthermore, the average ice surface velocity (derived from Van Wychen *et al.*, (2014)) over the survey lines in the area classified as FR1 is 7.9 m/yr. We therefore assume that the underlying assumptions for a 1D advection-diffusion model are valid for FR1, and exclude the few data points outside this area from the reflectivity analysis. A comparison to a temperature profile measured in 1972 near the summit of DIC [Paterson and Clarke, 1978] shows that the modeled ice temperatures are in good agreement with the measurements (Figure 4-2).

For simplification, depth-averaged ice temperatures \hat{T} are used to derive depth-averaged attenuation rates in Eq. (6), where \hat{T} is obtained via the depth integral over the modeled ice temperature profile T at depth z

$$\hat{T} = \frac{1}{d} \int_0^d T(z) dz, \quad (7)$$

where d is the ice thickness. The average difference between inserting depth-averaged ice temperatures in Eq. (6) and multiplying by the ice thickness, versus deriving attenuation rates over the modeled depth-temperature profiles is 0.11 dB, which is minimal and therefore justifies this simplification.

The resulting modeled depth-averaged ice temperatures over the study area range between -22 °C and -15 °C (Figure 4-3a). Inserting these ice temperatures in the Arrhenius model (Eq. (5) to (7)) results in depth-averaged one-way attenuation rates ranging from 13.5 dB/km near the center of DIC to 22.2 dB/km towards the ice cap margins (Figure 4-4).

Uncertainties in the attenuation rates potentially arise from uncertainties in the modeled ice temperatures, from the assumption of constant impurity concentration over DIC, and from the assumption of constant impurity composition with depth. Propagating the ice temperature model uncertainties results in a mean depth-averaged ice temperature uncertainty of 3.14 °C. Further propagating the ice temperature uncertainties at each location leads to an average total two-way attenuation uncertainty of 3.29 dB (integrated over the entire ice column), which is below the bed power measurement uncertainty. Uncertainties from spatially- and depth varying impurity concentrations are ignored as changes and uncertainties in temperatures are likely

larger and have the dominant effect on attenuation rates (the ice temperature is the dominating factor in the Arrhenius relationship). Furthermore, ice temperatures, and thus attenuation rates are expected to be relatively uniform over the relatively small spatial area containing the hypothesized subglacial lakes. Relative reflectivity anomalies from these areas are therefore not expected to be significantly affected by uncertainties in englacial attenuation.

4.3.5 Radar-inferred attenuation rates

Radar inferred attenuation rates are derived from a linear fit between the ice thicknesses and geometrically corrected bed reflection power [e.g. *Gades et al.*, 2000; *Jacobel et al.*, 2009; *Wolovick et al.*, 2013; *Schroeder et al.*, 2016a]. To better comply with the underlying assumption of constant attenuation rates over the sampled area, we constrain the sample region as a function of the modeled depth-averaged ice temperatures. This approach is somewhat similar to the method introduced by *Schroeder et al.*, (2016a) where the sample window is minimized along the radar profiles, and to the method introduced by *Jordan et al.*, (2016) where a moving sampling window is constrained by Arrhenius modeled attenuation rates. Here, we define sample regions as areas in which the depth-averaged ice temperatures lie within a 1 °C range (e.g. all data points with depth-averaged ice temperatures between -22 °C and -21 °C), with the 1 °C window repeated every 0.1 °C between -22°C and -16 °C. Attenuation rates for each sample region are then derived via the correlation-coefficient magnitude (C) between ice thickness and bed power, following *Schroeder et al.*, (2016a). C is calculated for a sweep of attenuation rates between 0-40 dB/km, and the local attenuation rate is found where C reaches a minimum, meaning that the bed power and the ice thickness and are perfectly anti-correlated, and that losses from englacial attenuation are accounted for [*Schroeder et al.*, 2016a]. To ensure meaningful derivation of correlation-coefficient derived attenuation rates, we require that $C_0 \geq 0.5$, $C_w \leq 0.1$ and $N_h \leq 3$ dB, where C_0 is the uncorrected correlation-coefficient magnitude, N_h is the half-width of the correlation minimum that falls below the correlation coefficient magnitude C_w , and is also an expression of uncertainty [*Schroeder et al.*, 2016a]. Sample windows where these thresholds are not met are disregarded. A detailed description of this correlation-coefficient method can be found in *Schroeder et al.*, (2016a).

The resulting radar-inferred attenuation rates show a trend of increasing attenuation with increasing ice temperature, however, the rate of increase is stronger, and attenuation rates are between 0.6-20 dB/km higher than the Arrhenius modeled attenuation rates (Figure 4-4). Other studies also observed misfits between radar-derived and modeled attenuation rates over the Greenland Ice Sheet [*MacGregor et al.*, 2015; *Jordan et al.*, 2016], although the differences are

smaller than for this study. For Greenland, the discrepancy is hypothesized to be related to the frequency dependence of σ_∞ , and attenuation rates were corrected by applying a constant offset [MacGregor *et al.*, 2015]. Additionally, in southern Greenland, the difference was attributed to arise from spatial changes in the fraction of Holocene ice in the ice column, where the attenuation in Holocene ice is predicted to be higher due to a higher acidity [MacGregor *et al.*, 2015]. Investigating the causes for the misfit in our dataset is beyond the scope of this study, however, we believe that further investigation is necessary while also representing an opportunity to better understand radar attenuation losses and their frequency and temperature dependence. Furthermore, a detailed investigation of the radar-inferred attenuation rate and potentially adjusting the Arrhenius model input parameters, or evaluating the Arrhenius relationship itself may help to constrain the spatial pattern of ice temperature and impurity concentrations across DIC.

For the purposes of this study, we assume that the general trend of the Arrhenius modeled attenuation rates is more likely to be realistic than is the steep increase in attenuation with temperature that is suggested by the radar-derived values. To best conform with results from both methods, we best fit the Arrhenius curve to the radar derived attenuation rates by applying a multiplication factor m of 1.4, and use

$$N = mN_a = 1.4 \frac{10 \log_{10} e}{1000 \epsilon_0 c \sqrt{\epsilon}} \sigma_\infty \quad (8)$$

instead of Eq. (5). Resulting depth-averaged one-way attenuation rates range between 18.9 – 31.1 dB/km and are shown in Figure 4-3b.

4.3.6 Subglacial hydraulic head and water flow paths

The flow of subglacial water is controlled by the subglacial hydraulic head which is a function of the bedrock topography, the density of the subglacial fluid, and the overlying ice pressure. Subglacial water flows along gradients in the hydraulic head and has the potential to pool in hydraulically flat areas. Hydraulic flatness has therefore been used as criteria to identify subglacial water bodies [e.g. Carter *et al.*, 2007; Langley *et al.*, 2011]. Under the assumption that the subglacial water pressure equals the ice overburden pressure, the hydraulic head θ can be derived as

$$\theta = \left(\frac{\rho_i}{\rho_b} \right) S + \left(1 - \frac{\rho_i}{\rho_b} \right) B \quad (9)$$

where S is the ice surface elevation [m], B is the bed elevation [m], and ρ_i and ρ_b are the densities of ice (917 kg/m^3) and subglacial brine (1150 kg/m^3 , corresponding to a brine with 15 weight % NaCl [Rutishauser *et al.*, 2018]), respectively [Shreve, 1972; Wolovick *et al.*, 2013]. The ice surface elevation is derived from airborne laser altimetry measurements, and from the radar surface return in areas where no laser measurements are available (e.g. due to cloud cover). To reduce small scale roughnesses in the radar-derived ice surfaces, which are likely caused by near-surface firn heterogeneities [Rutishauser *et al.*, 2016], we apply a moving average filter with an 800 m window length, corresponding to approximately two times the average ice thickness. The hydraulic head is derived along the flight lines as well as over a 500 m grid mesh, using bed and surface DEMs generated via bilinear interpolation of the ice surface and bed elevations resulting from the SRH1 dataset. To compute the hydraulic head for orthometric heights, the surface and bed elevations were corrected for changes in the geoid, using the Arctic Gravity Project geoid [Arctic Gravity Project, 2006]. Uncertainties of the hydraulic head are derived by propagating the mean crossover errors in the measured ice surface (4 m, assuming radar derived ice surfaces) and bed elevations (9 m) through Eq. (9). Additionally, nominal gridding errors of 0.97 m and 3.96 m are added, representing the residuals of the interpolated surface and bed elevations, respectively. The resulting total uncertainty of the gridded hydraulic head is 6.6 m. To identify hydraulically flat areas in which ice is potentially afloat above subglacial water bodies, we derive the slope of the hydraulic head ($\tan \nabla \theta$) and use the slope uncertainty (0.75°) as the upper threshold for what we define as ‘hydraulically flat’.

An important implication to note is that the bedrock topography has a much larger effect on the hydraulic head when the subglacial fluid is considered to be brine than it does if the fluid is fresh water. For fresh water, the relative importance of the bed topography compared to the ice surface topography is about 1/11 whereas, for a subglacial brine with a density of 1150 kg/m^3 , it is about 1/4. This implies that brine-rich subglacial water bodies are likely to be topographically controlled, with water pooling in bedrock troughs. Although evidence suggests that subglacial water beneath DIC is brine-rich [Rutishauser *et al.*, 2018], we also reconstructed the pattern of hydraulically flat areas that would be expected if the subglacial fluid were fresh water (1000 kg/m^3). In general, the locations of the hydraulically flat areas identified for the fresh water case are similar to those identified for the case of a subglacial brine. However, over trough T2, where the basal reflectivity supports the presence of a subglacial lake (see Sections 4.4.2 and 4.5), the area with flat hydraulic head for freshwater extends over the southern valley wall of T2 (Figure S 4-1). In comparison, the hydraulically flat area when

considering a fluid with the density of brine is mostly limited to the center of the trough. We found no radar evidence for the presence of subglacial water outside the trough center (see Section 4.5), and thus believe that the hydraulic head distribution computed for subglacial brine is more consistent with the radar observations than is that computed for fresh water, suggesting that the assumption that the subglacial fluid is brine-rich is reasonable.

Potential flow paths for subglacial water are derived via application of a flow accumulation algorithm by TopoToolbox [*Schwanghart and Kuhn, 2010*] to the hydraulic head distribution. In this algorithm flow paths are identified from all grid cells that drain a minimum of 10 upstream cells. To test the sensitivity of the water routing model to uncertainties in the hydraulic head, we ran the flow accumulation model 100 times with randomly perturbed hydraulic heads by adding normally distributed errors with a standard deviation equal to the hydraulic head uncertainty (Figure S 4-2). Only when the perturbation amplitudes are increased to 2-3 times the uncertainty of the hydraulic head, do some changes occur in the reconstructed subglacial water flow routes.

4.3.7 Basal roughness

Subglacial roughness is dependent on several factors. Ice dynamics, including the direction and speed of ice flow that drive basal erosion, while the bedrock lithology also affects rates of erosion, with soft beds being more readily erodible than hard beds. The geological structure may also play a role, with features such as fault zones shaping the large-scale basal topography [e.g. *Siegert et al., 2005*]. On a scale comparable to the wavelength of the emitted electromagnetic radar pulse, the basal roughness affects the ratio between the proportions of specularly (mirror-like) and diffuse (scattered) reflected energy, where diffuse scattering of the radar wave is increased with increasing interface roughness [*Boithias, 1987; Peters et al., 2005*]. Over an ice-water interface, which is expected to be smooth compared to the surrounding ice/dry-bedrock interface, the reflected radar signal is expected to have a high specularity content. High specularity has therefore been used as a criterion to identify areas of basal water [*Oswald and Gogineni, 2008, 2012; Schroeder et al., 2013; Jordan et al., 2017; Oswald et al., 2018*] and subglacial lakes [e.g. *Carter et al., 2007; Young et al., 2017*], and was previously observed over the hypothesized subglacial lake in bedrock trough T1 [*Rutishauser et al., 2018*].

The specularity content can be derived from the shape of the waveform returned from the basal reflection (e.g. abruptness) [*Oswald and Gogineni, 2008, 2012; Jordan et al., 2017; Oswald et al., 2018*], or from variations in the angular distribution of scattered energy along the radar

flight lines [Schroeder *et al.*, 2013; Young *et al.*, 2016]. We currently do not have such radar-inferred basal roughness estimates for the SRH1 dataset. Instead, we compute basal roughness estimates from the root-mean square deviation (RMSD) of the bedrock topography along flight lines [e.g. Shepard *et al.*, 2001; MacGregor *et al.*, 2013; Jordan *et al.*, 2017] via

$$v(\Delta x) = \sqrt{\frac{1}{N} \sum_{i=1}^N [\bar{z}_b(x_i) - \bar{z}_b(x_i + \Delta x)]^2}, \quad (10)$$

where \bar{z}_b is the detrended bed elevation over the chosen window length, Δx is the horizontal lag between elevation points and N is the number of sample points within the window [Shepard *et al.*, 2001]. We derive the RMSD for lags Δx between 50 and 1000 m over 5 km window lengths repeated at every bedrock observation.

Numerous studies have indicated that subglacial terrains exhibit self-affine behavior [e.g. MacGregor *et al.*, 2013; Jordan *et al.*, 2017], meaning that the vertical scale of the basal roughness increases with a lower rate than the horizontal length scale [e.g. Shepard *et al.*, 2001]. This power-law relationship can be expressed via the Hurst exponent H , and can be derived by computing the RMSD over different length scales

$$v(\Delta x) = v(\Delta x_0) \left(\frac{\Delta x}{\Delta x_0} \right)^H, \quad (11)$$

where Δx_0 is a reference horizontal lag [Shepard *et al.*, 2001]. H can be derived from devioqram plots where the rms deviations are plotted as a function of the horizontal lags on a double-logarithmic plot [e.g. Shepard *et al.*, 2001]. Here, we derive H from linear fits in the devioqram for horizontal lags between 50-800 m. Shorter and longer lags outside this range were excluded to ensure linearity. H ranges between 0-1, where for $H = 1$, the terrain is ‘self-similar’ with the horizontal and vertical scales of the roughness increasing at the same rate, and for $H = 0$, the terrain is ‘stationary’ where the vertical roughness parameters are independent of the horizontal length scale. The relationship in Eq. (11) allows us to estimate basal roughness on a wavelength scale ($\Delta x = 5$ m), which is much smaller than the along-track sampling rate of the radar data. For areas with $H < 0.5$, where vertical roughness is essentially independent of the horizontal lag, no wavelength scale RMSD values were extrapolated, leading to gaps in the resulting roughness map.

The degree of radar wave scattering has been related to the Hurst exponent, with specular bed reflections being associated with generally lower Hurst exponents [Jordan *et al.*, 2017]. Thus,

the Hurst exponents derived here may be used as a proxy for specularity, and thus for the presence of subglacial water.

4.4 Results

4.4.1 Bed morphology

The high spatial resolution of this dataset allows us to identify great detail in the subglacial bedrock terrain, in particular to map the morphology of the bedrock troughs T1 and T2, each of which has been hypothesized to contain a subglacial lake [Rutishauser *et al.*, 2018] (Figure 4-5a). As previous studies already noted, DIC is underlain by a rugged mountainous terrain that reaches elevations above 1700 m asl. near the center of the ice cap, and is incised by numerous subglacial bedrock troughs [Dowdeswell *et al.*, 2004; Rutishauser *et al.*, 2018]. The new bed DEM reveals that bedrock trough T2 is part of a deeply (~150-300 m) incised canyon which likely extends towards the western margin of the ice cap. This is one of the most extensive canyons beneath DIC, and in contrast to most others, under the current ice dynamics, is not connected to a marine-terminating outlet glacier. Studying the formation of this canyon and determining whether it was formed by glacier flow, subaerial rivers or shaped tectonically is beyond the scope of this study, but could potentially reveal information about past ice cap configurations and ice dynamics. In comparison, T1 is less incised (~100-200 m) into the bedrock and widens towards a plateau area in the north-west, at the head of a canyon that leads into the Sverdrup Glacier.

Average ice thicknesses are about 430 m, but exceed 800 m in some bedrock troughs (Figure 4-5b). Ice thicknesses over T1 are about 555 m, whereas along the canyon extending from T2 they exceed 700 m in a large portion of the canyon.

The western part of DIC has a generally flatter bed topography, and is characterized by smoother beds than the eastern part, which is defined by a more mountainous terrain and rougher beds (Figure 4-6a). The general transition from smoother beds in the west to more pronounced and rougher bed topography in the east may result from a change in basal lithology, and could be used to further refine the bedrock geology model generated by Rutishauser *et al.* (2018).

The spatial pattern in the Hurst exponent largely follows the bedrock morphology with lower Hurst values where the bed is flatter and smoother (Figure 4-6c and d). Furthermore, particularly low Hurst anomalies and low roughness occur near the previously identified subglacial lakes along troughs T1 and T2 (Figure 4-6b and d). The low Hurst exponents over

T1 correlate with previous observations of high specularity in the region [Rutishauser *et al.*, 2018], although the area of low Hurst exponents extends further to the west. This, in combination with observations of increased radar specularity over low Hurst areas beneath the Greenland Ice Sheet [Jordan *et al.*, 2017], may indicate that both T1 and T2 are characterized by specular interfaces.

4.4.2 Basal reflectivity

After all corrections are applied, variations in basal reflectivity result from a combination of changes in the dielectric contrast at the glacier bed and the roughness of the ice-bed interface. A reflectivity map shows a west-east gradient in basal reflectivities, with generally higher reflectivity in the north-western and central part of DIC (Figure 4-7). This gradient can also be observed in the median reflectivities for the individual catchment areas, where catchment areas in the west are characterized by reflectivities about 0.4-8.1 dB higher than those found in catchment areas in the eastern part of the ice cap. Following previous studies and interpreting the basal reflectivities as indicators for transitions between wet and dry bedrock conditions [Hubbard *et al.*, 2004; Peters *et al.*, 2005; Christianson *et al.*, 2012; Chu *et al.*, 2018], the observed reflectivity pattern suggests that the central and western part of DIC consist of widespread areas of wet beds, whereas the eastern part is characterized by predominantly dry beds. A map of reflectivity anomalies above the 12 dB threshold defined here as indicative of wet beds, summarizes the above observations and reveals that a high concentration of values of $R \geq 12$ dB occurs in the catchment area drained by Sverdrup Glacier (Figure 4-8a and Figure 4-9a).

High reflectivity anomalies are also observed within bedrock troughs T1 and T2, and over the areas of the two subglacial lakes hypothesized by Rutishauser *et al.* (2018). This is in agreement with the previous observation of high reflectivity anomalies [Rutishauser *et al.*, 2018] and supports the presence of subglacial water in these bedrock troughs. However, the reflectivity anomalies over T1 and T2 are not restricted to the previously outlined lake boundaries, indicating that the subglacial lakes may be larger in extent than was suggested by the previous dataset. Furthermore, high reflectivity anomalies are also observed outside T1 and T2, and are generally not restricted to bedrock troughs, which suggests that subglacial water may occur more extensively beneath DIC than was previously thought.

A comparison between the reflectivity pattern and the projected outcrop boundaries of the salt-bearing rock unit beneath DIC [Rutishauser *et al.*, 2018] shows that most high reflectivity anomalies are located in areas where the ice is projected to be underlain by salt-bearing rocks,

or at elevations below the boundary of this geological unit (especially in the western half of the ice cap) (Figure 4-7). While T1 is located within the projected salt-bearing unit, T2 is located just below the projected outcrop boundary and may receive brine input from areas above that are underlain by salt-bearing rocks. However, since the actual geological boundaries beneath the ice are unknown and because there are uncertainties in the geology model, *Rutishauser et al.* (2018) recognized that T2 may also be underlain by salt-bearing rocks.

The general pattern of basal reflectivities appears to correlate with the mapped wavelength-scale basal roughness (correlation coefficient $r = 0.4$, $n > 1.5 \times 10^5$ and $p = 0$ for a 95% confidence interval), where the reflectivities show an inverse relationship to the RMSD roughness (Figure 4-8). However, only 7.1% of all areas with RMSD roughness ≤ 0.51 m, which is the mean RMSD of all locations with $R \geq 12$ dB, show reflectivity anomalies of 12 dB or higher. The mean basal reflectivity for these low-roughness areas is 4 dB (Figure 4-8d). Despite the general correlation between the reflectivity and basal roughness, the absence of high reflectivity anomalies in 92.9% of the low roughness areas suggests that low basal roughness is not the exclusive cause of high reflectivity anomalies. Instead, it is likely a combination of low basal roughness and high dielectric permittivity at the glacier bed (i.e. from wet beds) that generates the high reflectivity anomalies observed beneath DIC.

The spatial distribution of basal reflectivities has a different pattern than is observed for radar scattering at the near-surface firn [*Rutishauser et al.*, 2016]. This indicates that firn losses are small, and implies that neglecting potential energy losses from the near-surface firn is justified for the purposes of this study.

4.4.3 Hydraulic head and subglacial water routes

High reflectivities indicating the presence of subglacial water are observed over both hypothesized subglacial lakes, as well as over extensive areas beneath the central and western parts of DIC. In order to examine the previous hypothesis of the existence of the two subglacial lakes and to determine whether the high reflectivities in the surrounding areas result from subglacial lakes or wet beds, we evaluate the criterion of hydraulic flatness [e.g. *Carter et al.*, 2007; *Langley et al.*, 2011]. High reflectivity anomalies that coincide with regions with flat hydraulic heads are typical signatures for a subglacial water body, where ice is afloat and the water is in hydrostatic equilibrium with the ice overburden pressure [e.g. *Carter et al.*, 2007].

In agreement with previous observations [Rutishauser *et al.*, 2018], the dataset used for this study reveals an area of relatively flat hydraulic head over bedrock trough T2, with slopes below our defined threshold for hydraulic flatness (Figure 4-9). The spatial correspondence between the hydraulic flatness, the high basal reflectivities, and the low basal roughness and Hurst exponent strongly support the previous inference of the existence of a subglacial lake in this bedrock trough. However, like the high basal reflectivity anomalies, the hydraulically flat area extends beyond the previously defined lake boundaries. This suggests that this subglacial lake may be larger than was previously suggested.

In contrast, and confirming previous observations [Rutishauser *et al.*, 2018], no area of flat hydraulic head is observed over the hypothesized subglacial lake in T1. Rutishauser *et al.* (2018) argued that the non-flat hydraulic head may result from flexural stresses preventing a hydrostatic equilibrium (i.e. the ice is not fully afloat), from uncertainties in the bedrock topography due to the relatively sparse data coverage, or from the lake outlined consisting of a thin film of water or a layer of water-saturated sediments rather than a deep water body. With the high spatial coverage of the new dataset, we can dismiss the argument of uncertainties in the bedrock topography. Furthermore, the relatively flat hydraulic head over T2 indicates that no, or only small flexural stresses occur over T2, thus reducing the likelihood of strong flexural stresses occurring over the less incised trough T1. Our results therefore strengthen the argument for a wet bed in- and around T1 rather than for the existence of a deep water body.

Overall, T2 is the only location where a hydraulically flat area coincides with a high concentration of high reflectivity anomalies (Figure 4-10). The absence of flat hydraulic heads across most other areas where the reflectivity suggests the presence of subglacial water indicates that the bed is characterized by water concentrated in small ponds or channels, as thin films or in saturated sediments rather than consisting of deep water bodies. In return, areas with flat hydraulic heads outside T2 might be caused by coincident combinations of bed and ice surface topographies such as opposing bed and surface slopes, rather than by hydrostatic equilibrium with a subglacial lake.

With respect to water flow paths, high reflectivities are mostly concentrated at the heads of predicted water flow routes and in topographically flat areas in-between them, but are not observed further downstream along the flow paths (Figure 4-11). The canyon connecting T2 with the western margin is the only exception to this observation, as higher basal reflectivity (but still below 12 dB) is also observed along the flow path following this canyon. Possible

glaciological processes and potential limits in radar detection that may account for this pattern are discussed in Section 4.6.2.

4.5 Definition of new shorelines for subglacial lake in T2

Results from the SRH1 survey strongly support the hypothesis for a subglacial lake in bedrock trough T2, however, the new dataset also indicates that the boundary drawn by *Rutishauser et al.* (2018) is likely too simplistic and does not capture the full extent of the subglacial lake. Here, we use a combination of hydraulic flatness and elevated basal reflectivity as criteria to derive new shorelines for this subglacial lake [e.g. *Carter et al.*, 2007].

In a first step, new lake shores are defined using an algorithm applied to each grid cell of the hydraulic head surface over bedrock trough T2 (Figure 4-12). A grid cell is defined as part of a subglacial water body if the cell is hydraulically flat and has a median $R \geq 7.3$ dB, corresponding to a one-standard deviation anomaly from the mean of all observed reflectivities beneath DIC (Table 4-2). Additionally, neighboring grid cells that are not hydraulically flat, but pass the reflectivity threshold of 7.3 dB are included in the inferred lake. This allows the inclusion of areas with shallow water near the lake shore where hydrostatic equilibrium may not be fully developed. In contrast, stand-alone grid cells where the above thresholds apply are neglected. Finally, the algorithm-defined shore lines were refined manually based on the basal reflectivities along the radar transects. This allows for a more precise identification of the shorelines compared to the algorithm, which averages reflectivity values over the grid cells.

The new shorelines defined in this study result in the identification of three water bodies in the vicinity of the southernmost of the previously identified subglacial lakes. These are hereafter referred to as T2A, T2B and T2C (Figure 4-12). Table 4-2 summarizes the basal characteristics observed within the identified water bodies, and compares them to the basal properties of the entire ice cap. The reflectivities over T2A, T2B and T2C are on average 9.7 dB, 8.4 dB and 8.5 dB above the median of all measured reflectivities, respectively. For comparison, the median reflectivity anomaly resulting from this dataset for the area that lies within the previously defined subglacial lake area is 8 dB. Although the average reflectivity anomalies in T2A-C are below the theoretical threshold of 12 dB for a wet to dry bed transition [*Peters et al.*, 2005], they are significantly higher than the anomalies in the areas around them (Figure 4-13). Similar observations of relatively low (6 dB) reflectivity anomalies were used to map the boundaries of subglacial lake Whillans, Antarctica [*Christianson et al.*, 2012]. Additionally, the reflectivity distributions over T2A-C have relatively low standard deviations (ranging between 3.6-3.9 dB). This is much lower than the 7.3 dB standard deviation of all measured reflectivities and

indicates that more uniform bed conditions are sampled. Thus, the high reflectivity anomalies and low standard deviations are consistent with characteristics that are expected over a relatively uniform ice-water interface across a subglacial water body, supporting the defined shorelines. The evidence for an ice-water interface across these areas is further supported by the low Hurst exponent, particularly over T2A, and the low RMSD roughness that indicates a smooth and specular interface (Figure 4-6). Some remaining variation in basal reflectivity may occur due to small scale roughnesses in the ice-water interface and near the lake shores where the water layer is locally thin. Similarly, small slopes in the hydraulic head (below the measurement uncertainties) may remain due to bridging stresses in the overlying ice that potentially prevent a fully developed hydraulic equilibrium. The areas for the newly defined water bodies T2A, T2B and T2C are 10.4 km², 4.6 km² and 8.1 km², respectively, with a total area of 23.2 km² which is more than double the area of the previously defined subglacial lake in T2.

Although the individual water bodies partially share the same hydraulically flat area, a drop in basal reflectivity beyond the defined shorelines suggests that they are separated by areas with dry(er) beds. However, it is possible that the water bodies are connected via channels that would remain undetected in the radar data if their sizes are much smaller than the radar footprint. Thus, we cannot conclusively say whether T2 consists of a single subglacial lake, or of three individual water bodies as outlined in Figure 4-12. For simplification, we hereafter refer to T2A-C as ‘one subglacial lake’. Additionally, a few reflectivity anomalies are also observed in the narrowing extensions of the bedrock trough around T2A and T2C, as well as in the connected canyon to the west. Here, we did not include these areas as part of the defined water bodies due to the relatively sparse occurrence of the anomalies. Nevertheless, we cannot exclude the possibility that water pooled in these areas may be connected to the water bodies mapped.

Figure 4-13 shows the bed topography, hydraulic head and basal reflectivity along selected radar profiles over T2. These profiles show that the reflection surface over the subglacial lake is exceptionally flat, which further supports the evidence for a water filled bedrock trough. In contrast, the reflecting surface in the canyon further upstream and downstream of where we outline the water bodies is less flat, and is generally characterized by bed slopes towards the canyon center (Figure 4-14). While we acknowledge the fact that the unfocused radar data used here do not provide a true representation of the bedrock topography, the flat surfaces at the trough bottom are unlikely to be affected by focusing of the data.

The trough morphology and associated lake water depths are likely to reflect the influences of geological and hydrological processes such as tectonic faulting, glacial or hydrological erosion, and spatial variations in bedrock lithology and its resistance to erosion, and/or sedimentary infill processes. If T2 is a tectonically controlled feature, its subglacial lake likely has a deeper water column than what would be expected if the trough was shaped by erosional processes controlled by bedrock lithology [e.g. *Bell et al.*, 2006; *Jamieson et al.*, 2016]. While water depths in T2 are currently unknown, inspection of the trough morphology could potentially be used to derive first-order water depth estimates through a slope projection of the valley walls.

Results from the water routing model suggest that if water flows out of T2A, it would do so at two locations (Figure 4-15). In the east, water may discharge through a relatively narrow trough towards the south, while in the west water routes follow the subglacial trough and potentially connect T2A with T2B and T2C. From the perturbation test of the water routing model, water would most likely flow out of T2C towards the south, with no clear hydrological connectivity to the western extension of the canyon. Only when the hydraulic head is perturbed with errors of 2-3 times the uncertainties in the hydraulic head, would water routes connect T2B and T2C with the canyon in the west (Figure S 4-2). Following the modeled water routes, outflows from the water bodies would eventually drain into North Croker Bay, a marine-terminating outlet glacier on the south side of DIC.

4.6 Discussion

4.6.1 Likelihood of the existence of the hypothesized subglacial lakes

The combined observations of a hydraulically flat areas with relatively high- and constant basal reflectivities (with low standard deviation) over bedrock trough T2 strongly support the existence of the previously hypothesized subglacial lake. Although specular data are not yet available, the low Hurst exponent and low basal roughness suggest the presence of a specular interface, which would support the interpretation of a subglacial lake. Finally, the particularly flat bottom of the bedrock trough in the subglacial lake area conforms with the interpretation of a water filled trough.

An alternative interpretation for the observed reflectivity anomalies over T2, and the flat trough bottom could be that the trough is filled with a layer of smooth (and potentially water-saturated) sediments causing highly specular radar reflections. However, unless this part of the canyon consists of an over-deepening, this explanation raises the question why such sediments would only be found in this part of the canyon. Furthermore, this interpretation fails to explain the

hydraulic flatness over the area, which is a result of the combined relative flatness of both the bedrock and ice surfaces. The ice surface over a subglacial lake is generally flat due to the ice being afloat on the subglacial liquid. Nevertheless in the absence of a subglacial lake, flat ice surfaces may also occur as a result of their general relationship to the bedrock topography, where the surface expression is a function of the amplitude and wavelengths of bedrock perturbations, ice dynamics and ice rheology [e.g. *Budd, 1970; Raymond and Gudmundsson, 2005*]. Overall, the observed characteristics of the ice over T2 are in good agreement with the physical principles that generally apply over subglacial lakes [e.g. *Carter et al., 2007*]. Without being able to fully exclude the above possibilities, we argue that the existence of a subglacial lake is more likely than the number of concurrent exemptions from these general principles that would have to occur to explain the observed subglacial lake signatures in the absence of a subglacial lake.

As previously observed, this subglacial lake is situated just below the projected geological contact with potentially salt-bearing rocks (Figure 4-7) [*Rutishauser et al., 2018*]. It is therefore possible that brines which may have formed either through direct contact between the ice and the saline rocks, or subaerially during a past interglacial period [*Rutishauser et al., 2018*] are/were routed into this bedrock trough, providing the water contained in the subglacial lake. We therefore argue that the location of the lake relative to the projected geology supports the existence of a hypersaline subglacial lake.

In contrast to T2, the absence of a flat hydraulic head gradient over T1 strongly suggests that the high reflectivity anomalies observed in this area are associated with a wet bed rather than with a deep subglacial lake. However, *Rutishauser et al. (2018)* observed uniquely high specular values indicating a smooth ice-bed transition, and used this as a criterion for the existence of the subglacial lake in T1. Furthermore, they noted the possibility that the ice-bottom interface over the subglacial lake may be further smoothed by active subglacial melting. The low Hurst exponents observed in this study could support the presence of a highly specular interface over T1 [*Jordan et al., 2017*]. Here, the general use of specular surfaces as diagnostic tool to identify subglacial lakes is contrary to the criterion of flat hydraulic heads. *Jordan et al., (2017)* also obtained such contradictory results where more specular reflections were found over frozen beds beneath the Greenland Ice Sheet than over thawed areas. Based on the sloping hydraulic gradients over T1 and the observation of high reflectivity in hydraulically non-flat areas below extensive parts of DIC, we conclude that the subglacial water signatures over T1 more likely represent an area of wet bed than a deep water body.

4.6.2 Basal hydrological conditions outside the subglacial lake

The pattern of basal reflectivity reveals substantial regions with high reflectivity anomalies ($R \geq 12$ dB) beneath the central and western part of DIC. In contrast to the subglacial lake identified in T2, these areas are not hydraulically flat and are thus not classified as subglacial lakes. Instead, we suggest that these reflectivity anomalies result from a subglacial brine-network in which water is concentrated in small ponds, channels, thin films of water, water-saturated sediments, or some sort of brine-slush. This brine-network is largely located in the area in which salt-bearing rocks are projected to outcrop beneath the ice, or at elevations below this geological unit (Figure 4-7) [Rutishauser *et al.*, 2018]. Although the exact lithology is unknown, we hypothesize that the brine-network is associated with the lithological boundaries, such that brine is generated in areas where ice is in direct contact with salt-bearing rocks, and may spread downstream from there. Another possibility is that the brine-network represents remnant brine that was generated during an interglacial period through interactions of water with underlying salt-bearing rocks, and potentially cryoconcentration that increases the salinity upon ice coverage. The exact processes of salt/brine-ice interactions and the effects on basal melting, subglacial erosion and subglacial hydrological and geochemical processes remain unknown.

The hypothesis that the brine-network is associated with the outcropping of a particular lithology could be supported by observations of the bed morphology and the pattern of basal roughness, which both indicate a change in lithology from the western to the eastern part of DIC. One could argue that the observed reflectivity pattern is a result of changes in basal roughness and that the reflectivity changes are misinterpreted as wet and dry beds. However, while acknowledging the general inverse correlation between basal reflectivity and roughness which likely explains some reflectivity variations, no consistent pattern is observed throughout all sampled areas (see Section 4.4.2 and Figure 4-8). Although we cannot differentiate between the reflectivity anomalies resulting from subglacial water and smooth beds with certainty, the interpretation that there are areas of both wet and dry beds is supported by the evidence for the existence of subglacial water in T2 together with the evidence for salt-bearing rocks outcropping beneath the ice [Rutishauser *et al.*, 2018], and by the observation that not all smooth beds result in high basal reflectivity while some areas where the bedrock surface is rough do. However, further research, including the derivation of the specular content [Schroeder *et al.*, 2013; Young *et al.*, 2016] is required to fully evaluate this interpretation.

High reflectivity signatures of the hypothesized brine-network are generally observed at the head of water routes as well as in relatively flat areas in between the water flow paths.

Interestingly, no radar signatures that would indicate the presence of subglacial water are observed further downstream along the predicted flow routes. Possible explanations for this pattern include that the bed along the predicted flow paths is dry either due to either a lack of downstream transport of brine or basal freeze-on processes [e.g. *Wolovick et al.*, 2013], or that the radar instrument fails to detect subglacial water signatures in these areas. The water routes for the subglacial brine are strongly topographically controlled and thus generally pass through relatively narrow canyons towards the ice cap margins. It is therefore possible that due to the confinement of water flow within narrow canyons, the subglacial brine-network transitions from a patchy and distributed system to a channelized subglacial water system, which has different morphologies and radar signatures [e.g. *Schroeder et al.*, 2013]. Depending on the size and orientation of subglacial channels with respect to the radar footprint and antenna orientation, subglacial water concentrated in channels may remain undetected in the radar measurements.

The canyon extending from T2 towards the western margin is the only exception to this pattern as somewhat higher reflectivities can be observed along this flow path further downstream. This canyon is much wider than other identified canyons beneath DIC, and it is therefore plausible that the subglacial water system remains as a distributed system, which shows up as more specular water interfaces within the radar footprint, leading to the observed higher reflectivities. Further characterization of the subglacial water system beneath DIC and possible transitions from a distributed brine-network to a channelized morphology could be investigated via the specular content [*Schroeder et al.*, 2013], which can be derived from this dataset upon further processing. If brine is transported to the ice cap margins, it might be possible to detect saline outflows from this subglacial brine-network at the margins.

4.7 Conclusions

Based on the results from this study, we were able to evaluate the likelihood for the existence of the previously hypothesized subglacial lakes beneath DIC [*Rutishauser et al.*, 2018] and to characterize the hydrological conditions in the area around them. Our results strongly support the evidence for a subglacial lake in bedrock trough T2, where the new dataset indicates the existence of three distinct, but possibly connected, water bodies with a total area of 23.2 km². In contrary, we conclude that the observed subglacial water signatures over bedrock trough T1 arise from wet beds rather than from a deep water-body. This possibility has already been acknowledged by *Rutishauser et al.* (2018), but could not be resolved with certainty due to the

relatively sparse data coverage available for that study, which highlights the importance of collecting dense datasets over relatively small subglacial features such as the lake beneath DIC.

This study also reveals extensive areas of wet beds near the central and western regions of DIC, which we interpret as part of a brine-network. We speculate that the characteristics of this brine-network are related to, and potentially controlled by the bedrock topography and lithology, where sub-ice outcrops of the salt-bearing evaporite unit proposed by *Rutishauser et al. (2018)* likely play a crucial role in the formation of the hypersaline water and its geochemistry. Although the processes of formation and detailed configuration of the hypothesized brine-network remain unknown, this study indicates that the subglacial hydrological conditions beneath DIC are more complex than previously suggested.

Our results, in particular the confirmation of the existence of one of the subglacial lakes, and the determination of its full extent and potential connectivity to a surrounding brine-network will help inform the planning of future research into this lake, including in-situ access and sampling of the lake water to explore its habitability for microbial life. Additionally, further investigations into the unique subglacial hydrological system beneath DIC and its relationship to bed lithology and topography could serve as a guide for interpretations of other novel subglacial water systems that may exist in other parts of the Canadian Arctic where glaciers and ice caps overlie similar evaporitic geological units [*Harrison et al., 2016; Rutishauser et al., 2018*].

While our analysis is based on unfocused radar data, more detailed characteristics of this complex subglacial hydrological system beneath DIC could be derived upon further processing of the dataset, including derivation of the radar scattering properties of the bed (specularity content) and first-order water depths of the subglacial lake via a valley-wall slope projection.

4.8 Acknowledgments

The aero-geophysical survey and data analyses were funded by The W. Garfield Weston Foundation. We thank The W. Garfield Weston Foundation for championing northern research, and for providing the opportunity for Canadian researchers to engage in this exciting scientific opportunity in the Canadian Arctic. We thank PCSP and Kenn Borek Air Ltd. for logistical support, the field survey team for help with data collection, and NRI and the peoples of Grise Fjord and Resolute Bay for permission to conduct airborne surveys over Devon Ice Cap.

Tables

Table 4-1: Parameters and dielectric properties used in the conductivity model to estimate attenuation rates across DIC.

Symbol	Description	Units	Value
T_r	Reference temperature	K	252 ^a
T	Ice temperature	K	Modeled using a steady-state 1D advection-diffusion model
σ_{pure}	Conductivity of pure ice	μSm^{-1}	9.2±0.2 ^a
μ_{H^+}	Molar conductivity of H^+	$\text{S m}^{-1} \text{M}^{-1}$	3.2±0.5 ^a
μ_{Cl^-}	Molar conductivity of Cl^-	$\text{S m}^{-1} \text{M}^{-1}$	0.43±0.07 ^a
$\mu_{NH_4^+}$	Molar conductivity of NH_4^+	$\text{S m}^{-1} \text{M}^{-1}$	0.8 ^a
$[H^+]$	Molar concentration of H^+	μM	1.82 ^b
$[Cl^-]$	Molar concentration of Cl^-	μM	1.00 ^b
$[NH_4^+]$	Molar concentration of NH_4^+	μM	1.20 ^b
E_{pure}	Activation energy of pure ice	eV	0.51±0.01 ^a
E_{H^+}	Activation energy of H^+	eV	0.20±0.04 ^a
E_{Cl^-}	Activation energy of Cl^-	eV	0.19±0.02 ^a
$E_{NH_4^+}$	Activation energy of NH_4^+	eV	0.23 ^a

^a Values taken from the M07 model for the Greenland Ice Sheet as described in *MacGregor et al. (2015)* and applied by *Jordan et al. (2016)*.^b Average concentration measured along a firn core retrieved from DIC [*Criscitiello et al.*, in prep.].

Table 4-2: Median (mdn) basal reflectivity along with their standard deviation (std) and hydraulic heads from data within the original shorelines outlined by Rutishauser et al. (2018), and the newly defined shorelines for T2A-C from this study. ΔR is the median reflectivity anomaly over the subglacial lakes relative to the median of data.

	All Data	T1 ^a	T2 ^a	T2A	T2B	T2C	T2A-C
mdn R [dB]	-21.5	-11.1	-13.5	-11.8	-13.1	-13.0	-12.5
std [dB]	7.3	6.0	5.3	3.9	3.6	3.6	3.8
ΔR [dB]	-	10.4	8.0	9.7	8.4	8.5	9.0
Hydraulic head (range) [m asl]	416-2158 (1742)	1604-1710 (106)	1575-1633 (75)	1599-1650 (51)	1559-1603 (44)	1506-1546 (40)	1506-1650 (145)
Area [km ²]	~6700	7.4 ^b	8.4 ^b	10.4	4.6	8.1	23.2

^a Previously defined subglacial lake shorelines from Rutishauser et al. (2018). ^b Note that the original area calculations by Rutishauser et al. (2018) were erroneous.

Figures

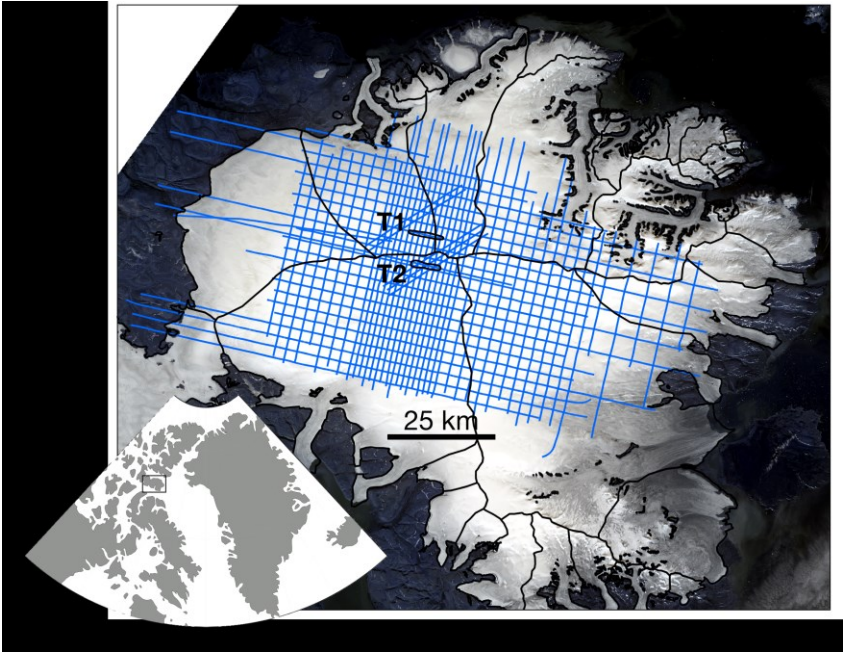


Figure 4-1: Location of Devon Ice Cap in the Canadian Arctic and Landsat image of Devon Ice Cap overlain with the survey grid and the locations of of the previously identified subglacial lakes within the bedrock troughs T1 and T2.

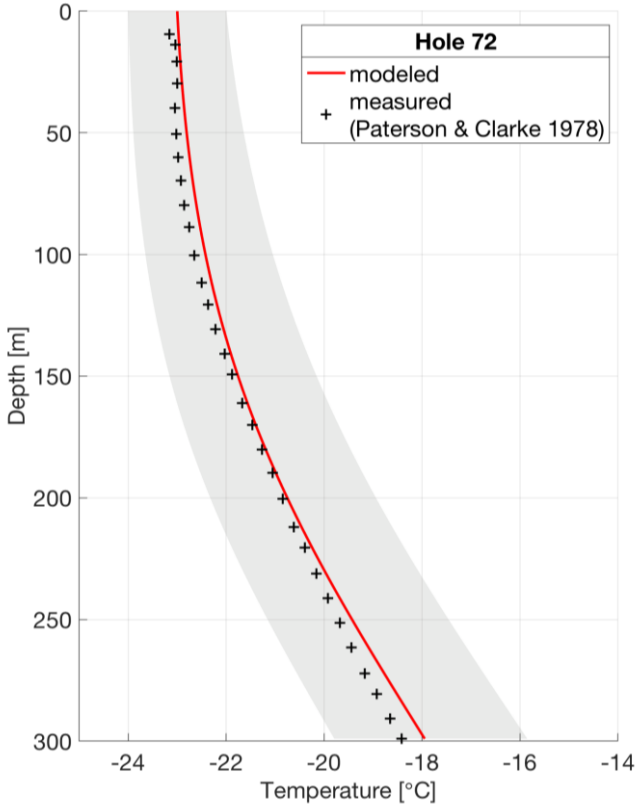


Figure 4-2: Comparison of the 1D steady-state advection-diffusion modeled ice temperatures (red) to measured ice temperatures near the summit of DIC (black) [Paterson and Clarke, 1978]. The grey shaded area indicates the uncertainties by propagating the uncertainties of the model input parameters.

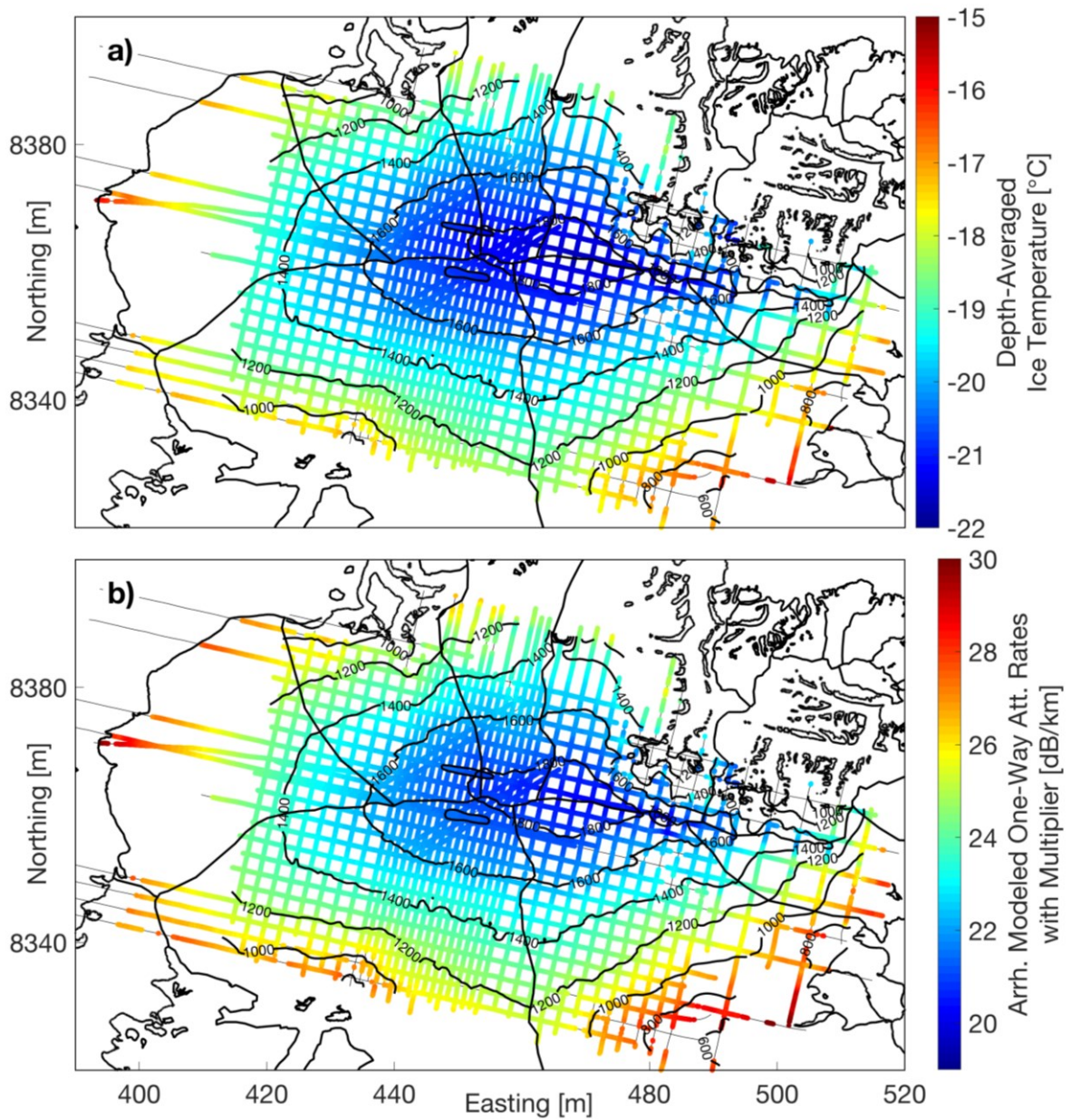


Figure 4-3: a) Map of modeled depth-averaged ice temperatures using a steady-state 1D advection-diffusion model across DIC along with the location of the previously hypothesized subglacial lakes. Black contour lines represent the ice surface elevation (200 m interval) and the ice divides. b) Adjusted depth-averaged Arrhenius modeled attenuation rates which are used for the attenuation correction in this study.

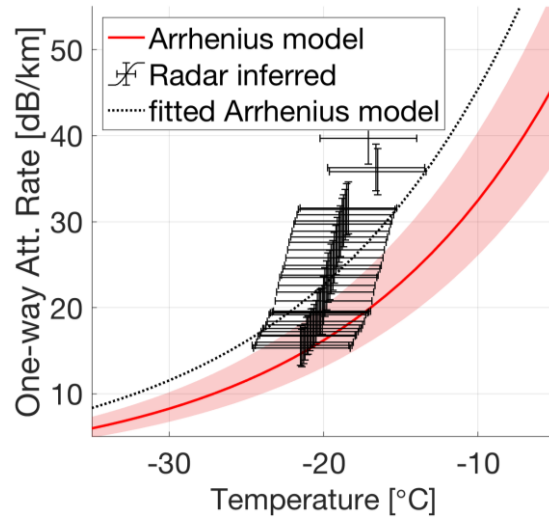


Figure 4-4: Radar inferred (linear fit between ice thickness and bed power) and Arrhenius modeled attenuation rates. The uncertainty in the Arrhenius modeled attenuation rates is computed using the average ice temperature uncertainty of 3.14 °C, which also represents the temperature error bars in the radar-inferred attenuation rates. Radar-inferred attenuation rate uncertainties are derived as N_h . The dotted black line represents the Arrhenius modeled attenuation rates with a multiplier of 1.4, which is used in this study.

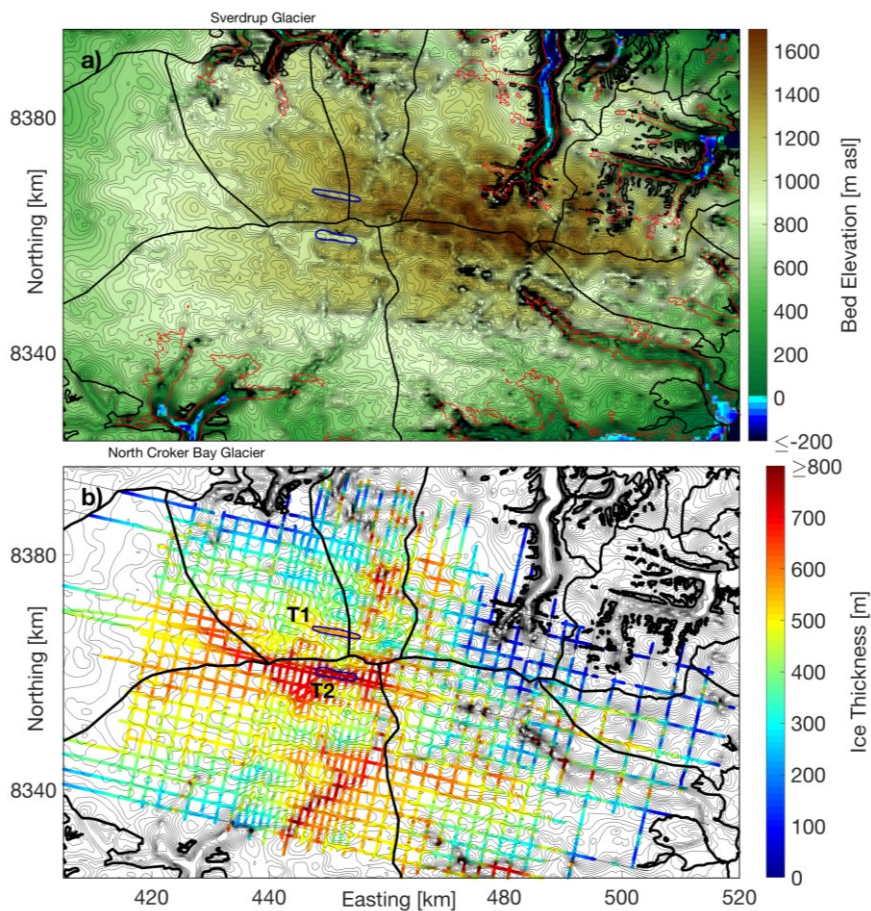


Figure 4-5: a) Bedrock topography (contour lines every 25 m) overlain with the location of the outlines of the hypothesized subglacial lakes from Rutishauser et al. (2018) in blue. Red lines depict the 20 m/yr ice flow contour line derived from Van Wychen et al., (2014). b) Ice thickness along survey lines, overlain with the bedrock contours (every 50 m).

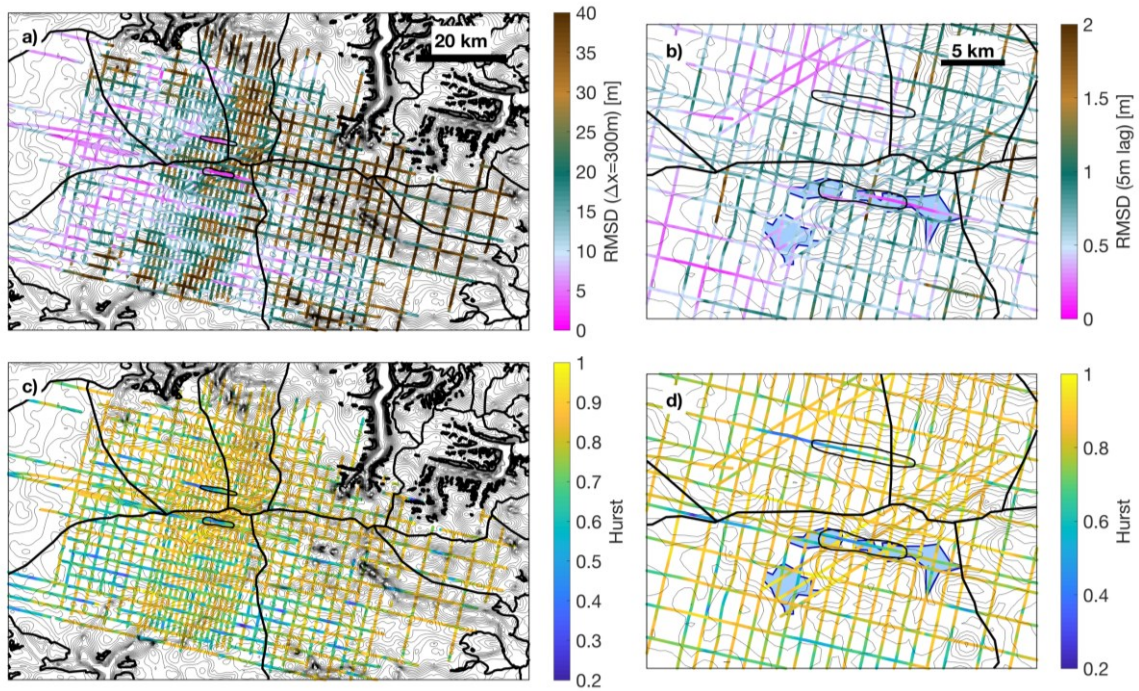


Figure 4-6: a) Basal roughness on a radar footprint scale ($\Delta x=300\text{m}$) over DIC, and b) basal roughness on the wavelength scale ($\Delta x=5\text{m}$) in the region of the subglacial lakes. c) Hurst exponent over DIC and d) Hurst exponent over the area of the subglacial lakes. Previously hypothesized (black) [Rutishauser et al., 2018] and newly defined (blue shaded) subglacial lake boundaries are outlined. Bed contours are marked with thin black lines with a 50 m interval, whereas thick black lines indicate the location of the ice divides.

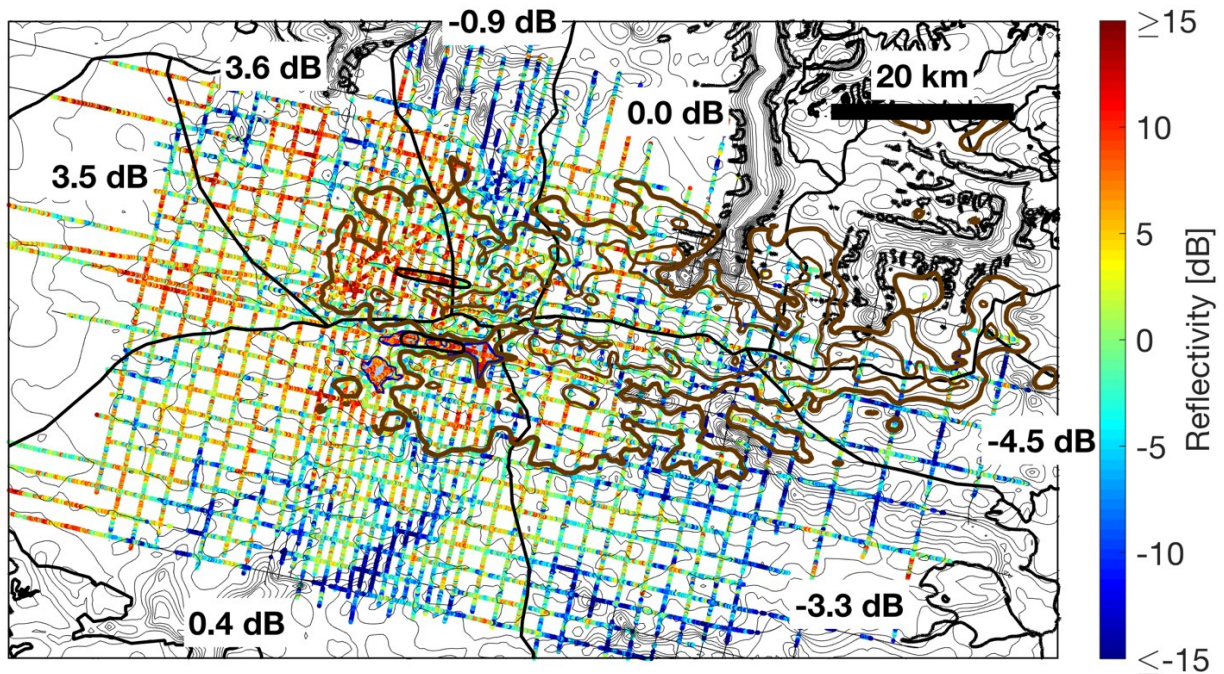


Figure 4-7: Basal Reflectivity map along with the median reflectivity anomaly for the individual catchment areas (numbers). Brown lines indicate the bottom (thick lines) and top (thin lines) of the projected salt-bearing rock outcrops underneath the ice [Rutishauser et al., 2018]. Thin black lines are the bed topography contour lines (every 50 m), and thick black lines represent the locations of the ice divides.

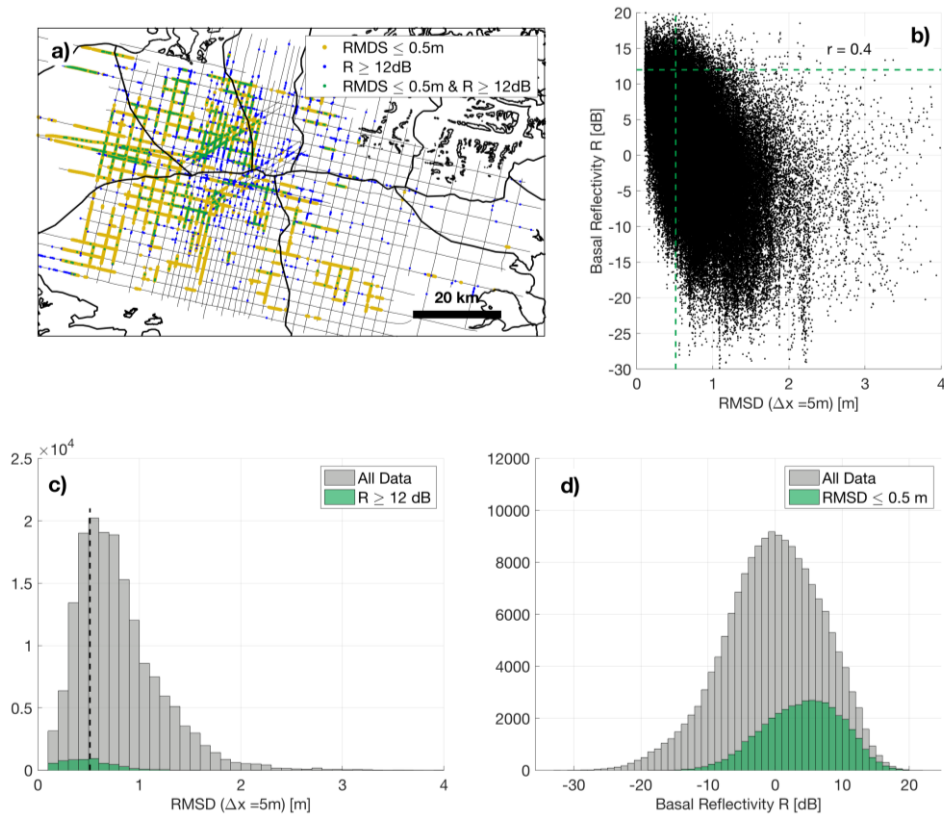


Figure 4-8: a) Map indicating low roughness areas (yellow) and high reflectivity anomalies (blue), along with locations where they overlap (green). b) Correlation between basal reflectivity (R) and RMSD. c) Distribution of all RMSD values along with the distribution of RMSD over high reflectivity areas, which has a mean of 0.51 m (used as threshold to define 'low roughness' areas). d) Distribution of all basal reflectivities along with the reflectivities over low roughness areas, which has a mean of 4 dB.

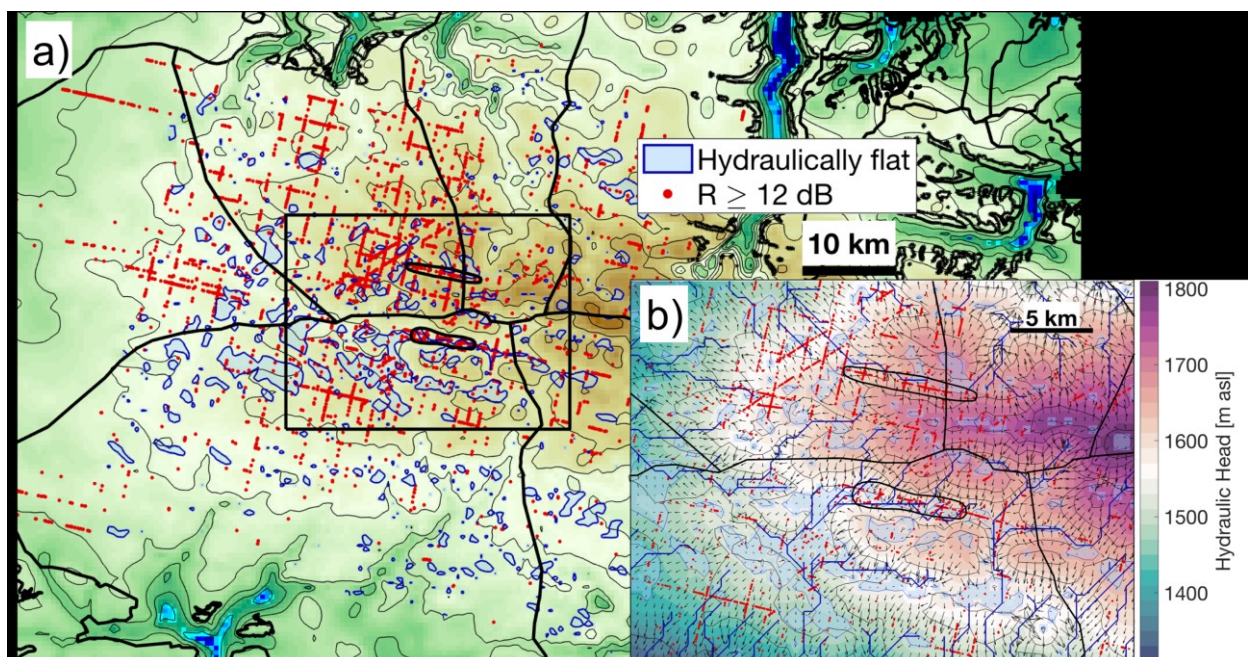


Figure 4-9 a) Bed DEM overlain with hydraulically flat areas (blue) and reflectivity anomalies $R \geq 12$ dB (red). b) Hydraulic head over the area of the hypothesized subglacial lakes overlain with hydraulically flat areas, reflectivity anomalies and potential water routes.

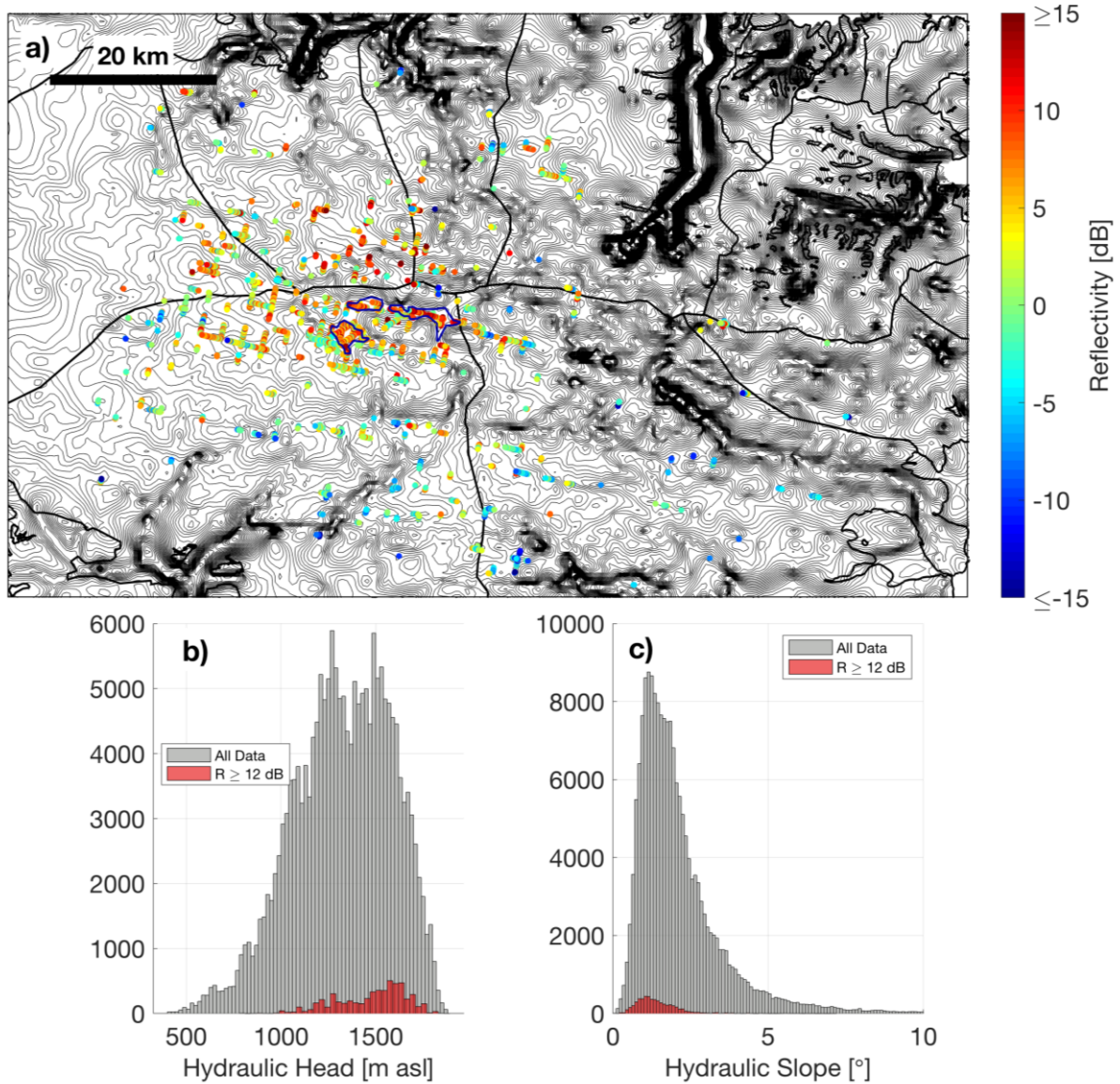


Figure 4-10: a) Bedrock contour lines (25 m interval) overlain with basal reflectivity values over hydraulically flat areas. The newly defined shorelines of the subglacial water bodies in T2 are outlined in blue. b) and c) distribution of all (gray) hydraulic heads and slopes observed over DIC, along with the hydraulic heads and slopes that occur in areas where $R \geq 12$ dB (red).

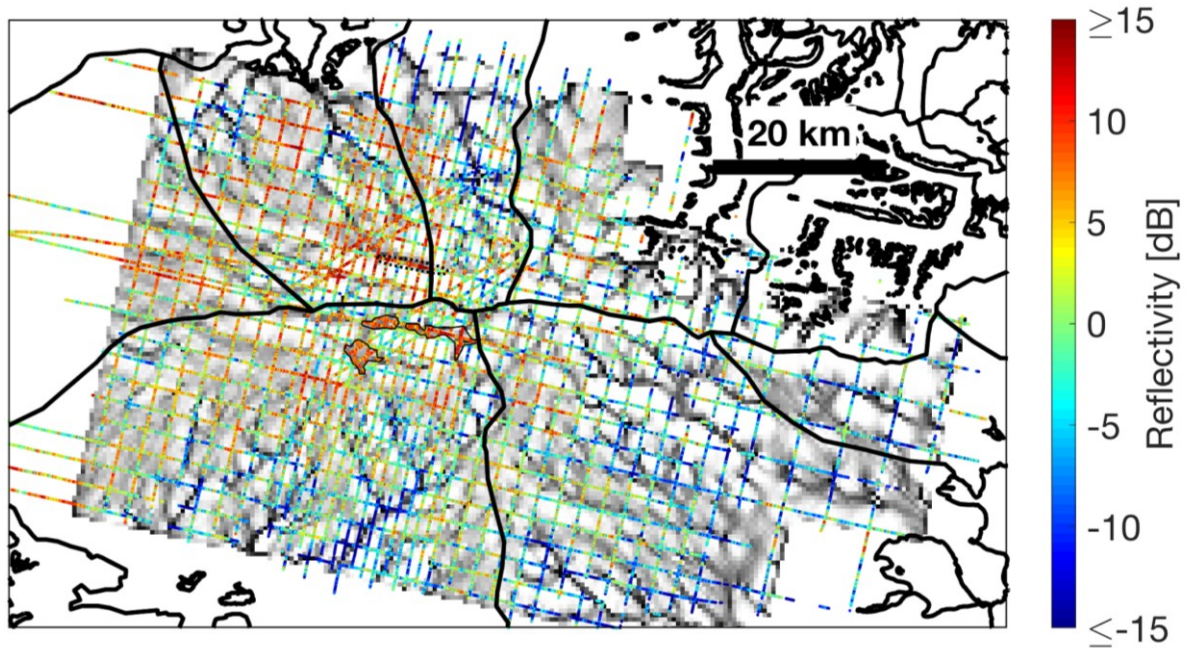


Figure 4-11: Background map (grayscale) shows the water flow paths resulting from a perturbation model with 100 model runs, and is overlain with the basal reflectivities. Black solid and dotted lines mark the newly defined shorelines for the subglacial water bodies in T2 and the previously outlined subglacial lake in T1, respectively.

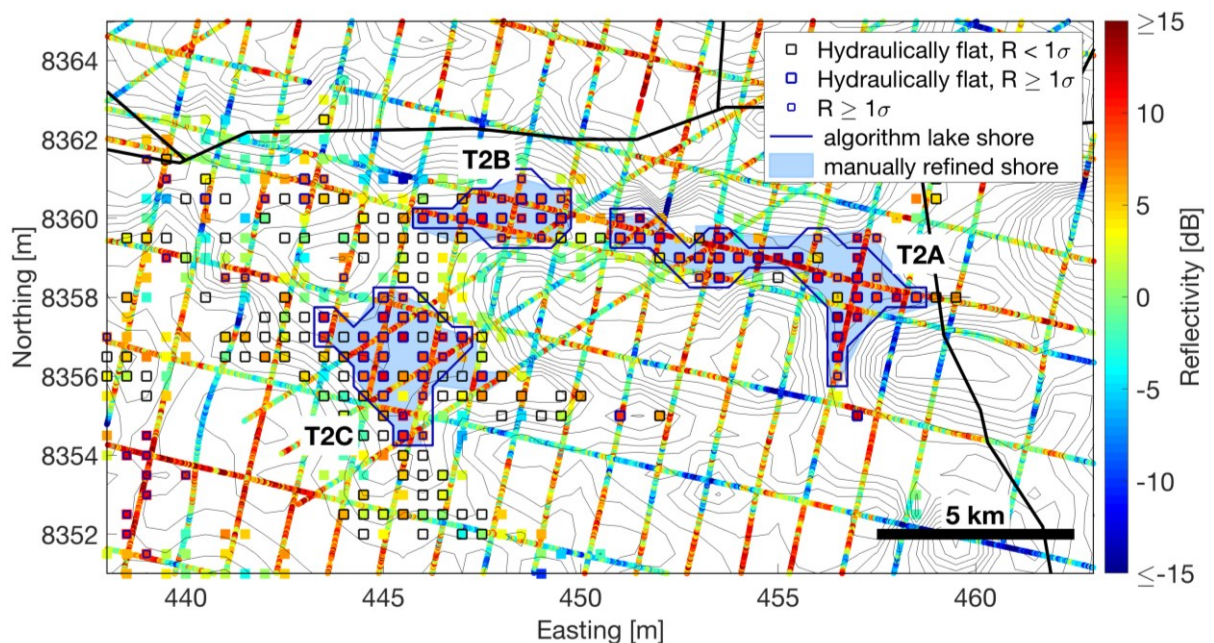


Figure 4-12: Basal reflectivities along the radar profiles and newly defined outlines of the subglacial water bodies occupying the bedrock trough T2. The squares represent grid cells of the hydraulic head mesh and are color coded with their median reflectivity value. Large squares indicate grid cells that are hydraulically flat, whereas the blue and black contours indicate whether the median grid cell reflectivity is above or below one standard deviation of all measured reflectivities (σ), respectively. Small squares represent grid cells without a flat hydraulic head but for which the median reflectivity $\geq 1\sigma$. Thin black lines represent the bedrock topography (25 m interval) whereas thick black lines mark the location of the ice divides.

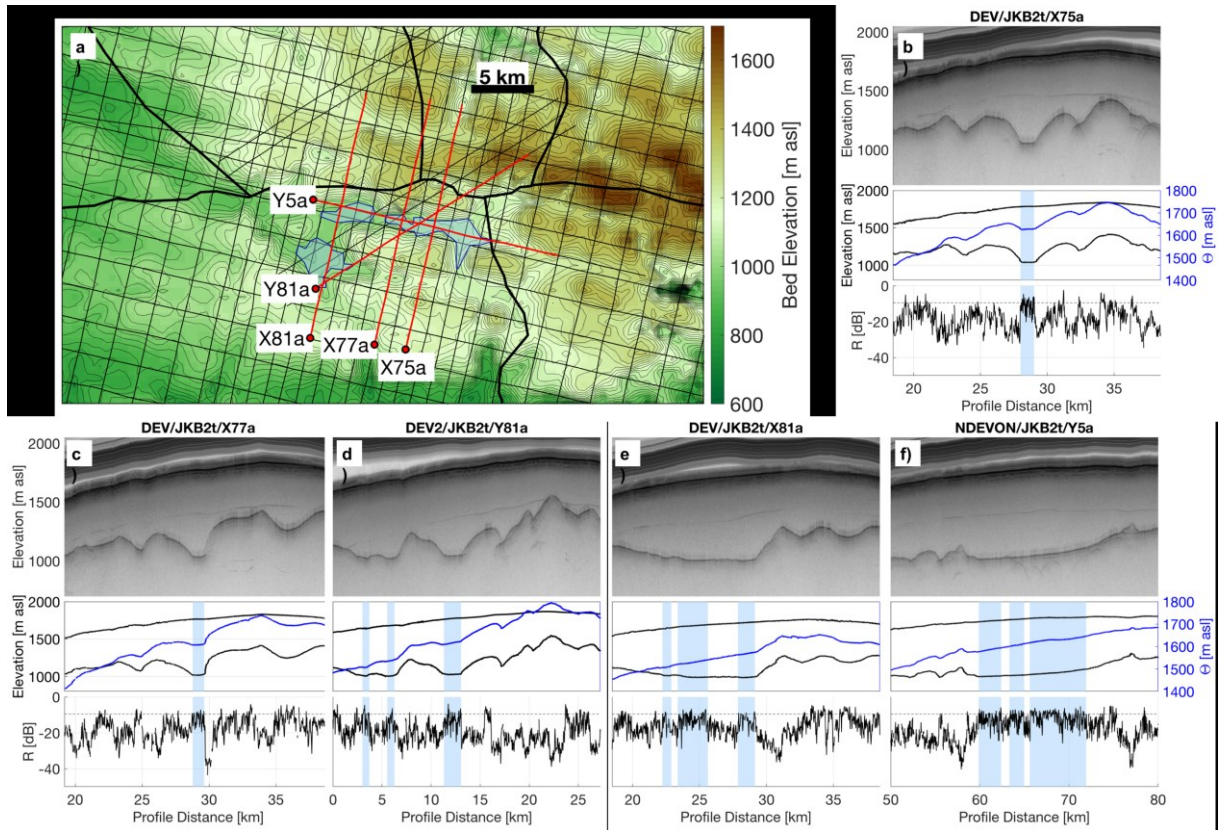


Figure 4-13: a) Bedrock topography overlain with selected radar profiles across trough T2. b-f) Selected radar sections (top panel) along with the bed and surface elevations (black) the hydraulic head Θ (blue, middle panel) and the basal reflectivity (bottom panel). Areas of the subglacial water bodies outlined from this study are shaded in blue.

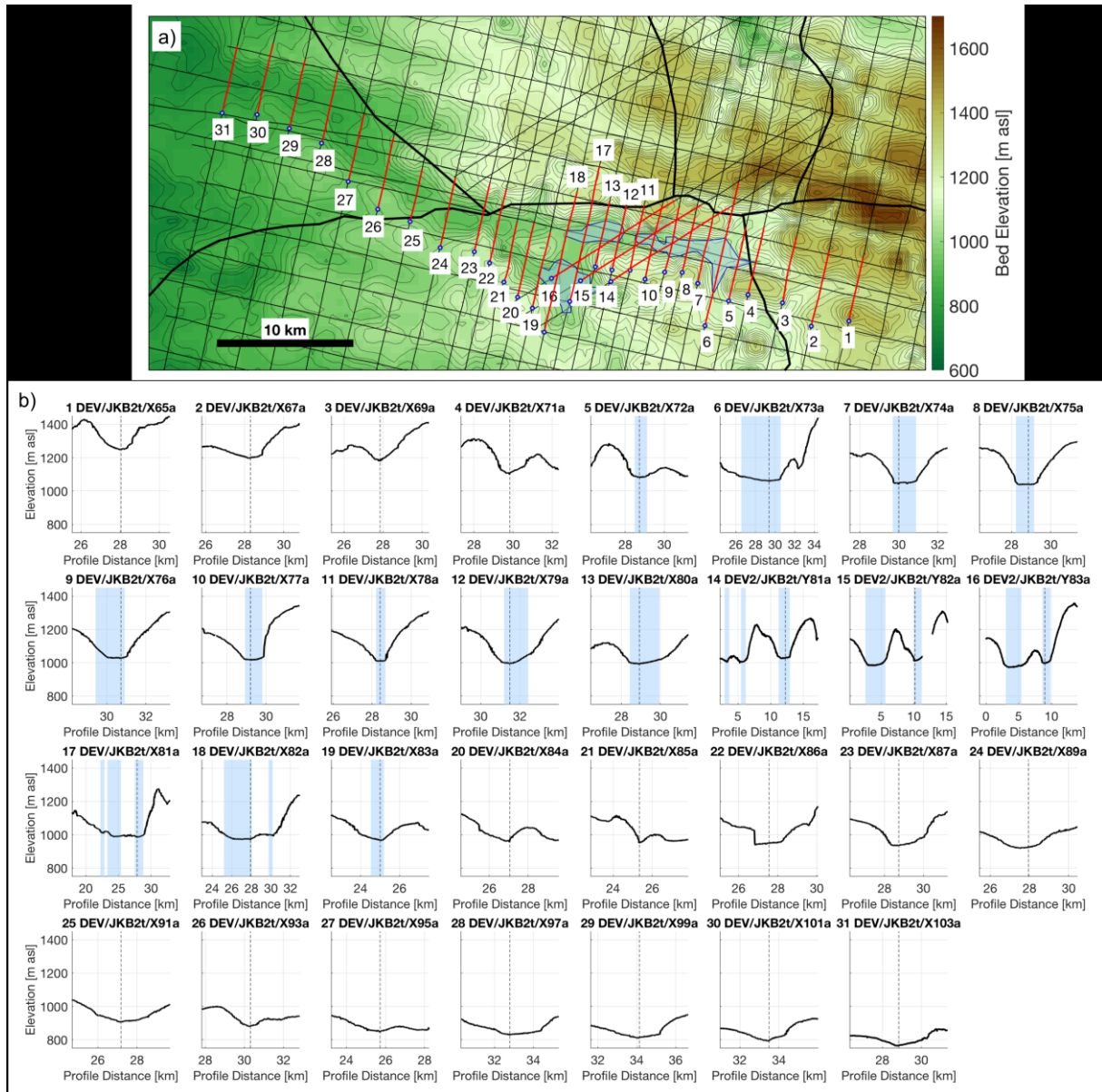


Figure 4-14: a) Bedrock topography overlain with selected profiles across the canyon extending from T2. b) Bedrock elevations along radar profiles across the canyon, revealing the trough morphology. All profiles are oriented from south towards the north, where the dot in a) marks the start point. The blue shaded areas represent the water bodies defined in this study, and the black dotted line indicates the approximate trough center defined by the water flow routes.

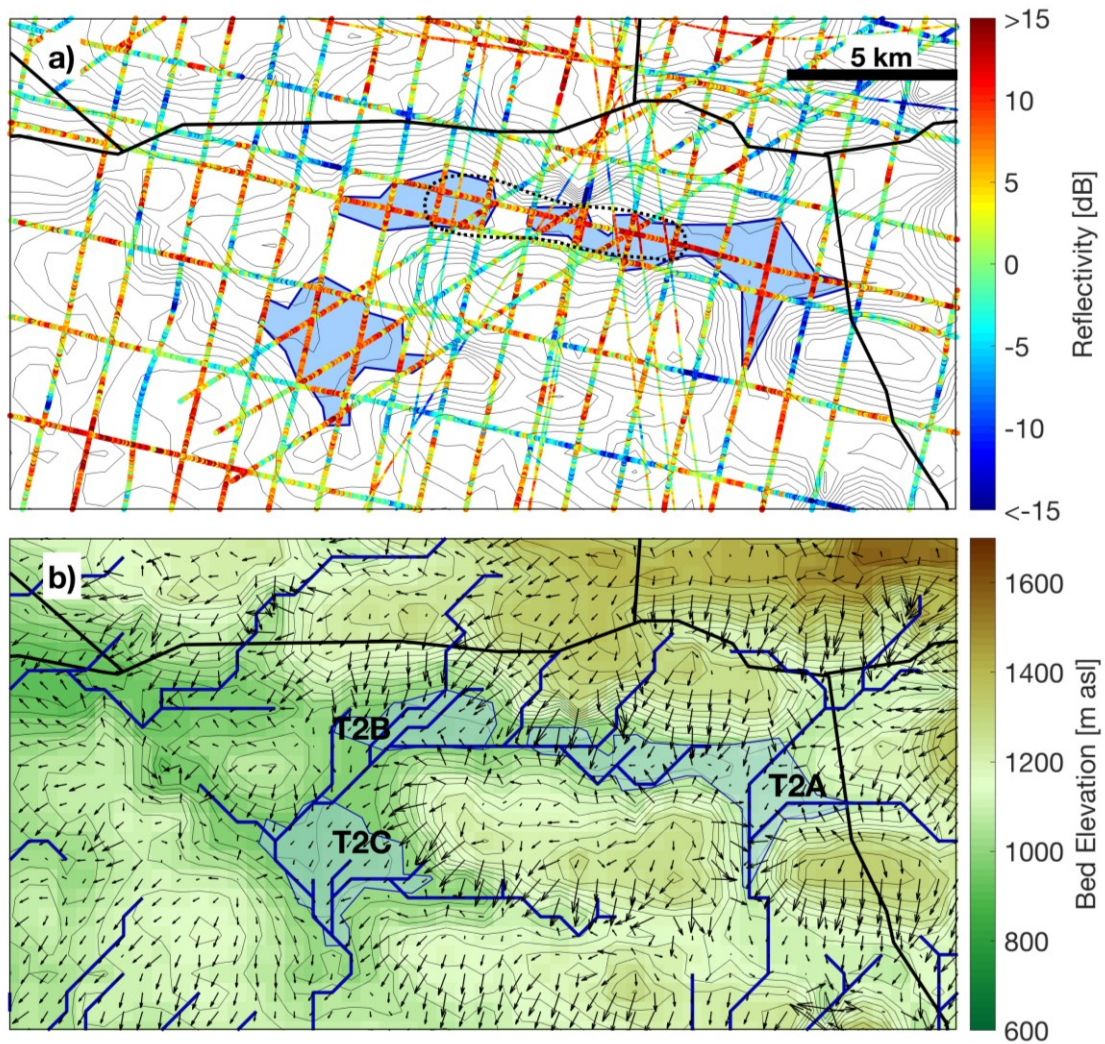


Figure 4-15: a) Bed reflectivity overlain with bed elevation contours (25 m interval) and outlines of the newly defined water bodies. Thin lines represent the MCoRDS data used for previous identification of the subglacial lake [CReSIS, 2016; Rutishauser et al., 2018]. Previously hypothesized lake outline is shown as dotted black line. b) Bed topography overlain with outlines of the newly defined water bodies and the water flow routes. Arrows follow the gradients of the hydraulic head and indicate potential water flow.

Supplementary Figures

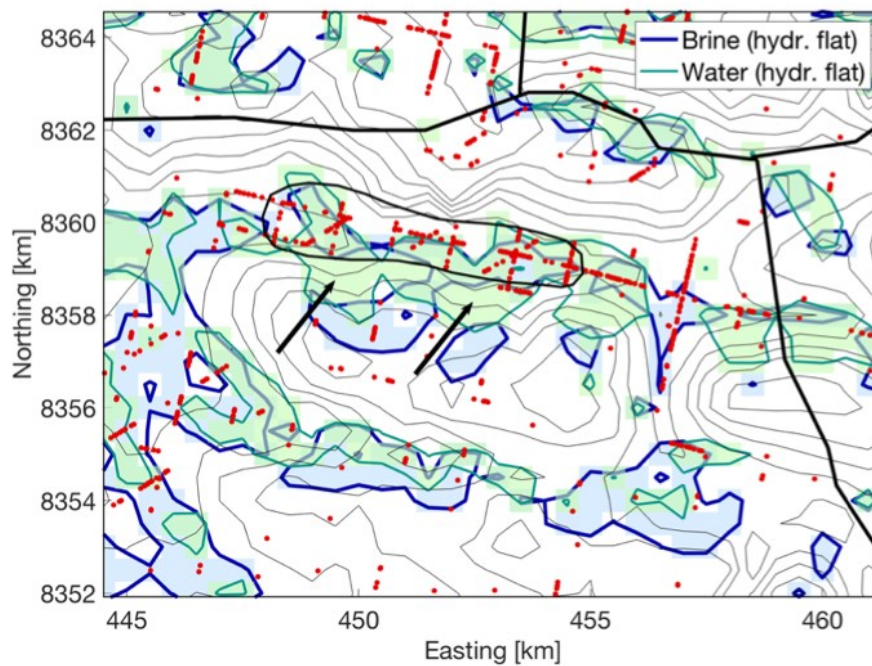


Figure S 4-1: Comparison of hydraulically flat areas computed for densities of subglacial brine (blue) and fresh water (green) over bedrock trough T2. Red dots mark areas where the basal reflectivity $R \geq 12$ dB. The hydraulic head for freshwater is flat over the southern valley slope of the subglacial bedrock trough T2, where basal reflectivities are not indicative for subglacial water. The hydraulic head for brine is also flat towards the top of the ridge south of T2. This is likely driven by the reversed bedrock and surface slopes, and not from subglacial water being in hydrostatic equilibrium.

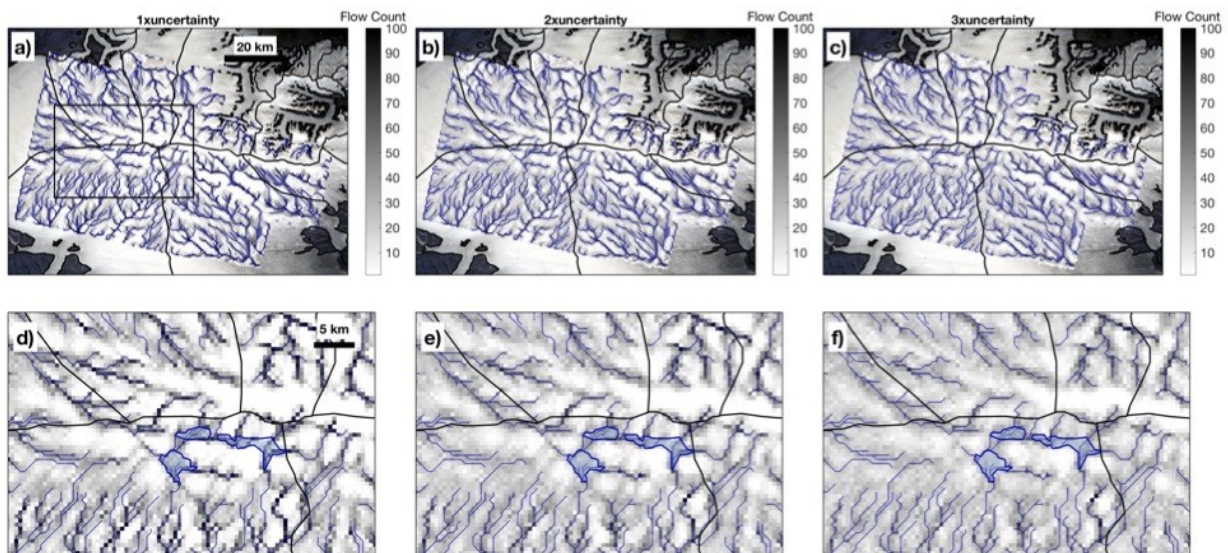


Figure S 4-2: Flow accumulation model run 100 times with randomly perturbed hydraulic heads using 1x (a, d), 2x (b, e), and 3x (c, f) its uncertainty. Blue lines represent the water flow routes without perturbation. d-f show the flow routes within the region marked in a), along with the outliers of the subglacial water bodies defined from this study.

4.9 References

- Arctic Gravity Project (2006), Arctic Gravity Project, Available from: http://www.isgeoid.polimi.it/Geoid/Artico/artico_g.html
- Badgeley, J. A., E. C. Pettit, C. G. Carr, S. Tulaczyk, J. A. Mikucki, and W. B. Lyons (2017), An englacial hydrologic system of brine within a cold glacier: Blood Falls, McMurdo Dry Valleys, Antarctica, *J. Glaciol.*, *63*, 1–14, doi:10.1017/jog.2017.16.
- Bell, R. E., M. Studinger, M. A. Fahnestock, and C. A. Shuman (2006), Tectonically controlled subglacial lakes on the flanks of the Gamburtsev Subglacial Mountains, East Antarctica, *Geophys. Res. Lett.*, *33*(2), L02504, doi:10.1029/2005GL025207.
- Boetius, A., A. M. Anesio, J. W. Deming, J. A. Mikucki, and J. Z. Rapp (2015), Microbial ecology of the cryosphere: sea ice and glacial habitats, *Nat. Rev. Microbiol.*, *13*(11), 677–690, doi:10.1038/nrmicro3522.
- Boithias, L. (1987), *Radio wave propagation*, McGraw-Hill, New York.
- Budd, W. F. (1970), Ice flow over bedrock perturbations, *J. Glacio.*, *9*(55), 29–48, doi:10.3189/S0022143000026770.
- Burgess, D., and M. J. Sharp (2004), Recent Changes in Areal Extent of the Devon Ice Cap, Nunavut, Canada, *Arctic, Antarct. Alp. Res.*, *36*(2), 261–271, doi:10.1657/1523-0430(07-069).
- Burgess, D. O., M. J. Sharp, D. W. F. Mair, J. a. Dowdeswell, and T. J. Benham (2005), Flow dynamics and iceberg calving rates of Devon Ice Cap, Nunavut, Canada, *J. Glaciol.*, *51*(173), 219–230, doi:10.3189/172756505781829430.
- Carter, S. P., D. D. Blankenship, M. E. Peters, D. A. Young, J. W. Holt, and D. L. Morse (2007), Radar-based subglacial lake classification in Antarctica, *Geochemistry, Geophys. Geosystems*, *8*(3), n/a-n/a, doi:10.1029/2006GC001408.
- Carter, S. P., D. D. Blankenship, D. a. Young, and J. W. Holt (2009), Using radar-sounding data to identify the distribution and sources of subglacial water: Application to Dome C, East Antarctica, *J. Glaciol.*, *55*(194), 1025–1040, doi:10.3189/002214309790794931.
- Christianson, K., R. W. Jacobel, H. J. Horgan, S. Anandakrishnan, and R. B. Alley (2012), Subglacial Lake Whillans - Ice-penetrating radar and GPS observations of a shallow active reservoir beneath a West Antarctic ice stream, *Earth Planet. Sci. Lett.*, *331–332*, 237–245,

doi:10.1016/j.epsl.2012.03.013.

- Christner, B. C. et al. (2014), A microbial ecosystem beneath the West Antarctic ice sheet, *Nature*, 512(7514), 310–313, doi:10.1038/nature13667.
- Chu, W., D. M. Schroeder, H. Seroussi, T. T. Creyts, S. J. Palmer, and R. E. Bell (2016), Extensive winter subglacial water storage beneath the Greenland Ice Sheet, *Geophys. Res. Lett.*, 1–9, doi:10.1002/2016GL071538.
- Chu, W., D. M. Schroeder, H. Seroussi, T. T. Creyts, and R. E. Bell (2018), Complex Basal Thermal Transition Near the Onset of Petermann Glacier, Greenland, *J. Geophys. Res. Earth Surf.*, 123(5)May, 985–995, doi:10.1029/2017JF004561.
- Cockell, C. S. et al. (2013), Subglacial Environments and the Search for Life Beyond the Earth, in *Antarctic Subglacial Aquatic Environments*, pp. 129–148, American Geophysical Union.
- Corr, H., J. C. Moore, and K. W. Nicholls (1993), Radar absorption due to impurities in Antarctic ice, *Geophys. Res. Lett.*, 20(11), 1071–1074.
- CRISIS (2016), CRISIS, *Radar Depth Sounder Data*, Lawrence, Kansas, USA, Digital Media. <http://data.cresis.ku.edu/>
- Criscitello, A. S., T. Geldsetzer, R. Rhodes, M. Arienzo, J. McConnell, M. S. Osman, J. J. Yackel, S. Marshall, and J. K. W. Chan (n.d.), Marine aerosol records of Arctic sea-ice and polynya variability from new Ellesmere and Devon Island firn cores, Nunavut, Canada, *prep.*
- Cuffey, K. M., and W. S. B. Paterson (2010), *The Physics of Glaciers*, Academic Press.
- Dowdeswell, J. A., T. J. Benham, M. R. Gorman, D. Burgess, and M. J. Sharp (2004), Form and flow of the Devon Island Ice Cap, Canadian Arctic, *J. Geophys. Res. Surf.*, 109(F2), doi:10.1029/2003JF000095.
- Evans, S. (1965), Dielectric properties of ice and snow - a review, *J. Glaciol.*, 773–792.
- Gades, A. M., C. F. Raymond, H. Conway, and R. W. Jacobel (2000), Bed properties of Siple Dome and adjacent ice streams, West Antarctica, inferred from radio-echo sounding measurements, *J. Glaciol.*, 46(152), 88–94, doi:10.3189/172756500781833467.
- Garcia-Lopez, E., and C. Cid (2017), Glaciers and ice sheets as analog environments of potentially habitable icy worlds, *Front. Microbiol.*, 8(JUL), 1407,

doi:10.3389/fmicb.2017.01407.

- Gardner, A. S., M. J. Sharp, R. M. Koerner, C. Labine, S. Boon, S. J. Marshall, D. O. Burgess, and D. Lewis (2009), Near-surface temperature lapse rates over arctic glaciers and their implications for temperature downscaling, *J. Clim.*, 22(16), 4281–4298, doi:10.1175/2009JCLI2845.1.
- Grasby, S. E. et al. (2012), Geothermal energy resource potential of Canada, *Geol. Surv. Canada, Open File, 6914*, doi:10.4095/291488.
- Harrison, J. C., T. Lynds, A. Ford, and R. H. Rainbird (2016), Geology, simplified tectonic assemblage map of the Canadian Arctic Islands, Northwest Territories - Nunavut, *Geol. Surv. Canada, Can. Geosci., Map 80*, doi:10.4095/297416.
- Howat, I. M., C. Porter, M. J. Noh, B. E. Smith, and S. Jeong (2015), Brief communication: Sudden drainage of a subglacial lake beneath the Greenland Ice Sheet, *Cryosphere*, 9(1), 103–108, doi:10.5194/tc-9-103-2015.
- Hubbard, A., W. Lawson, B. Anderson, B. Hubbard, and H. Blatter (2004), Evidence for subglacial ponding across Taylor Glacier, Dry Valleys, Antarctica, *Ann. Glaciol.*, 39(June), 79–84, doi:10.3189/172756404781813970.
- Jacobel, R. W., B. C. Welch, D. Osterhouse, R. Pettersson, and J. A. MacGregor (2009), Spatial variation of radar-derived basal conditions on Kamb Ice Stream, West Antarctica, *Ann. Glaciol.*, 50(51), 10–16, doi:10.3189/172756409789097504.
- Jacobel, R. W., K. E. Lapo, J. R. Stamp, B. W. Youngblood, B. C. Welch, and J. L. Bamber (2010), A comparison of basal reflectivity and ice velocity in East Antarctica, *Cryosph.*, 4(4), 447–452, doi:10.5194/tc-4-447-2010.
- Jamieson, S. S. R., N. Ross, J. S. Greenbaum, D. A. Young, A. R. A. Aitken, J. L. Roberts, D. D. Blankenship, S. Bo, and M. J. Siegert (2016), An extensive subglacial lake and canyon system in Princess Elizabeth Land, East Antarctica, *Geology*, 44(2), 87–90, doi:10.1130/G37220.1.
- Jordan, T. M., J. L. Bamber, C. N. Williams, J. D. Paden, M. J. Siegert, P. Huybrechts, O. Gagliardini, and F. Gillet-Chaulet (2016), An ice-sheet-wide framework for englacial attenuation from ice-penetrating radar data, *Cryosphere*, 10(4), 1547–1570, doi:10.5194/tc-10-1547-2016.

- Jordan, T. M., M. A. Cooper, D. M. Schroeder, C. N. Williams, J. D. Paden, M. J. Siegert, and J. L. Bamber (2017), Self-affine subglacial roughness: consequences for radar scattering and basal water discrimination in northern Greenland, *Cryosph.*, *11*(3), 1247–1264, doi:10.5194/tc-11-1247-2017.
- Karl, D. M., D. F. Bird, K. Björkman, T. Houlihan, R. Shackelford, and L. Tupas (1999), Microorganisms in the accreted ice of Lake Vostok, Antarctica., *Science*, *286*(5447), 2144–2147, doi:10.1126/science.286.5447.2144.
- Kinnard, C., C. M. Zdanowicz, D. a. Fisher, and C. P. Wake (2006), Calibration of an ice-core glaciochemical (sea-salt) record with sea-ice variability in the Canadian Arctic, *Ann. Glaciol.*, *44*(May 1998), 383–390, doi:10.3189/172756406781811349.
- Langley, K., J. Kohler, K. Matsuoka, A. Sinisalo, T. Scambos, T. Neumann, A. Muto, J. G. Winther, and M. Albert (2011), Recovery Lakes, East Antarctica: Radar assessment of sub-glacial water extent, *Geophys. Res. Lett.*, *38*(5), 1–5, doi:10.1029/2010GL046094.
- MacGregor, J. A., D. P. Winebrenner, H. Conway, K. Matsuoka, P. A. Mayewski, and G. D. Clow (2007), Modeling englacial radar attenuation at Siple Dome, West Antarctica, using ice chemistry and temperature data, *J. Geophys. Res. Earth Surf.*, *112*(3), 1–14, doi:10.1029/2006JF000717.
- MacGregor, J. A., K. Matsuoka, E. D. Waddington, D. P. Winebrenner, and F. Pattyn (2012), Spatial variation of englacial radar attenuation: Modeling approach and application to the Vostok flowline, *J. Geophys. Res. Earth Surf.*, *117*(3), n/a-n/a, doi:10.1029/2011JF002327.
- MacGregor, J. A., G. A. Catania, H. Conway, D. M. Schroeder, I. Joughin, D. A. Young, S. D. Kempf, and D. D. Blankenship (2013), Weak bed control of the eastern shear margin of Thwaites Glacier, West Antarctica, *J. Glaciol.*, *59*(217), 900–912, doi:10.3189/2013JoG13J050.
- MacGregor, J. A. et al. (2015), Radar attenuation and temperature within the Greenland Ice Sheet, *J. Geophys. Res. Earth Surf.*, *120*(6), 983–1008, doi:10.1002/2014JF003418.
- Matsuoka, K. (2011), Pitfalls in radar diagnosis of ice-sheet bed conditions: Lessons from englacial attenuation models, *Geophys. Res. Lett.*, *38*(5), 1–5, doi:10.1029/2010GL046205.
- Matsuoka, K., T. Furukawa, S. Fujita, H. Maeno, S. Uratsuka, R. Naruse, and O. Watanabe

- (2003), Crystal orientation fabrics within the Antarctic ice sheet revealed by a multipolarization plane and dual-frequency radar survey, *J. Geophys. Res. Solid Earth*, 108(B10), doi:10.1029/2003JB002425.
- Matsuoka, K., D. Morse, and C. F. Raymond (2010a), Estimating englacial radar attenuation using depth profiles of the returned power, central West Antarctica, *J. Geophys. Res.*, 115(F2), 1–15, doi:10.1029/2009JF001496.
- Matsuoka, K., J. A. MacGregor, and F. Pattyn (2010b), Using englacial radar attenuation to better diagnose the subglacial environment: A review, *Proc. 13th International Conf. Gr. Penetrating Radar, GPR 2010*, 1–5, doi:10.1109/ICGPR.2010.5550161.
- Matsuoka, K., J. A. MacGregor, and F. Pattyn (2012), Predicting radar attenuation within the Antarctic ice sheet, *Earth Planet. Sci. Lett.*, 359–360, 173–183, doi:10.1016/j.epsl.2012.10.018.
- Mayr, U. (1980), Stratigraphy and correlation of lower Paleozoic formations, subsurface of Bathurst Island and adjacent smaller islands, Canadian Arctic Archipelago, *Geol. Surv. Canada, Bull.*, 306.
- Mikucki, J. A., and J. C. Priscu (2007), Bacterial diversity associated with Blood Falls, a subglacial outflow from the Taylor Glacier, Antarctica, *Appl. Environ. Microbiol.*, 73(12), 4029–4039, doi:10.1128/AEM.01396-06.
- Mikucki, J. A., C. M. Foreman, B. Sattler, W. Berry Lyons, and J. C. Priscu (2004), Geomicrobiology of blood falls: An iron-rich saline discharge at the terminus of the Taylor Glacier, Antarctica, *Aquat. Geochemistry*, 10(3–4), 199–220, doi:10.1007/s10498-004-2259-x.
- Neal, C. S. (1979), The dynamics of the Ross Ice Shelf revealed by radio echo-sounding, *J. Glaciol.*, 24(90), 295–307, doi:10.1017/S0022143000014817.
- Orosei, R. et al. (2018), Radar evidence of subglacial liquid water on Mars., *Science*, 361(6401), 490–493, doi:10.1126/science.aar7268.
- Oswald, G. K. A., and S. P. Gogineni (2012), Mapping basal melt under the northern Greenland ice sheet, *IEEE Trans. Geosci. Remote Sens.*, 50(2), 585–592, doi:10.1109/TGRS.2011.2162072.
- Oswald, G. K. A., S. Rezvanbehbahani, and L. A. Stearns (2018), Radar evidence of ponded

- subglacial water in Greenland, *J. Glaciol.*, 64(247), 711–729, doi:10.1017/jog.2018.60.
- Oswald, G. K. a, and S. P. Gogineni (2008), Recovery of subglacial water extent from Greenland radar survey data, *J. Glaciol.*, 54(184), 94–106, doi:10.3189/002214308784409107.
- Palmer, S. J., J. A. Dowdeswell, P. Christoffersen, D. A. Young, D. D. Blankenship, J. S. Greenbaum, T. Benham, J. Bamber, and M. J. Siegert (2013), Greenland subglacial lakes detected by radar, *Geophys. Res. Lett.*, 40(23), 6154–6159, doi:10.1002/2013GL058383.
- Paterson, W. S. B. (1976), Vertical strain-rate measurements in an arctic ice cap and deductions from them, *J. Glaciol.*, 17(75), 3–12.
- Paterson, W. S. B., and G. K. C. Clarke (1978), Comparison of theoretical and observed temperature profiles in Devon Island ice cap, Canada, *Geophys. J. Int.*, 55(3), 615–632, doi:10.1111/j.1365-246X.1978.tb05931.x.
- Peters, M. E., D. D. Blankenship, and D. L. Morse (2005), Analysis techniques for coherent airborne radar sounding: Application to West Antarctic ice streams, *J. Geophys. Res. Solid Earth*, 110(B6), doi:10.1029/2004JB003222.
- Raymond, M. J., and G. H. Gudmundsson (2005), On the relationship between surface and basal properties on glaciers, ice sheets, and ice streams, *J. Geophys. Res.*, 110(B8), B08411, doi:10.1029/2005JB003681.
- Reeh, N., and W. S. B. Paterson (1988), Application of a flow model to the ice-divide region of Devon Island ice cap, Canada, *J. Glaciol.*, 34(116), 55–63.
- Rutishauser, A., C. Grima, M. Sharp, D. D. Blankenship, D. A. Young, F. Cawkwell, and J. A. Dowdeswell (2016), Characterizing near-surface firn using the scattered signal component of the glacier surface return from airborne radio-echo sounding, *Geophys. Res. Lett.*, 43(24), 12,502–12,510, doi:10.1002/2016GL071230.
- Rutishauser, A., D. D. Blankenship, M. Sharp, M. L. Skidmore, J. S. Greenbaum, C. Grima, D. M. Schroeder, J. A. Dowdeswell, and D. A. Young (2018), Discovery of a hypersaline subglacial lake complex beneath Devon Ice Cap, Canadian Arctic, *Sci. Adv.*, 4(4), eaar4353, doi:10.1126/sciadv.aar4353.
- Schmidt, B. E., D. D. Blankenship, G. W. Patterson, and P. M. Schenk (2011), Active formation of ‘chaos terrain’ over shallow subsurface water on Europa, *Nature*, 479(7374), 502–505,

doi:10.1038/nature10608.

- Schroeder, D. M., D. D. Blankenship, and D. A. Young (2013), Evidence for a water system transition beneath Thwaites Glacier, West Antarctica, *Proc. Natl. Acad. Sci.*, *110*(30), 12225–12228, doi:10.1073/pnas.1302828110.
- Schroeder, D. M., D. D. Blankenship, R. K. Raney, and C. Grima (2015), Estimating subglacial water geometry using radar bed echo specularity: Application to Thwaites Glacier, West Antarctica, *IEEE Geosci. Remote Sens. Lett.*, *12*(3), 443–447, doi:10.1109/LGRS.2014.2337878.
- Schroeder, D. M., H. Seroussi, W. Chu, and D. A. Young (2016a), Adaptively constraining radar attenuation and temperature across the Thwaites Glacier catchment using bed echoes, *J. Glaciol.*, *62*(236), 1075–1082, doi:10.1017/jog.2016.100.
- Schroeder, D. M., C. Grima, and D. D. Blankenship (2016b), Evidence for variable grounding-zone and shear-margin basal conditions across Thwaites Glacier, West Antarctica, *GEOPHYSICS*, *81*(1), WA35-WA43, doi:10.1190/geo2015-0122.1.
- Schwanghart, W., and N. J. Kuhn (2010), TopoToolbox: A set of Matlab functions for topographic analysis, *Environ. Model. Softw.*, *25*(6), 770–781, doi:10.1016/j.envsoft.2009.12.002.
- Shepard, M. K., B. A. Campbell, M. H. Bulmer, T. G. Farr, L. R. Gaddis, and J. J. Plaut (2001), The roughness of natural terrain: A planetary and remote sensing perspective, *J. Geophys. Res. Planets*, *106*(E12), 32777–32795, doi:10.1029/2000JE001429.
- Shreve, R. L. (1972), Movement of Water in Glaciers, *J. Glaciol.*, *11*(62), 205–214.
- Siegert, M. J., J. Taylor, and A. J. Payne (2005), Spectral roughness of subglacial topography and implications for former ice-sheet dynamics in East Antarctica, *Glob. Planet. Change*, *45*(1–3 SPEC. ISS.), 249–263, doi:10.1016/j.gloplacha.2004.09.008.
- Siegert, M. J., N. Ross, J. Li, D. M. Schroeder, D. Rippin, D. Ashmore, R. Bingham, and P. Gogineni (2016), Subglacial controls on the flow of Institute Ice Stream, West Antarctica, *Ann. Glaciol.*, *57*(73), 19–24, doi:10.1017/aog.2016.17.
- Skidmore, M., S. P. Anderson, M. Sharp, J. Foght, and B. D. Lanoil (2005), Comparison of microbial community compositions of two subglacial environments reveals a possible role for microbes in chemical weathering processes., *Appl. Environ. Microbiol.*, *71*(11), 6986–

97, doi:10.1128/AEM.71.11.6986-6997.2005.

- Willis, M. J., B. G. Herried, M. G. Bevis, and R. E. Bell (2015), Recharge of a subglacial lake by surface meltwater in northeast Greenland, *Nature*, 518(7538), 223–227, doi:10.1038/nature14116.
- Winebrenner, D. P., B. E. Smith, G. A. Catania, H. B. Conway, and C. F. Raymond (2003), Radio-frequency attenuation beneath Siple Dome, West Antarctica, from wide-angle and profiling radar observations, *Ann. Glaciol.*, 37, 226–232, doi:10.1093/nar.
- Wolovick, M. J., R. E. Bell, T. T. Creyts, and N. Frearson (2013), Identification and control of subglacial water networks under Dome A, Antarctica, *J. Geophys. Res. Earth Surf.*, 118(1), 140–154, doi:10.1029/2012JF002555.
- Wright, A., and M. J. Siegert (2013), The Identification and Physiographical Setting of Antarctic Subglacial Lakes: An Update Based on Recent Discoveries, in *Antarctic Subglacial Aquatic Environments*, pp. 9–26.
- Van Wychen, W., D. O. Burgess, L. Gray, L. Copland, M. Sharp, J. A. Dowdeswell, and T. J. Benham (2014), Glacier velocities and dynamic ice discharge from the Queen Elizabeth Islands, Nunavut, Canada, *Geophys. Res. Lett.*, 41(2), 484–490, doi:10.1002/2013GL058558.
- Van Wychen, W., J. Davis, L. Copland, D. O. Burgess, L. Gray, M. Sharp, J. A. Dowdeswell, and T. J. Benham (2017), Variability in ice motion and dynamic discharge from Devon Ice Cap, Nunavut, Canada, *J. Glaciol.*, 63(239), 436–449, doi:10.1017/jog.2017.2.
- Young, D. A., D. M. Schroeder, D. D. Blankenship, S. D. Kempf, and E. Quartini (2016), The distribution of basal water between Antarctic subglacial lakes from radar sounding, *Philos. Trans. R. Soc. A Math. Phys. Eng. Sci.*, 374(2059), 20140297, doi:10.1098/rsta.2014.0297.
- Young, D. A. et al. (2017), High resolution boundary conditions of an old ice target near Dome C, Antarctica, *Cryosph.*, (July), 1–16, doi:10.5194/tc-2016-169.

Chapter 5

Conclusions

Radio-echo sounding (RES), and in particular airborne RES is a powerful and efficient tool to derive properties of glaciers and ice caps over spatially extensive areas. Although numerous airborne RES surveys have been conducted over Devon Ice Cap (DIC), the data collected had not previously been utilized to investigate either the characteristics of the near-surface firn layer on the ice cap or the hydrological conditions beneath it. The objectives of the research presented in this thesis were to (i) investigate whether the RES signal that is returned from the glacier surface can be used to characterize the spatial heterogeneity of the near-surface firn layer on DIC, and (ii) investigate the subglacial hydrological conditions beneath this largely cold-based ice cap.

The first part of this thesis led to the development of a novel technique for characterizing the spatial heterogeneity of firn affected by melting and refreezing processes using the scattering component of the airborne RES surface return (Chapter 2). Over DIC, low scattering components are associated with laterally homogeneous firn above 1800 m asl. that contains thin, flat and continuous ice layers, and with firn below ~1200m which consists predominantly of ice. Between 1200 and 1800 m asl., high scattering components are associated with firn that contains inhomogeneous, undulating ice layers formed by re-freezing of percolated surface melt. Although this interpretation scheme was developed for DIC, the approach can easily be applied to other glaciers and ice caps and can help to identify areas where firn is affected significantly by surface melting and internal refreezing processes. Because these melting and refreezing processes can lead to large uncertainties in mass balance estimates derived from surface elevation measurements made by repeat altimetry, knowledge of the spatial extent and distribution of the firn areas affected and how they change over time is important. The results from this study (Chapter 2) regarding the origins of the scattered surface signal component and its relationship to the near-surface properties of the ice cap will potentially be very useful for exploration of planetary targets such as the icy moons of Jupiter, for which similar analyses of the radar surface returns have been proposed.

As a future study, this technique could be applied to the radar dataset collected during the spring 2018 survey over DIC (data used in Chapter 4). This would not only provide a spatially more extensive characterization of the firn, but would also allow an assessment of any changes in the firn structure that took place between the period from 2014-2018.

The second part of this thesis led to the identification and detailed characterization of a hypersaline subglacial lake complex (Chapter 3 and 4) and an extensive brine-network (Chapter 4) beneath DIC. The existence of a subglacial water system beneath the cold-based center of DIC was somewhat unexpected, and thus highlights the importance of investigating subglacial hydrological conditions through direct observations of bedrock properties. The water system beneath DIC is likely sustained as liquid at sub-freezing temperatures by a significant freezing-point depression caused by a relatively high salt concentration in the water. Geological lines of evidence suggest that a salt-bearing evaporite unit outcrops beneath the ice of DIC (Chapter 3), and this is presumed to provide the solute source for the brine. Thus, characteristics of the brine-network beneath DIC are likely related to, and potentially controlled by the bedrock lithology and topography, where the saline-rock outcrops beneath the ice play a crucial role in the formation of the hypersaline water and its geochemistry.

The hypersaline subglacial lake and brine-network beneath DIC are unprecedented worldwide. The subglacial lake is not only the first such lake to be discovered in the Canadian Arctic, but to date, is also considered to be the only spatially isolated *brine-rich* subglacial lake to be identified on Earth. This subglacial lake and the surrounding brine-network may represent unique habitats that could support microbial life and are thus compelling analogs for systems that might be suitable habitats for life on other icy planetary bodies. Due to its hypersaline nature, this subglacial lake represents a unique analog for brine bodies and pockets that may exist on Europa or Mars, and are therefore particularly compelling targets for future exploration that might include in-situ sampling and microbiological and biogeochemical investigations. The discovery of the unique subglacial lake beneath DIC (Chapter 3) is expected to be of significant scientific interest to the fields of glaciology, subglacial hydrology, and biogeochemistry as well as to those of microbiology, the limits to life in extreme environments, and the planetary sciences. This subglacial lake will likely play a major role in future research on terrestrial analogs for environments that may host life on other planetary bodies. The detailed characterization of the lake, and the evidence that is presented in this thesis for its potential connectivity to a surrounding brine-network (Chapter 4) are crucial for the planning of future research on this lake. In particular, the data and results presented here will provide the necessary context for eventual in-situ access and sampling of the lake water, any accreted ice above it, and the sediment below it.

Furthermore, other glaciers and ice caps across the Canadian Arctic may interact with evaporite units similar to the one that is the likely source of salt for the brine-rich water system beneath

DIC. Thus, this research can serve as a guide for future investigations into other equally unique subglacial water systems that may exist elsewhere in the Canadian Arctic.

Future geophysical investigations aimed at further characterization of the unique water system beneath DIC could include helicopter-borne multipolarization radar measurements, which may have the potential to identify possible transitions from a distributed to a channelized water system. Additionally, a targeted helicopter-borne radar survey may help to determine whether the subglacial lake and the individual water bodies are connected with each other and the surrounding environment by water inflow- and outflow channels. Water inflow and/or outflow likely drive circulation of the lake water, and could also play a crucial role in supporting the existence of microbial life by transporting nutrients into the lake. Additionally, future radar sounding surveys that resolve the internal layer stratigraphy within the ice column could potentially be used to identify the distribution of subglacial melting- and freeze-on processes above the lakes and the surrounding brine-network, and may help determining processes of how the subglacial brine is formed. The collection- and analysis of gravity and magnetics measurements could help to further characterize the geological context beneath DIC, and thus further constrain possible locations where the salt-bearing evaporite unit may outcrop beneath the ice. Finally, while a slope-projection of the enclosing valley walls can provide first-order estimates of the lake water depth, seismic investigations would provide more accurate water depths, and would also make it possible to characterize the substrate beneath the lake water (i.e. the character and thickness of underlying sediments). Such geophysical investigations will provide information necessary for eventual in-situ access and sampling of the lake water.

Bibliography

- Arctic Gravity Project (2006), Arctic Gravity Project, Available from: http://www.isgeoid.polimi.it/Geoid/Artico/artico_g.html
- Badgeley, J. A., E. C. Pettit, C. G. Carr, S. Tulaczyk, J. A. Mikucki, and W. B. Lyons (2017), An englacial hydrologic system of brine within a cold glacier: Blood Falls, McMurdo Dry Valleys, Antarctica, *J. Glaciol.*, *63*, 1–14, doi:10.1017/jog.2017.16.
- Bell, R. E., M. Studinger, M. A. Fahnestock, and C. A. Shuman (2006), Tectonically controlled subglacial lakes on the flanks of the Gamburtsev Subglacial Mountains, East Antarctica, *Geophys. Res. Lett.*, *33*(2), L02504, doi:10.1029/2005GL025207.
- Bezeau, P., M. Sharp, D. Burgess, and G. Gascon (2013), Firn profile changes in response to extreme 21st-century melting at Devon Ice Cap, Nunavut, Canada, *J. Glaciol.*, *59*(217), 981–991, doi:10.3189/2013JoG12J208.
- Bingham, R. G., and M. J. Siegert (2007), Radar-derived bed roughness characterization of Institute and Møller ice streams, West Antarctica, and comparison with Siple Coast ice streams, *Geophys. Res. Lett.*, *34*(21), 1–5, doi:10.1029/2007GL031483.
- Boetius, A., A. M. Anesio, J. W. Deming, J. A. Mikucki, and J. Z. Rapp (2015), Microbial ecology of the cryosphere: sea ice and glacial habitats, *Nat. Rev. Microbiol.*, *13*(11), 677–690, doi:10.1038/nrmicro3522.
- Boithias, L. (1987), *Radio wave propagation*, McGraw-Hill, New York.
- Boon, S., D. O. Burgess, R. M. Koerner, and M. J. Sharp (2010), Forty-seven Years of Research on the Devon Island Ice Cap, Arctic Canada., *Arctic*, *63*(1), 13–29.
- Braithwaite, R. J., M. Laternser, and W. T. Pfeffer (1994), Variations of near-surface firn density in the lower accumulation area of the Greenland ice sheet, Pakitsoq, West Greenland, *J. Glaciol.*, *40*(136), 477–485, doi:10.1088/0022-3727/48/32/325305.
- Budd, W. F. (1970), Ice flow over bedrock perturbations, *J. Glacio.*, *9*(55), 29–48, doi:10.3189/S0022143000026770.
- Burgess, D., and M. J. Sharp (2004), Recent Changes in Areal Extent of the Devon Ice Cap, Nunavut, Canada, *Arctic, Antarct. Alp. Res.*, *36*(2), 261–271, doi:10.1657/1523-0430(07-069).
- Burgess, D. O., M. J. Sharp, D. W. F. Mair, J. a. Dowdeswell, and T. J. Benham (2005), Flow dynamics and iceberg calving rates of Devon Ice Cap, Nunavut, Canada, *J. Glaciol.*, *51*(173), 219–230, doi:10.3189/172756505781829430.
- Carter, S. P., D. D. Blankenship, M. E. Peters, D. A. Young, J. W. Holt, and D. L. Morse (2007), Radar-based subglacial lake classification in Antarctica, *Geochemistry, Geophys. Geosystems*, *8*(3), n/a-n/a, doi:10.1029/2006GC001408.
- Carter, S. P., D. D. Blankenship, D. a. Young, and J. W. Holt (2009), Using radar-sounding data to identify the distribution and sources of subglacial water: Application to Dome C, East Antarctica, *J. Glaciol.*, *55*(194), 1025–1040, doi:10.3189/002214309790794931.
- Cassidy, N. J. (2009), Ground Penetrating Radar Data Processing, Modelling and Analysis, in *Ground Penetrating Radar Theory and Applications*, edited by H. M. Jol, pp. 141–176, Elsevier, Amsterdam.
- Christianson, K., R. W. Jacobel, H. J. Horgan, S. Anandakrishnan, and R. B. Alley (2012), Subglacial Lake Whillans - Ice-penetrating radar and GPS observations of a shallow active reservoir beneath a West Antarctic ice stream, *Earth Planet. Sci. Lett.*, *331–332*, 237–245, doi:10.1016/j.epsl.2012.03.013.
- Christner, B. C. et al. (2014), A microbial ecosystem beneath the West Antarctic ice sheet, *Nature*, *512*(7514), 310–313, doi:10.1038/nature13667.
- Chu, W., D. M. Schroeder, H. Seroussi, T. T. Creyts, S. J. Palmer, and R. E. Bell (2016), Extensive winter subglacial water storage beneath the Greenland Ice Sheet, *Geophys. Res.*

- Lett.*, 1–9, doi:10.1002/2016GL071538.
- Chu, W., D. M. Schroeder, H. Seroussi, T. T. Creyts, and R. E. Bell (2018), Complex Basal Thermal Transition Near the Onset of Petermann Glacier, Greenland, *J. Geophys. Res. Earth Surf.*, 123(5)May, 985–995, doi:10.1029/2017JF004561.
- Clifford, S. M. (1987), Polar basal melting on Mars, *J. Geophys. Res.*, 92(B9), 9135–9152, doi:10.1029/JB092iB09p09135.
- Cockell, C. S. et al. (2013), Subglacial Environments and the Search for Life Beyond the Earth, in *Antarctic Subglacial Aquatic Environments*, pp. 129–148, American Geophysical Union.
- Corr, H., J. C. Moore, and K. W. Nicholls (1993), Radar absorption due to impurities in Antarctic ice, *Geophys. Res. Lett.*, 20(11), 1071–1074.
- CReSIS (2016), CReSIS, *Radar Depth Sounder Data*, Lawrence, Kansas, USA, Digital Media. <http://data.cresis.ku.edu/>
- Criscitiello, A. S., T. Geldsetzer, R. Rhodes, M. Arienzo, J. McConnell, M. S. Osman, J. J. Yackel, S. Marshall, and J. K. W. Chan (n.d.), Marine aerosol records of Arctic sea-ice and polynya variability from new Ellesmere and Devon Island firn cores, Nunavut, Canada, *prep*.
- Cuffey, K. M., and W. S. B. Paterson (2010), *The Physics of Glaciers*, Academic Press.
- Destremes, F., and G. Cloutier (2010), A critical review and uniformized representation of statistical distributions modeling the ultrasound echo envelope, *Ultrasound Med. Biol.*, 36(7), 1037–1051, doi:10.1016/j.ultrasmedbio.2010.04.001.
- Dowdeswell, J. A., and S. Evans (2004), Investigations of the form and flow of ice sheets and glaciers using radio-echo sounding, *Reports Prog. Phys.*, 67(10), 1821–1861, doi:10.1088/0034-4885/67/10/R03.
- Dowdeswell, J. A., T. J. Benham, M. R. Gorman, D. Burgess, and M. J. Sharp (2004), Form and flow of the Devon Island Ice Cap, Canadian Arctic, *J. Geophys. Res. Surf.*, 109(F2), doi:10.1029/2003JF000095.
- Elfouhaily, T. M., and C.-A. Guérin (2004), A critical survey of approximate scattering wave theories from random rough surfaces, *Waves in Random Media*, 14(4), R1–R40, doi:10.1088/0959-7174/14/4/R01.
- Evans, S. (1965), Dielectric proper ties of ice and snow - a review, *J. Glaciol.*, 773–792.
- Fernandes, L., A. Schmitt, A. Wendleder, M. Sharp, and A. Roth (2018), Detecting Supraglacial Meltwater Drainage on the Devon Ice Cap using Kennaugh Decomposition of TerraSAR-X imagery, in *EUSAR 2018; 12th European Conference on Synthetic Aperture Radar*, pp. 1–6.
- Fisher, D., J. Zheng, D. Burgess, C. Zdanowicz, C. Kinnard, M. Sharp, and J. Bourgeois (2011), Recent melt rates of Canadian arctic ice caps are the highest in four millennia, *Glob. Planet. Change*, 84–85, 3–7, doi:10.1016/j.gloplacha.2011.06.005.
- Gades, A. M., C. F. Raymond, H. Conway, and R. W. Jacobel (2000), Bed properties of Siple Dome and adjacent ice streams, West Antarctica, inferred from radio-echo sounding measurements, *J. Glaciol.*, 46(152), 88–94, doi:10.3189/172756500781833467.
- Garcia-Lopez, E., and C. Cid (2017), Glaciers and ice sheets as analog environments of potentially habitable icy worlds, *Front. Microbiol.*, 8(JUL), 1407, doi:10.3389/fmicb.2017.01407.
- Gardner, A. S., M. J. Sharp, R. M. Koerner, C. Labine, S. Boon, S. J. Marshall, D. O. Burgess, and D. Lewis (2009), Near-surface temperature lapse rates over arctic glaciers and their implications for temperature downscaling, *J. Clim.*, 22(16), 4281–4298, doi:10.1175/2009JCLI2845.1.
- Gascon, G., M. Sharp, D. Burgess, P. Bezeau, and A. B. G. Bush (2013), Changes in accumulation-area firn stratigraphy and meltwater flow during a period of climate warming: Devon Ice Cap, Nunavut, Canada, *J. Geophys. Res. Earth Surf.*, 118(4), 2380–

- 2391, doi:10.1002/2013JF002838.
- Grasby, S. E. et al. (2012), Geothermal energy resource potential of Canada, *Geol. Surv. Canada, Open File*, 6914, doi:10.4095/291488.
- Gray, L., D. Burgess, L. Copland, M. N. Demuth, T. Dunse, K. Langley, and T. V. Schuler (2015), CryoSat-2 delivers monthly and inter-annual surface elevation change for Arctic ice caps, *Cryosphere*, 9(5), 1895–1913, doi:10.5194/tc-9-1895-2015.
- Greenbaum, J. S. et al. (2015), Ocean access to a cavity beneath Totten Glacier in East Antarctica, *Nat. Geosci.*, 8(4), 294–298, doi:10.1038/ngeo2388.
- Grima, C., W. Kofman, A. Herique, R. Orosei, and R. Seu (2012), Quantitative analysis of Mars surface radar reflectivity at 20MHz, *Icarus*, 220(1), 84–99, doi:10.1016/j.icarus.2012.04.017.
- Grima, C., D. M. Schroeder, D. D. Blankenship, and D. A. Young (2014a), Planetary landing-zone reconnaissance using ice-penetrating radar data: Concept validation in Antarctica, *Planet. Space Sci.*, 103, doi:10.1016/j.pss.2014.07.018.
- Grima, C., D. D. Blankenship, D. A. Young, and D. M. Schroeder (2014b), Surface slope control on firn density at Thwaites Glacier, West Antarctica: Results from airborne radar sounding, *Geophys. Res. Lett.*, 41(19), 6787–6794, doi:10.1002/2014GL061635.
- Gudmandsen, P. (1969), Airborne Radio Echo Sounding of the Greenland Ice Sheet, *Geogr. J.*, 135(4), 548–551, doi:10.2307/1795099.
- Hall, D. L., S. M. Sterner, and R. J. Bodnar (1988), Freezing point depression of NaCl-KCl-H₂O solutions, *Econ. Geol.*, 83, 197–202, doi:10.2113/gsecongeo.83.1.197.
- Harig, C., and F. J. Simons (2016), Ice mass loss in Greenland, the Gulf of Alaska, and the Canadian Archipelago: Seasonal cycles and decadal trends, *Geophys. Res. Lett.*, 43(7), 3150–3159, doi:10.1002/2016GL067759.
- Harrison, J. C., T. Lynds, A. Ford, and R. H. Rainbird (2016), Geology, simplified tectonic assemblage map of the Canadian Arctic Islands, Northwest Territories - Nunavut, *Geol. Surv. Canada, Can. Geosci., Map 80*, doi:10.4095/297416.
- Howat, I. M., C. Porter, M. J. Noh, B. E. Smith, and S. Jeong (2015), Brief communication: Sudden drainage of a subglacial lake beneath the Greenland Ice Sheet, *Cryosphere*, 9(1), 103–108, doi:10.5194/tc-9-103-2015.
- Hubbard, A., W. Lawson, B. Anderson, B. Hubbard, and H. Blatter (2004), Evidence for subglacial ponding across Taylor Glacier, Dry Valleys, Antarctica, *Ann. Glaciol.*, 39(June), 79–84, doi:10.3189/172756404781813970.
- Jacobel, R. W., B. C. Welch, D. Osterhouse, R. Pettersson, and J. A. MacGregor (2009), Spatial variation of radar-derived basal conditions on Kamb Ice Stream, West Antarctica, *Ann. Glaciol.*, 50(51), 10–16, doi:10.3189/172756409789097504.
- Jacobel, R. W., K. E. Lapo, J. R. Stamp, B. W. Youngblood, B. C. Welch, and J. L. Bamber (2010), A comparison of basal reflectivity and ice velocity in East Antarctica, *Cryosph.*, 4(4), 447–452, doi:10.5194/tc-4-447-2010.
- Jamieson, S. S. R., N. Ross, J. S. Greenbaum, D. A. Young, A. R. A. Aitken, J. L. Roberts, D. D. Blankenship, S. Bo, and M. J. Siegert (2016), An extensive subglacial lake and canyon system in Princess Elizabeth Land, East Antarctica, *Geology*, 44(2), 87–90, doi:10.1130/G37220.1.
- Jordan, T. M., J. L. Bamber, C. N. Williams, J. D. Paden, M. J. Siegert, P. Huybrechts, O. Gagliardini, and F. Gillet-Chaulet (2016), An ice-sheet-wide framework for englacial attenuation from ice-penetrating radar data, *Cryosphere*, 10(4), 1547–1570, doi:10.5194/tc-10-1547-2016.
- Jordan, T. M., M. A. Cooper, D. M. Schroeder, C. N. Williams, J. D. Paden, M. J. Siegert, and J. L. Bamber (2017), Self-affine subglacial roughness: consequences for radar scattering and basal water discrimination in northern Greenland, *Cryosph.*, 11(3), 1247–1264, doi:10.5194/tc-11-1247-2017.

- Karl, D. M., D. F. Bird, K. Björkman, T. Houlihan, R. Shackelford, and L. Tupas (1999), Microorganisms in the accreted ice of Lake Vostok, Antarctica., *Science*, 286(5447), 2144–2147, doi:10.1126/science.286.5447.2144.
- Kinnard, C., C. M. Zdanowicz, D. a. Fisher, and C. P. Wake (2006), Calibration of an ice-core glaciochemical (sea-salt) record with sea-ice variability in the Canadian Arctic, *Ann. Glaciol.*, 44(May 1998), 383–390, doi:10.3189/172756406781811349.
- Koerner, R. M. (1966), Accumulation on the Devon Island Ice Cap, Northwest Territories, Canada, *J. Glaciol.*, 6(45), 383–392.
- Kovacs, A., A. J. Gow, and R. M. Morey (1995), The in-situ dielectric constant of polar firm revisited, *Cold Reg. Sci. Technol.*, 23(3), 245–256, doi:10.1016/0165-232X(94)00016-Q.
- Ku, C. C., and J. A. Sharp (1983), Werner deconvolution for automated magnetic interpretation and its refinement using Marquardt's inverse modeling, *GEOPHYSICS*, 48(6), 754–774, doi:10.1190/1.1441505.
- Langley, K., J. Kohler, K. Matsuoka, A. Sinisalo, T. Scambos, T. Neumann, A. Muto, J. G. Winther, and M. Albert (2011), Recovery Lakes, East Antarctica: Radar assessment of sub-glacial water extent, *Geophys. Res. Lett.*, 38(5), 1–5, doi:10.1029/2010GL046094.
- Livingstone, S. J., C. D. Clark, J. Woodward, and J. Kingslake (2013), Potential subglacial lake locations and meltwater drainage pathways beneath the Antarctic and Greenland ice sheets, *Cryosphere*, 7(6), 1721–1740, doi:10.5194/tc-7-1721-2013.
- Lyons, W. B., K. A. Welch, G. Snyder, J. Olesik, E. Y. Graham, G. M. Marion, and R. J. Poreda (2005), Halogen geochemistry of the McMurdo dry valleys lakes, Antarctica: Clues to the origin of solutes and lake evolution, *Geochim. Cosmochim. Acta*, 69(2), 305–323, doi:10.1016/j.gca.2004.06.040.
- MacGregor, J. A., D. P. Winebrenner, H. Conway, K. Matsuoka, P. A. Mayewski, and G. D. Clow (2007), Modeling englacial radar attenuation at Siple Dome, West Antarctica, using ice chemistry and temperature data, *J. Geophys. Res. Earth Surf.*, 112(3), 1–14, doi:10.1029/2006JF000717.
- MacGregor, J. A., K. Matsuoka, E. D. Waddington, D. P. Winebrenner, and F. Pattyn (2012), Spatial variation of englacial radar attenuation: Modeling approach and application to the Vostok flowline, *J. Geophys. Res. Earth Surf.*, 117(3), n/a-n/a, doi:10.1029/2011JF002327.
- MacGregor, J. A., G. A. Catania, H. Conway, D. M. Schroeder, I. Joughin, D. A. Young, S. D. Kempf, and D. D. Blankenship (2013), Weak bed control of the eastern shear margin of Thwaites Glacier, West Antarctica, *J. Glaciol.*, 59(217), 900–912, doi:10.3189/2013JoG13J050.
- MacGregor, J. A. et al. (2015), Radar attenuation and temperature within the Greenland Ice Sheet, *J. Geophys. Res. Earth Surf.*, 120(6), 983–1008, doi:10.1002/2014JF003418.
- Mather, K. B. (1962), Further observations on sastrugi, snow dunes and the pattern of surface winds in Antarctica, *Polar Rec. (Gr. Brit.)*, 11(71), 158, doi:10.1017/S0032247400052888.
- Matsuoka, K. (2011), Pitfalls in radar diagnosis of ice-sheet bed conditions: Lessons from englacial attenuation models, *Geophys. Res. Lett.*, 38(5), 1–5, doi:10.1029/2010GL046205.
- Matsuoka, K., T. Furukawa, S. Fujita, H. Maeno, S. Uratsuka, R. Naruse, and O. Watanabe (2003), Crystal orientation fabrics within the Antarctic ice sheet revealed by a multipolarization plane and dual-frequency radar survey, *J. Geophys. Res. Solid Earth*, 108(B10), doi:10.1029/2003JB002425.
- Matsuoka, K., D. Morse, and C. F. Raymond (2010a), Estimating englacial radar attenuation using depth profiles of the returned power, central West Antarctica, *J. Geophys. Res.*, 115(F2), 1–15, doi:10.1029/2009JF001496.
- Matsuoka, K., J. A. MacGregor, and F. Pattyn (2010b), Using englacial radar attenuation to

- better diagnose the subglacial environment: A review, *Proc. 13th International Conf. Gr. Penetrating Radar, GPR 2010*, 1–5, doi:10.1109/ICGPR.2010.5550161.
- Matsuoka, K., J. A. MacGregor, and F. Pattyn (2012), Predicting radar attenuation within the Antarctic ice sheet, *Earth Planet. Sci. Lett.*, 359–360, 173–183, doi:10.1016/j.epsl.2012.10.018.
- Mayr, U. (1980), Stratigraphy and correlation of lower Paleozoic formations, subsurface of Bathurst Island and adjacent smaller islands, Canadian Arctic Archipelago, *Geol. Surv. Canada, Bull.*, 306.
- Mikucki, J. A., and J. C. Priscu (2007), Bacterial diversity associated with Blood Falls, a subglacial outflow from the Taylor Glacier, Antarctica, *Appl. Environ. Microbiol.*, 73(12), 4029–4039, doi:10.1128/AEM.01396-06.
- Mikucki, J. A., C. M. Foreman, B. Sattler, W. Berry Lyons, and J. C. Priscu (2004), Geomicrobiology of blood falls: An iron-rich saline discharge at the terminus of the Taylor Glacier, Antarctica, *Aquat. Geochemistry*, 10(3–4), 199–220, doi:10.1007/s10498-004-2259-x.
- Mikucki, J. A., E. Auken, S. Tulaczyk, R. A. Virginia, C. Schamper, K. I. Sørensen, P. T. Doran, H. Dugan, and N. Foley (2015), Deep groundwater and potential subsurface habitats beneath an Antarctic dry valley, *Nat. Commun.*, 6(May 2014), 6831, doi:10.1038/ncomms7831.
- Millan, R., J. Mouginit, and E. Rignot (2017), Mass budget of the glaciers and ice caps of the Queen Elizabeth Islands, Canada, from 1991 to 2015, *Environ. Res. Lett.*, 12(2), 024016, doi:10.1088/1748-9326/aa5b04.
- Mortimer, C. A., M. Sharp, and B. Wouters (2016), Glacier surface temperatures in the Canadian High Arctic, 2000–15, *J. Glaciol.*, (July), 1–13, doi:10.1017/jog.2016.80.
- Murray, A. E. et al. (2012), Microbial life at -13°C in the brine of an ice-sealed Antarctic lake, *Proc. Natl. Acad. Sci.*, 109(50), 2–7, doi:10.1073/pnas.1208607109/-DCSupplemental.www.pnas.org/cgi/doi/10.1073/pnas.1208607109.
- Neal, C. S. (1979), The dynamics of the Ross Ice Shelf revealed by radio echo-sounding, *J. Glaciol.*, 24(90), 295–307, doi:10.1017/S0022143000014817.
- Orosei, R. et al. (2018), Radar evidence of subglacial liquid water on Mars., *Science*, 361(6401), 490–493, doi:10.1126/science.aar7268.
- Oswald, G. K. A. (1975), Investigation of Sub-Ice Bedrock Characteristics by Radio-Echo Sounding, *J. Glaciol.*, 15(73), 75–87, doi:10.3189/S0022143000034286.
- Oswald, G. K. A., and S. P. Gogineni (2012), Mapping basal melt under the northern Greenland ice sheet, *IEEE Trans. Geosci. Remote Sens.*, 50(2), 585–592, doi:10.1109/TGRS.2011.2162072.
- Oswald, G. K. A., S. Rezvanbehbahani, and L. A. Stearns (2018), Radar evidence of ponded subglacial water in Greenland, *J. Glaciol.*, 64(247), 711–729, doi:10.1017/jog.2018.60.
- Oswald, G. K. a, and S. P. Gogineni (2008), Recovery of subglacial water extent from Greenland radar survey data, *J. Glaciol.*, 54(184), 94–106, doi:10.3189/002214308784409107.
- Palmer, S. J., J. A. Dowdeswell, P. Christoffersen, D. A. Young, D. D. Blankenship, J. S. Greenbaum, T. Benham, J. Bamber, and M. J. Siegert (2013), Greenland subglacial lakes detected by radar, *Geophys. Res. Lett.*, 40(23), 6154–6159, doi:10.1002/2013GL058383.
- Parry, V., P. Nienow, D. Mair, J. Scott, B. Hubbard, K. Steffen, and D. Wingham (2007), Investigations of meltwater refreezing and density variations in the snowpack and firn within the percolation zone of the Greenland ice sheet, *Ann. Glaciol.*, 46(1), 61–68, doi:10.3189/172756407782871332.
- Paterson, W. S. B. (1976), Vertical strain-rate measurements in an arctic ice cap and deductions from them, *J. Glaciol.*, 17(75), 3–12.
- Paterson, W. S. B., and G. K. C. Clarke (1978), Comparison of theoretical and observed

- temperature profiles in Devon Island ice cap, Canada, *Geophys. J. Int.*, 55(3), 615–632, doi:10.1111/j.1365-246X.1978.tb05931.x.
- Paterson, W. S. B., and R. M. Koerner (1974), Radio Echo Sounding on Four Ice Caps in Arctic Canada, *Arctic*, 27(3), 1–9.
- Paterson, W. S. B., R. M. Koerner, D. Fisher, S. J. Johnsen, H. B. Clausen, W. Dansgaard, P. Bucher, and H. Oeschger (1977), An oxygen-isotope climatic record from the Devon Island ice cap, arctic Canada, *Nature*, 266(5602), 508–511, doi:10.1038/266508a0.
- Peters, M. E., D. D. Blankenship, and D. L. Morse (2005), Analysis techniques for coherent airborne radar sounding: Application to West Antarctic ice streams, *J. Geophys. Res. Solid Earth*, 110(B6), doi:10.1029/2004JB003222.
- Peters, M. E., D. D. Blankenship, S. P. Carter, S. D. Kempf, D. A. Young, and J. W. Holt (2007), Along-Track Focusing of Airborne Radar Sounding Data From West Antarctica for Improving Basal Reflection Analysis and Layer Detection., *IEEE Trans. Geosci. Remote Sens.*, 45(9), 2725–2736.
- Plewes, L. A., and B. Hubbard (2001), A review of the use of radio-echo sounding in glaciology, *Prog. Phys. Geogr.*, 25(2), 203–236.
- Radić, V., and R. Hock (2011), Regionally differentiated contribution of mountain glaciers and ice caps to future sea-level rise, *Nat. Geosci.*, 4(2), 91–94, doi:10.1038/ngeo1052.
- Radić, V., A. Bliss, a. C. Beedlow, R. Hock, E. Miles, and J. G. Cogley (2013), Regional and global projections of twenty-first century glacier mass changes in response to climate scenarios from global climate models, *Clim. Dyn.*, 42(5841), 37–58, doi:10.1007/s00382-013-1719-7.
- Raymond, M. J., and G. H. Gudmundsson (2005), On the relationship between surface and basal properties on glaciers, ice sheets, and ice streams, *J. Geophys. Res.*, 110(B8), B08411, doi:10.1029/2005JB003681.
- Reeh, N., and W. S. B. Paterson (1988), Application of a flow model to the ice-divide region of Devon Island ice cap, Canada, *J. Glaciol.*, 34(116), 55–63.
- Robin, G. D. Q., D. J. Drewry, and D. T. Meldrum (1977), International Studies of Ice Sheet and Bedrock, *Philos. Trans. R. Soc. B Biol. Sci.*, 279(963), 185–196, doi:10.1098/rstb.1977.0081.
- Rutishauser, A., C. Grima, M. Sharp, D. D. Blankenship, D. A. Young, F. Cawkwell, and J. A. Dowdeswell (2016), Characterizing near-surface firn using the scattered signal component of the glacier surface return from airborne radio-echo sounding, *Geophys. Res. Lett.*, 43(24), 12,502–12,510, doi:10.1002/2016GL071230.
- Rutishauser, A., D. D. Blankenship, M. Sharp, M. L. Skidmore, J. S. Greenbaum, C. Grima, D. M. Schroeder, J. A. Dowdeswell, and D. A. Young (2018), Discovery of a hypersaline subglacial lake complex beneath Devon Ice Cap, Canadian Arctic, *Sci. Adv.*, 4(4), eaar4353, doi:10.1126/sciadv.aar4353.
- Schmidt, B. E., D. D. Blankenship, G. W. Patterson, and P. M. Schenk (2011), Active formation of ‘chaos terrain’ over shallow subsurface water on Europa, *Nature*, 479(7374), 502–505, doi:10.1038/nature10608.
- Schroeder, D. M., D. D. Blankenship, and D. A. Young (2013), Evidence for a water system transition beneath Thwaites Glacier, West Antarctica, *Proc. Natl. Acad. Sci.*, 110(30), 12225–12228, doi:10.1073/pnas.1302828110.
- Schroeder, D. M., D. D. Blankenship, R. K. Raney, and C. Grima (2015), Estimating subglacial water geometry using radar bed echo specularity: Application to Thwaites Glacier, West Antarctica, *IEEE Geosci. Remote Sens. Lett.*, 12(3), 443–447, doi:10.1109/LGRS.2014.2337878.
- Schroeder, D. M., H. Seroussi, W. Chu, and D. A. Young (2016a), Adaptively constraining radar attenuation and temperature across the Thwaites Glacier catchment using bed echoes, *J. Glaciol.*, 62(236), 1075–1082, doi:10.1017/jog.2016.100.

- Schroeder, D. M., C. Grima, and D. D. Blankenship (2016b), Evidence for variable grounding-zone and shear-margin basal conditions across Thwaites Glacier, West Antarctica, *GEOPHYSICS*, 81(1), WA35-WA43, doi:10.1190/geo2015-0122.1.
- Schwanghart, W., and N. J. Kuhn (2010), TopoToolbox: A set of Matlab functions for topographic analysis, *Environ. Model. Softw.*, 25(6), 770–781, doi:10.1016/j.envsoft.2009.12.002.
- Sharp, M., D. O. Burgess, J. G. Cogley, M. Ecclestone, C. Labine, and G. J. Wolken (2011), Extreme melt on Canada’s Arctic ice caps in the 21st century, *Geophys. Res. Lett.*, 38(11), doi:10.1029/2011GL047381.
- Shepard, M. K., B. A. Campbell, M. H. Bulmer, T. G. Farr, L. R. Gaddis, and J. J. Plaut (2001), The roughness of natural terrain: A planetary and remote sensing perspective, *J. Geophys. Res. Planets*, 106(E12), 32777–32795, doi:10.1029/2000JE001429.
- Shreve, R. L. (1972), Movement of Water in Glaciers, *J. Glaciol.*, 11(62), 205–214.
- Siegert, M. J., J. Taylor, and A. J. Payne (2005), Spectral roughness of subglacial topography and implications for former ice-sheet dynamics in East Antarctica, *Glob. Planet. Change*, 45(1–3 SPEC. ISS.), 249–263, doi:10.1016/j.gloplacha.2004.09.008.
- Siegert, M. J., N. Ross, J. Li, D. M. Schroeder, D. Rippin, D. Ashmore, R. Bingham, and P. Gogineni (2016), Subglacial controls on the flow of Institute Ice Stream, West Antarctica, *Ann. Glaciol.*, 57(73), 19–24, doi:10.1017/aog.2016.17.
- Skidmore, M., S. P. Anderson, M. Sharp, J. Foght, and B. D. Lanoil (2005), Comparison of microbial community compositions of two subglacial environments reveals a possible role for microbes in chemical weathering processes., *Appl. Environ. Microbiol.*, 71(11), 6986–97, doi:10.1128/AEM.71.11.6986-6997.2005.
- Tabatabaenejad, A., and M. Moghaddam (2010), Study of validity region of small perturbation method for two-layer rough surfaces, *IEEE Geosci. Remote Sens. Lett.*, 7(2), 319–323, doi:10.1109/LGRS.2009.2034543.
- Tabatabaenejad, A., X. Duan, and M. Moghaddam (2013), Coherent Scattering of Electromagnetic Waves From Two-Layer Rough Surfaces Within the Kirchhoff Regime, *IEEE Trans. Geosci. Remote Sens.*, 51(7), 3943–3953, doi:10.1109/TGRS.2012.2229391.
- Ulaby, F. T., R. K. Moore, and A. K. Fung (1986), *Microwave remote sensing, active and passive; Volume III, From theory to applications Remote sensing, a series of advanced level textbooks and reference works*, Artech House : Dedham, MA, United States, Univ. Mich., Ann Arbor, MI, United States.
- Vaughan, D. G., J. C. Comiso, I. Allison, J. Carrasco, G. Kaser, R. Kwok, and T. Murray (2013), IPCC Observations: Cryosphere, in *Climate Change 2013: The Physical Science Basis. Contribution of Working Group I to the Fifth Assessment Report of the Intergovernmental Panel on Climate Change*, pp. 317–382, Cambridge University Press, Cambridge, United Kingdom and New York, USA.
- Willis, M. J., B. G. Herried, M. G. Bevis, and R. E. Bell (2015), Recharge of a subglacial lake by surface meltwater in northeast Greenland, *Nature*, 518(7538), 223–227, doi:10.1038/nature14116.
- Winebrenner, D. P., B. E. Smith, G. A. Catania, H. B. Conway, and C. F. Raymond (2003), Radio-frequency attenuation beneath Siple Dome, West Antarctica, from wide-angle and profiling radar observations, *Ann. Glaciol.*, 37, 226–232, doi:10.1093/nar.
- Wolovick, M. J., R. E. Bell, T. T. Creyts, and N. Frearson (2013), Identification and control of subglacial water networks under Dome A, Antarctica, *J. Geophys. Res. Earth Surf.*, 118(1), 140–154, doi:10.1029/2012JF002555.
- Wright, A., and M. Siegert (2012), A fourth inventory of Antarctic subglacial lakes, *Antarct. Sci.*, 24(06), 659–664, doi:10.1017/S095410201200048X.
- Wright, A., and M. J. Siegert (2013), The Identification and Physiographical Setting of Antarctic Subglacial Lakes: An Update Based on Recent Discoveries, in *Antarctic*

Subglacial Aquatic Environments, pp. 9–26.

- Wyatt, F. R., and M. J. Sharp (2015), Linking surface hydrology to flow regimes and patterns of velocity variability on Devon Ice Cap, Nunavut, *J. Glaciol.*, *61*(226), 387–399, doi:10.3189/2015JoG14J109.
- Van Wychen, W., D. O. Burgess, L. Gray, L. Copland, M. Sharp, J. A. Dowdeswell, and T. J. Benham (2014), Glacier velocities and dynamic ice discharge from the Queen Elizabeth Islands, Nunavut, Canada, *Geophys. Res. Lett.*, *41*(2), 484–490, doi:10.1002/2013GL058558.
- Van Wychen, W., L. Copland, D. O. Burgess, L. Gray, and N. Schaffer (2015), Glacier velocities and dynamic discharge from the ice masses of Baffin Island and Bylot Island, Nunavut, Canada, edited by T. Fisher, *Can. J. Earth Sci.*, *52*(11), 980–989, doi:10.1139/cjes-2015-0087.
- Van Wychen, W., J. Davis, L. Copland, D. O. Burgess, L. Gray, M. Sharp, J. A. Dowdeswell, and T. J. Benham (2017), Variability in ice motion and dynamic discharge from Devon Ice Cap, Nunavut, Canada, *J. Glaciol.*, *63*(239), 436–449, doi:10.1017/jog.2017.2.
- Young, D. A., S. D. Kempf, D. D. Blankenship, J. W. Holt, and D. L. Morse (2008), New airborne laser altimetry over the Thwaites Glacier catchment, West Antarctica, *Geochemistry, Geophys. Geosystems*, *9*(6), n/a-n/a, doi:10.1029/2007GC001935.
- Young, D. A., D. M. Schroeder, D. D. Blankenship, S. D. Kempf, and E. Quartini (2016), The distribution of basal water between Antarctic subglacial lakes from radar sounding, *Philos. Trans. R. Soc. A Math. Phys. Eng. Sci.*, *374*(2059), 20140297, doi:10.1098/rsta.2014.0297.
- Young, D. A. et al. (2017), High resolution boundary conditions of an old ice target near Dome C, Antarctica, *Cryosph.*, (July), 1–16, doi:10.5194/tc-2016-169.
- Zamani, H., A. Tavakoli, and M. Dehmollaian (2016), Scattering From Layered Rough Surfaces: Analytical and Numerical Investigations, *IEEE Trans. Geosci. Remote Sens.*, *54*(6), 3685–3696, doi:10.1109/TGRS.2016.2524639.
- Zwally, H. J., W. Abdalati, T. Herring, K. Larson, J. Saba, and K. Steffen (2002), Surface Melt-Induced Acceleration of Greenland Ice-Sheet Flow, *Science (80-.)*, *297*(5579), 218–222, doi:10.1126/science.1072708.